BIOINSPIRED SOFT MATTER SELF-ASSEMBLY AND ITS USE IN BIOMEDICAL APPLICATIONS

BY

NICHOLAS EDWIN CLAY

DISSERTATION

Submitted in partial fulfillment of the requirements
for the degree of Doctor of Philosophy in Chemical Engineering
in the Graduate College of the
University of Illinois at Urbana-Champaign, 2016

Urbana, Illinois

Doctoral Committee:

Associate Professor Hyunjoon Kong, Chair
Associate Professor Mary L. Kraft
Associate Professor Charles M. Schroeder
Professor Stephen Boppart

ABSTRACT

The human body consists of a dynamic collection of polymers, colloids, and gels. Therefore, most biological matter is soft matter, and many biomedical products, such as 3D cell culture platforms or nanocarriers for drug and imaging agent delivery, often consist mostly of soft matter. Despite advances in these fields, concerns still exist regarding the function, reproducibility, and cost of soft matter systems for biomedical applications.

To mitigate these concerns, we examined a variety of methods to utilize bioinspired self-assembly to improve the function of 3D cell culture platforms and drug- and imaging agent-loaded nanocarriers. The first part of this thesis investigates the role of a hydrophilic polymer in modulating the self-assembly of collagen molecules and the subsequent mechanical properties and permeability of the collagen gel. We further examined the combined effects of gel properties and external fluid flow on cancer cell phenotypes (Chapter 2). An additional study focuses on a 3D printing technique to form multifunctional hydrogels (Chapter 3). In parallel, this thesis examined the thermodynamic effects of solvent quality and microfluidic mixer-based oil/water mixing rate on the size of nano-sized polymeric micelles and vesicles (Chapter 4). An additional study focuses on a self-assembled cluster of imaging agents for stem cell labeling (Chapter 5). Furthermore, this thesis explored a strategy to significantly increase the bioavailability of drug molecules in nanoparticles by driving self-assembly between alpha-tocopherol (Vitamin E) and amphiphilic polymers. The resulting system was functionalized to target and enhance treatment of venous neointial hyperplasia (VNH) that often occurs at arteriovenous fistula (AVF) of patients who are undergoing dialysis therapy (Chapter 6). Overall, the studies included herein will contribute broad knowledge to the fundamental science and applications of self-assembled systems for biomedical tools and products.

ACKNOWLEDGMENTS

Without the support of many people, I would not be able to complete my Ph.D. Special thanks are due to my advisor Prof. Hyunjoon Kong for his constant advice in regards to research direction and future career options. I would also like to thank my committee members as well: Prof. Stephen Boppart, Prof. Charles Schroeder, and Prof. Mary Kraft.

I would also like to thank my collaborators: the Kenis Lab (UIUC), the Bashir Lab (UIUC), the Han Lab (Purdue University), the Kim Lab (Soongsil University), the Zimmerman Lab (UIUC), the Misra Lab (Mayo Clinic) and many countless others. I would also like to thank my undergraduate researchers: Sanjeet Sen, Nicholas Cho, and Kathryn Sullivan.

I would also like to thank my friends in graduate school, including (in no particular order): Cartney Smith; Jessica Banks; Jinrong Chen; Mei-Hsiu Lai; Yu-Ching Lee; Grace Chen; Rayna Kim; Victor Shum; Kyle Trenshaw; Dan McCurry; Ashley Yeager; Robert Wilson; Jerry Montgomery, and many, many others.

I would also like to thank my family members for their encouragement (Michael A. Clay, Susan M. Clay, Natalie M. Clay, Pearl Marie Clay (deceased July 2015), Jake Sherman Clay, Linda Polanski, Gerry Polanski, Jean Clay). Most notably, my sister is a Hodgkin's lymphoma survivor, which provided me with a very personal motivation behind my work. I would also like to thank my better half Jahnabi Roy for tolerating many late nights and early mornings.

I would also like to thank the National Institutes of Health, the Dow Chemical Company, and the E. I. du Pont de Nemours and Company for their generous financial support over these last five years. This thesis is dedicated to the memory of Paul DiMarco and David Lara.

Table of Contents

CHAPTER 1: INTRODUCTION

1.1 Soft Matter in Biomedical Applications

In the past 30 years, the study of soft matter---polymer networks, colloids, gels, and foams---has emerged, forming a contrast to the "hard" matter which traditionally described the field of materials engineering. Many biological situations include some form of soft matter. For example, red blood cells can be considered deformable microparticles existing under various forms of shear.[1] Cells synthesize and remodel a dynamic network of proteins stabilized by non-covalent and covalent interactions known as the extracellular matrix.[2] DNA can be viewed as a polymer.[3] Thus, to prepare biomedical products (e.g., 3D cell cultures, nanoparticles), a knowledge of soft matter is required.

1.2 3D Cell Culture: Background and Challenges

In the past 30 years, it has been well-established that cells respond differently when grown in a three-dimensional (3D) environment than when grown in a two-dimensional petri dish.[4–6] These 3D cell culture environments often consist of a cross-linked network of water-retaining polymers, termed a hydrogel.[7] These polymers can be synthetic or natural, and can be gelled using a variety of methods, such as radical polymerization.[8] Countless studies have also demonstrated that the properties of this hydrogel, such as the mechanical stiffness or permeability of the hydrogel, strongly influence the phenotype of the cells grown in the 3D environment.[9] Given the wide range of factors which can affect cell growth, the ideal hydrogel formulation would be able to tune multiple properties independent of one another. For example, an ideal hydrogel should present a range of stiffness values while keeping permeability constant. To this end, complex, hydrogels have been prepared, with actively tunable properties in response

to external stimuli.[10–12] Simpler methods to tune hydrogel properties within an in vivo-like parameter space have yet to be explored, however. In addition, new methods to prepare simple hydrogels with dual functionalities are needed.

1.3 Therapeutic Nanoparticles: Background and Challenges

The field of nanomedicine has seen a dramatic amount of growth within the past 20 years, cumulating in the FDA approval of at least 25 nanomedicines for variety of diseases.[13] Nanomedicines offer the ability to deliver targeted drugs to diseased states in a highly selective manner, thus offering reduced systemic effects to the patient and a more effective use of each dose. Many nanomedicines are based on a polymeric nanocarrier, which can be made to degrade under certain conditions. Moreover, the size and surface properties of the nanocarrier can be tuned to enable delivery to different areas of the body. The vast amount of research in this field, however, often translates poorly into making clinical products.[14] The existing hurdles in this field include: (1) poor control over particle morphology and size; (2) low encapsulation of hydrophilic and hydrophobic drugs, as well as imaging agents; and (3) particle trafficking to undesired areas.

To solve these issues, a better understanding of the nanocarrier fabrication process is needed. In addition, new techniques and new chemistries are required to improve the encapsulation process of drug compounds with varying solubility. Moreover, methods to improve the trafficking of nanomaterials to different cells or different areas of the body are needed.

1.4 Project Overview: Bioinspired Soft Matter Self-Assembly

Nature provides a vast template for the design of self-assembled materials.[15] Almost all aspects of living creatures, from the binding of a virus onto a cell membrane to the curvature of a

bacterial cell wall, are based on self-assembly. By relying on self-assembly, I have explored new methods to address the challenges regarding 3D cell culture and nanoparticle preparation.

1.5 Self-Assembled Extracellular Matrices for Advanced 3D Cell Culture and Theranostic Designs

A significant concern in the field of hydrogel design is the incorporation of multiple functions or properties within a hydrogel. 3D cell culture in a hydrogel often requires different properties to be tuned independently of one another. For example, fluid flow in a hydrogel and hydrogel stiffness are often linked, and controlling one will change the other. In this manner, separating each hydrogel property from one another would lead to more rational 3D cell culture experiments. To this end, we played with the molecular assembly of collagen. Collagen gels are formed from the self-assembly of collagen molecules into a triple helical structure. This structure is stabilized by the presence of hydrogen bonding networks which connect the chains of the triple helix.[16] These networks can be destabilized by the presence of certain hydrophilic molecules. Therefore, we hypothesized that incorporating polyethylene glycol into a self-assembled collagen gel would soften the matrix stiffness while keeping hydraulic conductivity in the gel constant. We incorporated this gel system into a cell-microenvironment-on-a-chip (CMOC) system in order to grow cells under different pressure-driven flows and different stiffness environments. In this manner, the orthogonal effects of stiffness and flow on cancer malignancy can be observed in an in vitro platform. This project is covered in Chapter 2.

The incorporation of multiple functions is also a key design parameter when considering therapeutic or diagnostic hydrogels. Most notably, the field of theranostics requires therapeutics and diagnostics to be incorporated into the same nanoparticle or microparticle system.[17]

However, incorporating both functions---diagnostics and therapeutics—into one particle without having the diagnostic function interfere with the therapeutic function, and vice versa, remains a grand challenge in this field. To this end, we hypothesized that using a 3D printing technique would enable the incorporation of orthogonal functions within a hydrogel. This project is covered in Chapter 3.

1.6 Bioinspired Design of Micelles and Polymeric Vesicles to Contain Drugs or Imaging Agents

In the past 15 years, a significant amount of research has been devoted to prepare nano-sized vesicles with an amphiphilic polymeric bilayer or micelles with a hydrophobic core.[18] These nanostructures are often formed from the self-assembly of amphiphilic polymers under different aqueous conditions. Similar to cell membranes and organelles, these nanomaterials can package unique physiochemical functions into distinct compartments. By adding increasingly complex chemistries to these nanostructures, these bilayers and micelle structures can successfully encapsulate and release different molecules.[20]

Forming these nanoparticles with a consistent size and morphology, however, remains a challenging task. It is likely that the self-assembly of these nanomaterials depends on the processing techniques used during self-assembly, as well as the solubility of the amphiphilic polymer in different conditions. To this end, we hypothesized that adding a one-step chemical modification to an amphiphilic polymer would enable improved solubility in an organic phase. This step would enable a wider parameter space in which to explore self-assembly. Therefore, by mixing this organic phase with water in either turbulent or laminar conditions at different mixing

rates, we hypothesized that nanostructures with different sizes could be formed. This concept is explored in Chapter 4.

More importantly, fine-tuned control over the trafficking of nanomaterials from the outside to the inside of the cell is still a significant concern in the nanoparticle field. Often, it is desirable to load as many nanoparticles into a cell as possible, as in the case of imaging agent-based stem cell tracking. Here, a higher number of nanoparticles per cell considers to a higher diagnostic signal. To this end, we hypothesized that modulating the mechanical environment in which cells are grown would improve nanoparticle uptake. To test this hypothesis, we incubated stem cells with polyaspartamide-coated superparamagnetic iron oxide nanoparticles (SPIONs) clusters, and then gently stimulated the cells using an orbital shaker. The results of this study are included in Chapter 5.

Hydrophobic compounds represent a particularly unique challenge for nanoparticle delivery. Incorporating a high fraction of hydrophobic compounds into the nanoparticle interior is difficult, as most polymers used to fabricate nanoparticles are mostly hydrophilic in nature. To this end, we sought to fabricate vitamin E-loaded nanocarriers using an amphiphilic polyaspartamide polymer. We hypothesized that by tailoring the chemistry of this polymer, a nanocarrier would be formed with a size and function similar to that of chylomicrons, which are in vivo transporters of vitamin E. This topic is covered in Chapter 6.

1.7 References

(1) Doshi, N.; Zahr, A. S.; Bhaskar, S.; Lahann, J.; Mitragotri, S. Red Blood Cell-Mimicking Synthetic Biomaterial Particles. *Proc. Natl. Acad. Sci.* **2009**, *106* (51), 21495–21499.
(2) Kobayashi, T.; Kim, H.; Liu, X.; Sugiura, H.; Kohyama, T.; Fang, Q.; Wen, F.-Q.; Abe, S.; Wang, X.; Atkinson, J. J.; et al. Matrix Metalloproteinase-9 Activates TGF-β and Stimulates Fibroblast Contraction of Collagen Gels. *Am. J. Physiol. - Lung Cell. Mol. Physiol.* **2014**, *306* (11), L1006–L1015.

(3) Marciel, A. B.; Mai, D. J.; Schroeder, C. M. Template-Directed Synthesis of Structurally Defined Branched Polymers. *Macromolecules* **2015**, *48* (5), 1296–1303.
(4) Engler, A. J.; Sen, S.; Sweeney, H. L.; Discher, D. E. Matrix Elasticity Directs Stem Cell Lineage Specification. *Cell* **2006**, *126* (4), 677–689.
(5) Paszek, M. J.; Zahir, N.; Johnson, K. R.; Lakins, J. N.; Rozenberg, G. I.; Gefen, A.; Reinhart-King, C. A.; Margulies, S. S.; Dembo, M.; Boettiger, D.; et al. Tensional Homeostasis and the Malignant Phenotype. *Cancer Cell* **2005**, *8* (3), 241–254.
(6) Ekert, J. E.; Johnson, K.; Strake, B.; Pardinas, J.; Jarantow, S.; Perkinson, R.; Colter, D. C. Three-Dimensional Lung Tumor Microenvironment Modulates Therapeutic Compound Responsiveness in Vitro--Implication for Drug Development. *PloS One* **2014**, *9* (3), e92248.
(7) Barry, R. A.; Shepherd, R. F.; Hanson, J. N.; Nuzzo, R. G.; Wiltzius, P.; Lewis, J. A. Direct-Write Assembly of 3D Hydrogel Scaffolds for Guided Cell Growth. *Adv. Mater.* **2009**, *21* (23), 2407–2410.
(8) Nguyen, K. T.; West, J. L. Photopolymerizable Hydrogels for Tissue Engineering Applications. *Biomaterials* **2002**, *23* (22), 4307–4314.
(9) Cha, C.; Jeong, J. H.; Shim, J.; Kong, H. Tuning the Dependency between Stiffness and Permeability of a Cell Encapsulating Hydrogel with Hydrophilic Pendant Chains. *Acta Biomater.* **2011**, *7* (10), 3719–3728.
(10) Zhang, Y.; Yang, B.; Zhang, X.; Xu, L.; Tao, L.; Li, S.; Wei, Y. A Magnetic Self-Healing Hydrogel. *Chem. Commun.* **2012**, *48* (74), 9305–9307.
(11) Xu, F.; Wu, C. M.; Rengarajan, V.; Finley, T. D.; Keles, H. O.; Sung, Y.; Li, B.; Gurkan, U. A.; Demirci, U. Three-Dimensional Magnetic Assembly of Microscale Hydrogels. *Adv. Mater.* **2011**, *23* (37), 4254–4260.
(12) Souza, G. R.; Molina, J. R.; Raphael, R. M.; Ozawa, M. G.; Stark, D. J.; Levin, C. S.; Bronk, L. F.; Ananta, J. S.; Mandelin, J.; Georgescu, M.-M.; et al. Three-Dimensional Tissue Culture Based on Magnetic Cell Levitation. *Nat. Nanotechnol.* **2010**, *5* (4), 291–296.
(13) Ventola, C. L. The Nanomedicine Revolution. *Pharm. Ther.* **2012**, *37* (10), 582–591.
(14) Wilhelm, S.; Tavares, A. J.; Dai, Q.; Ohta, S.; Audet, J.; Dvorak, H. F.; Chan, W. C. W. Analysis of Nanoparticle Delivery to Tumours. *Nat. Rev. Mater.* **2016**, *1* (5), 16014.
(15) Philp, D.; Stoddart, J. F. Self-Assembly in Natural and Unnatural Systems. *Angew. Chem. Int. Ed. Engl.* **1996**, *35* (11), 1154–1196.
(16) Raub, C. B.; Suresh, V.; Krasieva, T.; Lyubovitsky, J.; Mih, J. D.; Putnam, A. J.; Tromberg, B. J.; George, S. C. Noninvasive Assessment of Collagen Gel Microstructure and Mechanics Using Multiphoton Microscopy. *Biophys. J.* **2007**, *92* (6), 2212–2222.
(17) Janib, S. M.; Moses, A. S.; MacKay, J. A. Imaging and Drug Delivery Using Theranostic Nanoparticles. *Adv. Drug Deliv. Rev.* **2010**, *62* (11), 1052–1063.
(18) Discher, B. M.; Won, Y.-Y.; Ege, D. S.; Lee, J. C.-M.; Bates, F. S.; Discher, D. E.; Hammer, D. A. Polymersomes: Tough Vesicles Made from Diblock Copolymers. *Science* **1999**, *284* (5417), 1143–1146.
(19) Xu, J.; Zhao, Q.; Jin, Y.; Qiu, L. High Loading of Hydrophilic/hydrophobic Doxorubicin into Polyphosphazene Polymersome for Breast Cancer Therapy. *Nanomedicine Nanotechnol. Biol. Med.* **2014**, *10* (2), 349–358.

CHAPTER 2: A CELL-MICROENVIRONMENT-ON-A-CHIP (CMOC) SYSTEM ENABLING ORTHOGONAL CONTROL OF MATRIX SOFTNESS AND INTERSTITIAL FLOW FOR 3D CELL CULTURE[1]

2.1 Introduction

Cells are subject to and regulated by a complex, three dimensional (3D) extracellular microenvironment consisting of soluble factors, matrix stiffness, and interstitial fluid.[1–4] In the past several decades, extensive efforts have been made to recapitulate the extracellular microenvironment in vitro. Doing so would provide both a better understanding of diverse cell behavior as well as an advanced screening method for newly developed medicine and biomedical

[1] I would like thank my collaborators at Purdue University for their help, including Prof. Bumsoo Han, Kyenggon Shin, and Altug Ozcelikkale. I would like to thank Kong Lab members for their help as well, including Dr. Max Rich and Dr. Min Kyung Lee. I would also like to acknowledge the School of Chemical Sciences (SCS) graphics office for their assistance with figures. Special thanks are also due to the staff at the Frederick Seitz Materials Research Laboratory for help with scanning electron microscopy (SEM). This work was partially supported by Mayo Clinic and University of Illinois Alliance for Technology-Based Healthcare, National Science Foundation (STC-EBICS Grant CBET-0939511 to H.K.), NIH HHSN261201400021C (to B.H.), CTR Award from Indiana CTSI funded in part by UL1 TR000006 from NIH (to B.H.), a grant from Walther Cancer Foundation (to B.H.), and Dow graduate fellowship (to N.C).

products.[5–8] As such, a series of in vitro cell culture platforms have been proposed to recapitulate in vivo extracellular tissue microenvironments.[9–11]

Previous studies have largely focused on reproducing the extracellular matrix properties of different tissues using various hydrogel systems formulated for 3D cell culture.[12,13] The gel properties including stiffness and cell adhesion ligand density were tailored to examine cellular response and to further regulate cellular activities. Separately, efforts have emerged to interrogate a biological role of interstitial fluid flow.[14] Interstitial fluid flow has been shown to mechanically act on cells by producing a shear force on the cell surface. Alternatively, interstitial flow can also alter the autocrine gradients in the local cell environment, leading to changes in cell migration behavior.[1] However, few efforts were made to systematically combine the effects of pressure-driven interstitial fluid flow with those of matrix properties.

In addition, increasing evidence suggests that matrix properties and interstitial flow separately influence the progressions of several acute, chronic, and malignant diseases.[15–19] Of particular note is breast cancer, which responds to both mechanical properties of the ECM and interstitial flow through different mechanisms. Several in vivo studies have demonstrated that denser breast tissue is associated with a stronger risk for breast cancer.[20]. In vitro studies have further demonstrated that breast cancer cells possess a malignant phenotype when exposed to stiffer matrices. This transition to malignancy is largely regulated by mechanosensitive pathways (such as extracellular signal-regulated kinase (ERK)) which help the breast cancer cells sense their local mechanical environment.[21,22]

Separately, several studies have demonstrated that interstitial flow in the cancer microenvironment can result in a metastatic breast cancer phenotype. It has been suggested that interstitial flow can alter the autologous chemokine gradients surrounding the cancer cell, in turn

leading to cell migration in the direction of flow.[23] Additional studies have demonstrated that interstitial flow may also act mechanically on the cancer cell surface, in turn leading to more diverse changes in cell migration behavior.[16] However, few studies were made to examine how these two factors—matrix stiffness and interstitial flow—can orchestrate malignancy in concert.

To this end, this study presents a cell microenvironment-on-a-chip (CMOC) platform that can culture cells of interest in hydrogels with controlled stiffness and interstitial flow. Cell-laden collagen gels of controlled softness were fabricated in a microfluidic chip that was assembled to create a three-dimensional perfused cell culture environment. Non-reactive polyethylene glycol (PEG) was mixed with pre-gel collagen solution to control stiffness of the collagen gel over a desired range, while minimally altering hydraulic conductivity.

During the cell culture period, cell-laden gels were continuously exposed to a pressure gradient that induced an interstitial flow of approximately 1 μm/s. In parallel, a separate set of cells were loaded into the gels with controlled stiffness but not exposed to flow. In this study, breast cancer cells were used to evaluate the function of the CMOC platform. Breast cancer malignancy was analyzed by quantifying the growth rate and expression levels of estrogen receptor-alpha (ER-α), integrin β1, and E-cadherin of tumor spheroids. ER-α is a specific breast cancer biomarker, and integrin upregulation and E-cadherin downregulation is associated with a malignant breast cancer phenotype. We anticipate the results of this study will enable the scale-down of complex tissue to a benchtop level, in turn having significant implications for fundamental cell studies and various biological applications.

2.2 Results

2.2.1 Properties of collagen-PEG and pure collagen gels

Collagen-PEG gels and pure collagen gels were prepared by changing the pH of a mixture of type I collagen and PEG from acidic to neutral.[5,24] The mass ratio of the PEG to collagen ($M_{PEG/Col}$) in the pre-gel solution was changed from 0 to 0.25 and 0.50. According to an oscillatory shear test, pure collagen gels presented a modulus of around 1 kPa. PEG added to the collagen pre-gel at $M_{PEG/Col}$ of 0.25 resulted in a softer gel, with a storage modulus of around 0.2 kPa (Figure 2.1). Further increase of $M_{PEG/Col}$ from 0.25 to 0.50 made no significant effects on the storage modulus of the resulting gel.

Interestingly, the fibrous microstructure of the gel as determined with scanning electron microscopy (SEM) was minimally changed with the addition of PEG into the collagen gel (Figure 2.2a). Regardless of the value of $M_{PEG/Col}$, the pore area of the collagen fibers quantified with SEM images was around 0.1 μm^2, and average fiber diameter was around 40 nm (Figure 2.2b and 2.2c).

The hydraulic conductivity of the gel, which represents permeability of the gel under external pressure, was also quantified by fitting a stress versus strain curve obtained with a dynamic mechanical analyzer to the nonlinear poroelastic numerical model (Figure 2.3a and 2.3b). This hydraulic conductivity value was estimated using Darcy's law by correlating the pressure difference across the channel and the average interstitial flow velocity as follows (Equation 2.1):

$$\kappa = \frac{u_{avg}}{\Delta P} \tag{2.1}$$

where κ is the hydraulic conductivity, u_{avg} is the average interstitial fluid velocity based on average perfusion rate, and ΔP is the pressure difference across the channel. The hydraulic conductivity values were approximately 2×10^{-10} m^2 Pa^{-1} s^{-1} at $M_{PEG/Col}$ of 0 and 0.25. The conductivity was increased to 6×10^{-10} m^2 Pa^{-1} s^{-1} at $M_{PEG/Col}$ of 0.50 (Figure 2.3c).

With these results, the pure collagen gel and the collagen-PEG gel with $M_{PEG/Col}$ of 0.50 were further used to assemble the CMOC platform. These two gel compositions displayed different elastic modulus (i.e., 1.0 vs 0.2 kPa) but similar mesh size. However, external force changes hydraulic conductivity of the gel, thus potentially giving rise to differential effects of interstitial flow rate.

Collagen or collagen-PEG gels were introduced into the CMOC platform via sequential filling of microchannels with pre-gel solution followed by incubation to activate gel formation in situ (Figure 2.4a) [25]. Briefly, PDMS chips with three microchannels mimicking tissue sandwiched between two blood vessels were first prepared by standard photolithography techniques. Then, a syringe-driven flow of a pure collagen solution or collagen-PEG mixture filled the center part of the microchannels in the platform. Then, incubation of the chip loaded with collagen or collagen-PEG solution at 37 ˚C for 1 h resulted in a stable gel system.

The gels formed in the CMOC platform were perfused by the cell culture medium to recapitulate interstitial flow (Figure 2.4b). In order to create the interstitial fluid flow, the gel was exposed to a pressure difference of 90 to 130 Pa across the 900 μm channel width (Figure 2.4c). Mean interstitial flow velocity was estimated by measuring the volume of culture medium perfused across the culture chamber for 24 h, as described below (Equation 2.2):

$$u_{\text{avg}} = \frac{Q_{avg}}{A_{avg}} \tag{2.2}$$

where u_{avg} is the averaged interstitial fluid velocity, Q_{avg} is the perfused media volume, and A_{gel} is the cross sectional area of the gel. Typically, with a pressure gradient of 90 to 130 Pa across the 900 μm channel width, an average interstitial flow velocity of 1 μm/s was induced, which is comparable to the flow velocity in the interstitial tissue.[16]

2.2.2 Analyzing cell phenotype in the CMOC platform

Finally, MCF-7 breast cancer cells were cultured in the gel of the CMOC platform. The mixture of cells and pre-gel solutions readily filled the center part of microchannels of the platform due to the minimal change in viscosity of the pre-gel solution. Further incubation of the chip at 37 ˚ C for 1 h generated gel matrices that stably sequestered cells. External media flow minimally affected the overall structural integrity of the cell-laden gel matrices.

According to micrographs of cells in the gels, cells loaded in both pure collagen gel and softer collagen-PEG gel underwent active proliferation and formed a 3D spheroid (Figure 2.5a). For the first four days of cell culture, no significant change in the surface area of cell spheroids was observed between the two gel conditions. In contrast, at day 6, cell spheroids formed in the softer collagen-PEG gels presented 1.5-fold larger cross-sectional area than those cultured within the stiffer pure collagen gel (Figure 2.5b). Interstitial fluid flow made a minimal difference of the cross-sectional area of spheroids, regardless of the gel stiffness.

More interestingly, the hydraulic conductivity of the cell-laden gel decreased during the cell growth. As mentioned previously, the conductivity of acellular gel was 1×10^{-10} m^2 Pa^{-1} s^{-1}, increasing to 1×10^{-11} m^2 Pa^{-1} s^{-1} after day 6.

After 6 days of growth, the cell spheroids were stained to assess cellular expression levels of estrogen receptor (ER)-α, integrin β1, and E-cadherin (Figure 2.6). It is well-known that breast cancer cells express ER-α in the cell nucleus.[26,27] In addition, integrin β1 correlates with the degree of cellular invasion into a matrix, where E-cadherin expression correlates with cell-cell adhesion and a less invasive phenotype.[28–32] The expression levels were then quantified based on the positively stained pixel intensity of the resulting fluorescent image. In the absence of interstitial fluid flow, spheroids formed in the softer collagen-PEG gels displayed two-fold higher ER-α

expression level than those in the stiffer collagen gel (Figure 2.6a). In contrast, interstitial fluid flow normalized the effect of matrix softness on ER-α expression.

In addition, gel stiffness significantly influenced cellular expression of integrin β1, while perfusion modulated expression of both integrin β1 and E-cadherin. In particular, spheroids cultured in the softer collagen-PEG gel presented almost 10-fold higher integrin expression in the absence of interstitial fluid flow. This inverse dependency of the integrin expression level on the gel stiffness was normalized by perfusing the gel, as exhibited with the decrease of the integrin expression level of spheroids in the softer collagen-PEG gels (Figure 2.6b). In contrast, E-cadherin expression level of spheroids formed in the softer collagen-PEG gel was comparable to those formed in the pure collagen gel. The perfusion of the gel increased cellular expression of E-cadherin regardless of the gel stiffness (Figure 2.6c).

2.3 Discussion

Using the CMOC platform, this study demonstrated combined effects of gel stiffness controlled with $M_{PEG/Col}$ and interstitial flow rate on malignancy of cancer cells. The role of PEG in significantly modulating gel stiffness is related to the intermolecular forces responsible for collagen gel formation. Collagen gels consist of fibers self-assembled from two or more nanometer-sized fibrils.[33,34] It has been well-agreed that the collagen fibril structure is stabilized by the orchestration of intermolecular attractive and repulsive forces.[35,36] The main attractive force involves hydrogen bonding between peptides and water molecules which bridge peptides on different collagen chains (Figure 2.7a). Previous computational and experimental studies have demonstrated that hydrogen bonds between collagen molecules and water molecules contribute to making stable collagen fibrils.[37,38] With the addition of PEG to the pre-gel collagen solution, PEG

likely associated with water molecules via hydrogen bonds, thus reducing water bridges between collagen molecules (Figure 2.7b).

Due to the decreased hydrogen bonds between collagen and water molecules, collagen molecules may associate loosely to each other, in turn inhibiting fibrillogenesis and thus forming more deformable collagen fibers. As this softening is occurring within a fibril-level, significant microscopic changes in gel mesh size are minimal.

Similarly, previous studies have reported that sugars or other hydrophilic molecules can negatively impact the self-association between collagen molecules by disrupting the hydrogen bonds between collagen and water, in turn leading to fibril disorganization.[39,40] The specific role of PEG in influencing collagen structure can be elucidated with further study. Nonetheless, this study is among the first to regulate bulk mechanical properties of a collagen gel by mediating collagen-water hydrogen bonds. This approach to forming a collagen hydrogel with tunable properties relies primarily on tuning the non-covalent interactions that form the self-assembled gel network, thus avoiding the complex chemistry required in previous approaches.[41,42]

Another interesting feature of this gel formulation is the dependency of hydraulic conductivity and gel stiffness when the gel is subject to external pressure.[43] More interestingly, the mesh size of the gel characterized with the electron microscopic image was independent of the gel stiffness.[44] This result suggests that interstitial flow rate would be higher with the softer collagen-PEG gel, likely because the external force can deform the gel structure more significantly. This interpretation is supported by decrease of the hydraulic conductivity throughout cell culture. As the cells proliferate in the gel, the gel matrix becomes more compact due to synthesis of extracellular matrix proteins.

This study further demonstrated that perfusion in the CMOC system significantly shifts breast cancer cells to a less malignant phenotype. This trend was demonstrated by a decrease in integrin β1 and an increase in E-cadherin. When considering the orthogonal mechanical cues presented to the cells, it is likely that the perfusion-driven difference of interstitial flow rate between two gel conditions, represented with hydraulic conductivity, neutralizes effects of matrix stiffness on cancer cell malignancy. These results uniquely differs from previous studies that reported the strongly interconnected relationship between cancer malignancy and matrix stiffness.[45]

This disparity from previous studies may be caused by the unique feature of the CMOC platform which allowed integrative controls of matrix stiffness and perfusion in a physiologically relevant range.[46] Besides, the biological effects of perfusion may be also mitigated by the type of matrix used for cell culture because of the different binding affinities between soluble factors and the extracellular matrix.[47] More specific phenotypic changes may be realized as the interstitial flow rate is controlled over a broader range.

With controlled hydrogel properties and interstitial fluid flow rates, increasing combinations of in vivo-like mechanical environments could be scaled down to a benchtop level. As an initial application, the microfluidic platform enabled us to demonstrate how matrix softness and interstitial fluid flow orchestrate the malignancy of breast cancer cells. In the near future, additional mechanical factors (e.g., pulsatile flow) and soluble factors (e.g., matrix metalloproteinases) can be incorporated into this system, in order to reproduce a more in vivo-like environment.[48–50]

In addition, hydrogels with transient properties (e.g., a gel that softens or stiffens in response to a certain chemical factor) could be added to prepare a “smart” CMOC system. By coupling facile hydrogel formulations and standard lithography-based PDMS chips, we envision this CMOC platform can be used for studying a wide array of chronic and malignant diseases,

ultimately leading to a full “body-on-a-chip” enabling rapid but precise drug screening as well as the development of personalized medicines.

2.4 Conclusion

In conclusion, this study demonstrated a unique CMOC platform that allows us to integrate orthogonal effects of matrix mechanics and perfusion on cells cultured in a 3D matrix. The mechanical stiffness of the cell-laden collagen gel installed in the CMOC platform was controlled by adding controlled amounts of PEG during the gelation process. The presence of PEG likely reduces hydrogen bonds between collagen and water molecules, thus resulting in softer collagen fibers. The gel formulation also enabled us to modulate hydraulic conductivity, which influences interstitial flow rate under perfusion. According to breast cancer cell culture studies with the CMOC platform, perfusion minimized the role of matrix softness in upregulating breast cancer malignancy, likely due to more significant increases in shear stress on the cell membrane and the reorganization of soluble factors in the softer gel. We envisage that the CMOC platform would be useful to better understanding and regulating the effects of multifaceted extracellular microenvironments on the genotypic and phenotypic activities of a wide array of cells.

2.5 Materials and Methods

All components were purchased from Sigma-Aldrich unless noted otherwise.

2.5.1 Preparation of collagen-PEG and pure collagen gels

To prepare a pure collagen gel ($M_{PEG/Col} = 0$), an aqueous mixture of phosphate buffered saline (PBS, Corning), NaOH, fetal bovine serum (FBS, Invitrogen) was mixed with rat tail type I

collagen (Fisher) at 4 ˚C. Then, the mixture was incubated at 37 ˚ C for at least 30 minutes. To prepare collagen-PEG gels, a desired amount of PEG (MW 7,500, Polysciences) solution was added to the pre-gelled collagen solution mixed with PBS, NaOH, and FBS. A sample receipe for a collagen gel is noted below in Table 2.1. It should be noted that the rat tail collagen solution has a different concentration from batch to batch. The volume of collagen solution added was adjusted such that the final concentration is 6 mg/mL in the gel.

2.5.2 Rheological measurement of collagen-PEG gels

Pre-gel collagen solutions with $M_{PEG/Col}$ of 0, 0.25, and 0.5 were prepared as described previously. Then, 200 µL of the pre-gel solution was quickly loaded onto the bottom plate of a parallel plate (diameter = 22 mm) configuration on a rheometer (DHR-3, TA Instruments). Once gels formed between the two parallel plates, a frequency sweep from 0.1 to 10 Hz was applied to the gels at 0.1 % strain. The storage modulus value measured at 1 Hz was reported as the storage modulus value for a given condition. At least three replicates were tested per gel.

2.5.3 Measurement of hydraulic conductivity

Hydraulic conductivity of the collagen matrices were determined using a dynamic mechanical analyzer (DMA, TA Instruments Q800) and post-analysis based on poroelastic theory. Collagen gels were prepared in a disk shape with a 12 mm diameter and a 3 mm thickness inside a polydimethylsiloxane (PDMS) mold. A sample was transferred to the DMA sample holder. Then, the gel was subject to a ramp load from 0 to 10 mN at a rate of 2 mN/min speed. The sample thickness was determined by a DMA clamp position at the beginning of the

ramp load, and this thickness was used as the reference thickness for strain computation. Stress was calculated by dividing the measured force by the sample area.

Assuming the collagen gel is approximated as a poroelastic material, its stress-strain relationship during unconfined compression can be described by an analytic solution reported by Armstrong.[51,52] By performing non-linear numerical curve-fitting of the measured stress-strain data with respect to the analytic solution, the hydraulic conductivity and shear modulus were determined. The results were obtained using an optimization routine developed in MATLAB. An R^2 coefficient of correlation greater than 0.994 was considered a good fit.

2.5.4 Scanning electron microscope (SEM) imaging of collagen-PEG and pure collagen gels

Collagen-PEG and collagen gels were prepared as described before. Approximately 100-200 uL of the pregel solution was plated on a glass slide, and then incubated at 37 ˚ C for at least 20 minutes. Then, the collagen gels were incubated in PBS for at least 30 minutes. Afterwards, the gels were fixed in 3.7 % (v/v) paraformaldehyde, and then washed with DI water four times, with each wash lasting for 15 minutes. Then, 30, 50, 70, and 100 % (v/v) ethanol solutions were each added to the gels for 30 minutes, in order to gradually dehydrate the gels. Gels were then dried using a critical point dryer, and then coated with a thin layer of gold (EMITECH 575). Scanning electron microscope images (Hitachi S4800) images were taken with at an accelerating voltage of 10 kV, and a working distance of around 9 mm.

To measure the pore area of the collagen gels, SEM images were opened in ImageJ (NIH), and an automatic threshold was applied to remove background features. Then, at least 10 areas were measured, taken across multiple images. Fiber size was measured from the raw SEM images, without taking a background correction.

2.5.5 Cell culture of MCF-7 on microfluidic devices

MCF-7 cells (ATCC) were trypsinized, mixed with pre-gel collagen solutions as previously described, and then loaded into a pre-chilled CMOC. The CMOC design was prepared as previously described.[25] The final concentration of cells was 10^7 cells/mL. Once the culture chamber was filled with collagen solution, the CMOC was incubated for 1 h at 37 ˚ C and 5 % CO_2. After gel formation, culture medium was perfused using culture medium reservoirs connected to CMOC ports. Then, the cells were incubated at 37 ˚ C and 5 % CO_2 and cultured in the CMOC for 6 days with culture medium replaced every 24 h. Interstitial flow was driven by pressure differences between the two perfusion channels. The tumor growth rate was quantified by measuring surface area of spheroids captured with brightfield images acquired with an inverted microscope (IX71, Olympus). Total cellular area was obtained using ImageJ software, then divided by the number of cell clumps in the region of interest to acquire mean cell clump area. Then, the mean cell clump area was normalized by mean cell clump area on day 0 (Equation 2.3**)**:

$$Normalized\ Mean\ Cell\ Clump\ Area = \frac{Mean\ Cell\ Clump\ Area}{\left[Mean\ Cell\ Clump\ Area\right]_{Day\ 0}}. \qquad (2.3)$$

Additionally, cells growing on top of the glass slide were rejected and only the area of 3D cell cluster within extracellular matrix was included in this analysis.

2.5.6 Immunostaining for estrogen receptor-alpha (ER-α)

To stain for ER-α, cells in the microfluidic chips were fixed in methanol-free 3.7 % paraformaldehyde for at least 24 h at room temperature. Then, cells were blocked with a PBS solution containing 10 mg/mL bovine serum albuminum (BSA), 10 % (v/v) fetal bovine serum (FBS), and 0.1 % (v/v) Tween-20 for at least 12 h. The blocking solution was perfused from both

sides of the chip, with at least 200 µL of solution used in each port. Note that for these chips, a volume of 200 µL in one port corresponds to a height of approximately 26 mm, and a volume of 100 µL in one port corresponds to a height of approximately 15 mm. Afterwards, the cells were washed at least four times with 200 µL of PBS in each port, again perfused from both sides of the chip (that is, the washing solution was perfused from each side at least twice). Then, ER-alpha antibody (HC-20, Santa Cruz Biotech) was diluted 1:200 in 10 mg/mL BSA with 0.3 % (v/v) Triton-X PBS. At least 100 µL was applied to each port at 4 ° C for at least 12 h. Again, perfusion was done from both sides of the chip, for a total staining time of at least 24 h. Then, the cells on the chip were thoroughly washed as described. Then, secondary goat anti-rabbit antibody (IgG-CFL 647, abcam) was diluted 1:200 in 10 mg/mL BSA with 0.3 % (v/v) Triton-X PBS. About 100 µL of this diluted antibody solution was applied to each port for at least 4 h at room temperature. After washing again with the previously described procedure, at least 200 µL of Hoechst stain (concentration: ~100 ng/mL) was added to each port for at least 12 h. To improve image quality, an 80 % (v/v) glycerol solution in PBS with trace amounts of ascorbic acid was added to the chip immediately before imaging.

Images were captured with a confocal microscope (Zeiss LSM 700, objective: Plan-Apochromat 40x/1.3 Oil DIC M27). To detect the signal for ER-α, laser power at 639 nm was set to 60 %, gain was set to 450, and pinhole size was set to about 1 Airy unit. These parameters were kept constant throughout. To detect the signal for the Hoechst nuclear stain, laser power at 405 nm, gain, and pinhole size were adjusted as needed. Approximately 10 images were captured at two different digital zooms (0.7 or 1.3). Contrast and brightness were evenly adjusted across all images as needed. No non-linear corrections were applied. For clarity, the 639 nm channel was converted to green on the software (Zen 2 Blue edition) before further use.

2.5.7 Image analysis of ER-α expression levels

All confocal images were analyzed in ImageJ software (NIH). First, the red, green, and blue channels were separated. Then, the channels were converted to greyscale images, and placed in a stack. The mean gray value of the green channel that co-localized with a positive signal in the blue channel (the Hoechst stain) was then quantified. In this manner, only ER-α which localized in the nuclear region was quantified. At least 20 nuclei were imaged per condition, analyzed across no fewer than three images.

2.5.8 Immunostaining for integrin β1

To stain for integrin β1, cells grown in the microfluidic chips for 6 days were fixed in methanol-free 3.7 % paraformaldehyde for at least 6 h at room temperature. Then, cells were blocked with a PBS solution containing 10 mg/mL bovine serum albuminum (BSA), 10 % (v/v) fetal bovine serum (FBS), and 0.1 % (v/v) triton-X (Fisher) for at least 9 h. The blocking solution was perfused from both sides of the chip, with at least 100 µL of solution used in each port. Afterwards, the cells were washed at least four times with 100 µL of PBS in each port, again perfused from both sides of the chip. Then, anti-β1 integrin mouse antibody (P5D2, abcam) was diluted 1:100 in 10 mg/mL BSA with 0.1 % (v/v) triton-X in PBS. At least 100 µL of the diluted antibody solution was applied to each port at 4 ° C for at least 12 h. Perfusion was done from both sides of the chip. Then, the cells on the chip were thoroughly washed as described previously. Afterwards, secondary goat polyclonal to mouse antibody with Cy5 (ab6563, abcam) was diluted 1:200 in 10 mg/mL BSA with 0.1 % (v/v) Triton-X PBS. About 100 µL of this diluted antibody solution was applied to each port for at least 4 h at room temperature. Lastly, an 80 % (v/v) glycerol solution (Fisher) in PBS with trace amounts of ascorbic acid was added to

the chip immediately before imaging. All images were captured within two weeks from the end of staining. When not imaging, samples were stored at 4 ˚ C in the dark.

Images were captured with a confocal microscope (Zeiss LSM 700, objective: Plan-Apochromat 40x/1.3 Oil DIC M27). To detect the signal for integrin β1, laser power at 639 nm was set to 55 %, detector gain was set to 575, and pinhole size was set to about 1 Airy unit. These parameters were kept constant throughout. Contrast and brightness were evenly adjusted across all images as needed. No non-linear corrections were applied. The 639 nm channel was converted to red or orange in the Zen Blue software before further use.

2.5.9 Immunostaining for E-cadherin

To stain for E-cadherin, cells grown in the microfluidic chips for 6 days were fixed in methanol-free 3.7 % paraformaldehyde for at least 6 h at room temperature. Then, cells were blocked with a PBS solution containing 10 mg/mL bovine serum albuminum (BSA), 10 % (v/v) fetal bovine serum (FBS), and 0.1 % (v/v) triton-X for at least 9 h. The blocking solution was perfused from both sides of the chip, with at least 100 µL of solution used in each port. Afterwards, the cells were washed at room temperature at least four times with 100 µL of PBS in each port, again perfused from both sides of the chip. Then, anti-E-cadherin primary rabbit antibody (24E10, Cell Signaling Technology) was diluted 1:100 in 10 mg/mL BSA with 0.1 % (v/v) Triton-X in PBS. At least 100 µL of the diluted antibody solution was applied to each port at 4 ° C for at least 12 h. Perfusion was done from both sides of the chip. Then, the cells on the chip were thoroughly washed as described previously. Afterwards, secondary anti-rabbit antibody with an Alexa Fluor conjugate (Cell Signaling Technology) was diluted 1:100 in 10 mg/mL BSA with 0.1 % (v/v) Triton-X in PBS. About 100 µL of this diluted antibody solution

was applied to each port for at least 4 h at room temperature. After thorough washing, an 80 % glycerol solution in PBS with trace amounts of ascorbic acid was added to the chip immediately before imaging.

Images were captured with a confocal microscope (Zeiss LSM 700, objective: Plan-Apochromat 40x/1.3 Oil DIC M27). To detect the signal for E-cadherin, laser power at 555 nm was set to 18 %, detector gain was set to 575, and pinhole size was set to about 1 Airy unit. These parameters were kept constant throughout. At least 10 images were captured, each with a different digital zoom (0.7 and 1.3). Contrast and brightness were evenly adjusted across all images as needed. No non-linear corrections (e.g., gamma corrections) were applied. For clarity, the 555 nm channel was converted to green in the Zen Blue software before further use.

2.5.10 Image analysis for integrin β1and E-cadherin

To quantify the expression level for integrin β1and E-cadherin, the images were split into individual channels in ImageJ (red, green, and blue). Here, each channel is converted into a separate grey and white image. Then, the mean gray value was calculated for a given region of interest. The mean gray value reports the pixel intensity averaged over a region of interest; a higher mean gray value corresponds to a higher level of expression. For integrin β1, a cell spheroid as well as its extracellular components was considered as a region of interest. For E-cadherin, only the cell spheroid was considered as the region of interest. At least ten spheroids were measured per condition, taken from no fewer than 5 images. For accurate reporting of the expression level, the background mean gray value was measured and subtracted from the mean gray value for a region of interest.

2.5.11 Statistical analysis of data

To quantify statistical significance between two or more conditions, a one-way ANOVA test with a post-hoc Tukey's test (R Studio 3.2.2) was used. p values lower than 0.05 were considered statistically significant.

2.6 Figures and Tables

	Amount (µL)		
Collagen-PEG Mass Ratio	**0**	**0.25**	**0.5**
10X PBS	100.00	100.00	100.00
Sterile 1.0 N NaOH	16.47	16.47	16.47
0.1 M Hepes	30.00	30.00	30.00
P/S	1.00	1.00	1.00
L- Glutamine	10.00	10.00	10.00
FBS	60.00	60.00	60.00
PEG solution (300 mg/mL, MW 7,500 g/mol)	0.00	5.00	10.00
Sterile dH2O	66.54	61.54	56.54
Rat Tail Collagen	715.99	715.99	715.99

Table 2.1 Example recipe for forming collagen-PEG gels.

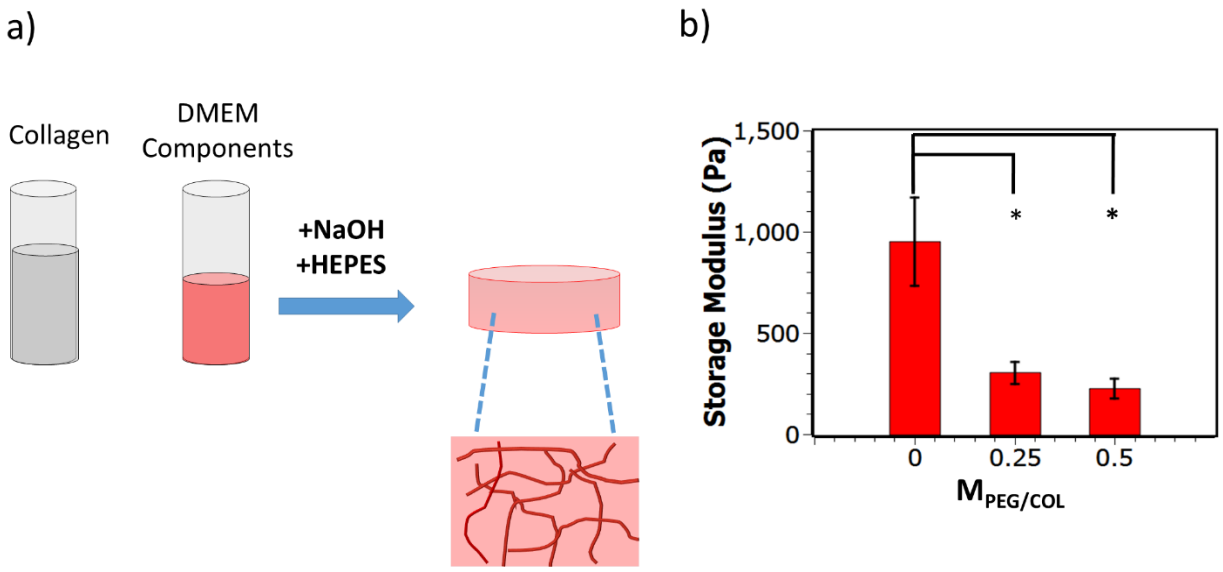

Figure 2.1 Stiffness of collagen gels mixed with controlled amounts of polyethylene glycol (PEG) ($M_{PEG/Col}$)**.** (a) Schematic depicting the formation of a collagen hydrogel. A dissolved acidic collagen solution is mixed with DMEM components (fetal bovine serum, glutamine, and penicillin-streptomycin). NaOH and HEPES are then added to increase the pH of the solution, in turn making a gel at 37 ˚ C. The pH change was the same for all gel formulations. (b) Storage modulus values for the pure collagen gel with no PEG ($M_{PEG/Col} = 0$), the collagen gel with $M_{PEG/Col}$ of 0.25, and the collagen gel with a mass ratio of PEG to collagen of 0.5 with $M_{PEG/Col}$ of 0.5. Storage modulus was measured at a frequency of 1 Hz. * represents the statistically significant difference of values between conditions ($p < 0.05$). Values and error bars on the graphs represent mean and standard deviation of at least three samples per condition, respectively.

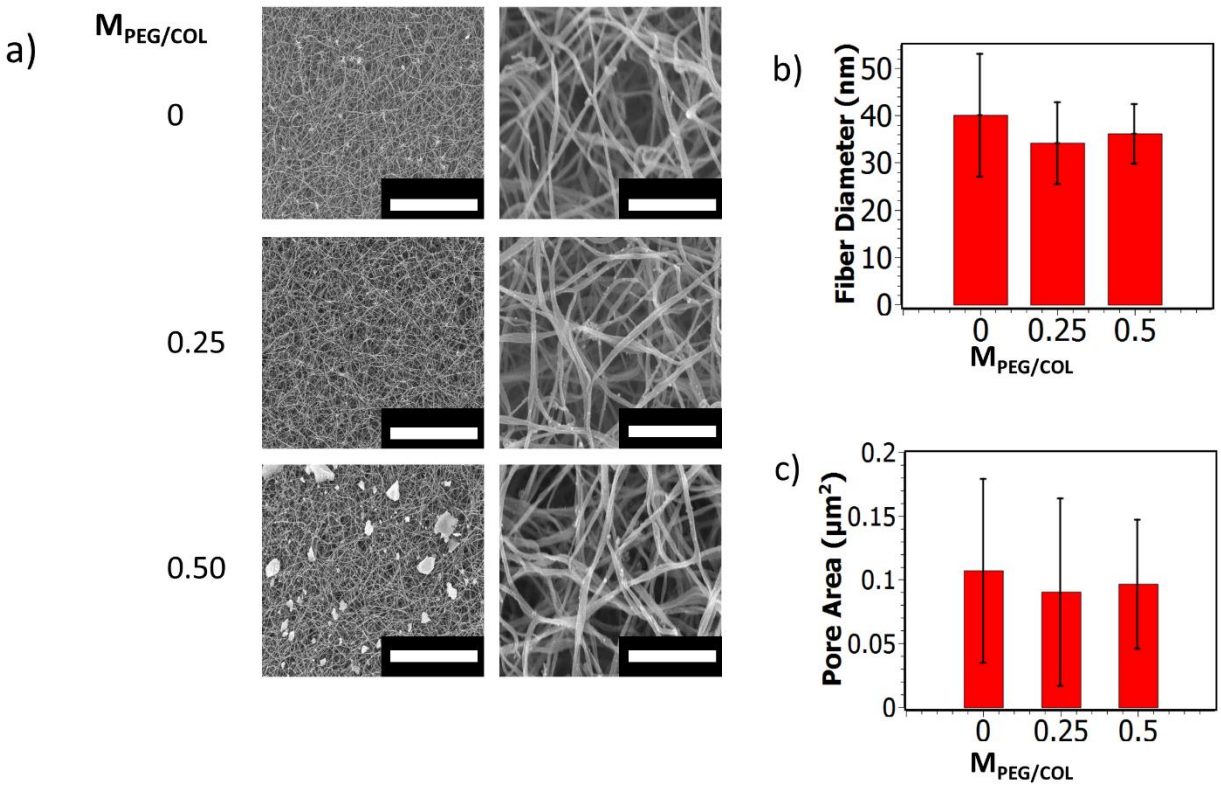

Figure 2.2 Microstructure of collagen gels mixed with controlled amounts of polyethylene glycol (PEG). (a) Scanning electron microscopy (SEM) images of collagen gels with controlled $M_{PEG/Col}$. Scale bars correspond to 10 μm (low magnification, left column) or 1 μm (high magnification, right column). (b) Fiber diameter of the resulting collagen fibers, as determined from SEM images of the gels. (c) Pore area of the fibrous collagen network as determined from SEM images of the gels. No statistical significance is denoted between the different conditions in (b) or (c).

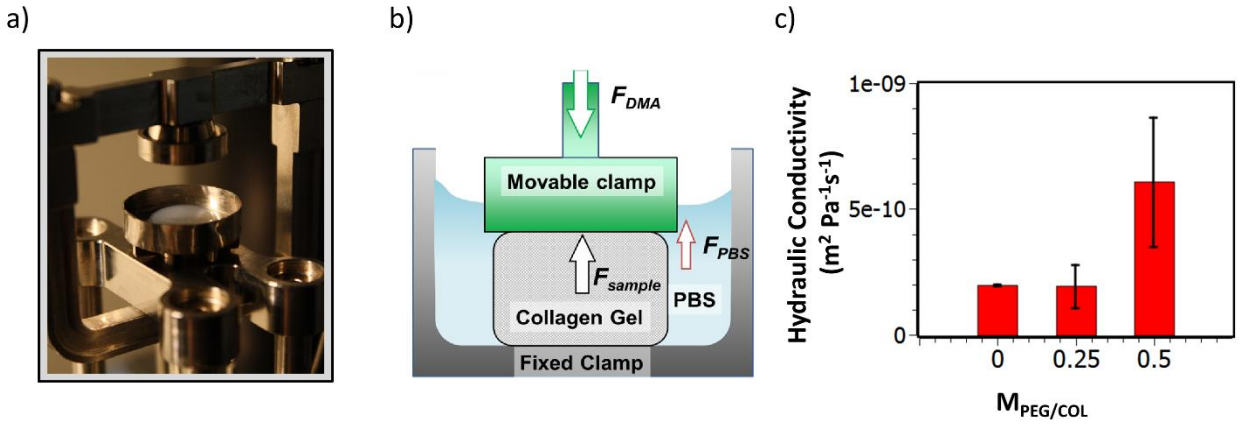

Figure 2.3 Hydraulic conductivity analysis for collagen gels made with controlled amounts of polyethylene glycol (PEG) to collagen mass ratio ($M_{PEG/Col}$)**.** (a) Image of the dynamic mechanical analyzer (DMA) setup loaded with a collagen gel. (b) Schematic describing the process of loading and testing the collagen gel in the DMA. The collagen gel was immersed in phosphate buffer saline (PBS). Compressive force by the DMA (F_{DMA}) is balanced by the reaction force by the collagen gel (F_{sample}) and the surface tension of phosphate buffered saline (F_{PBS}). (c) Hydraulic conductivity data for the pure collagen gel with no PEG ($M_{PEG/Col}$ = 0), the collagen gel with $M_{PEG/Col}$ of 0.25, and the collagen gel with $M_{PEG/Col}$ of 0.5. Values represent the mean of at least three samples per condition. Error bars represent standard deviation. No statistical significance is denoted between the different conditions in (c).

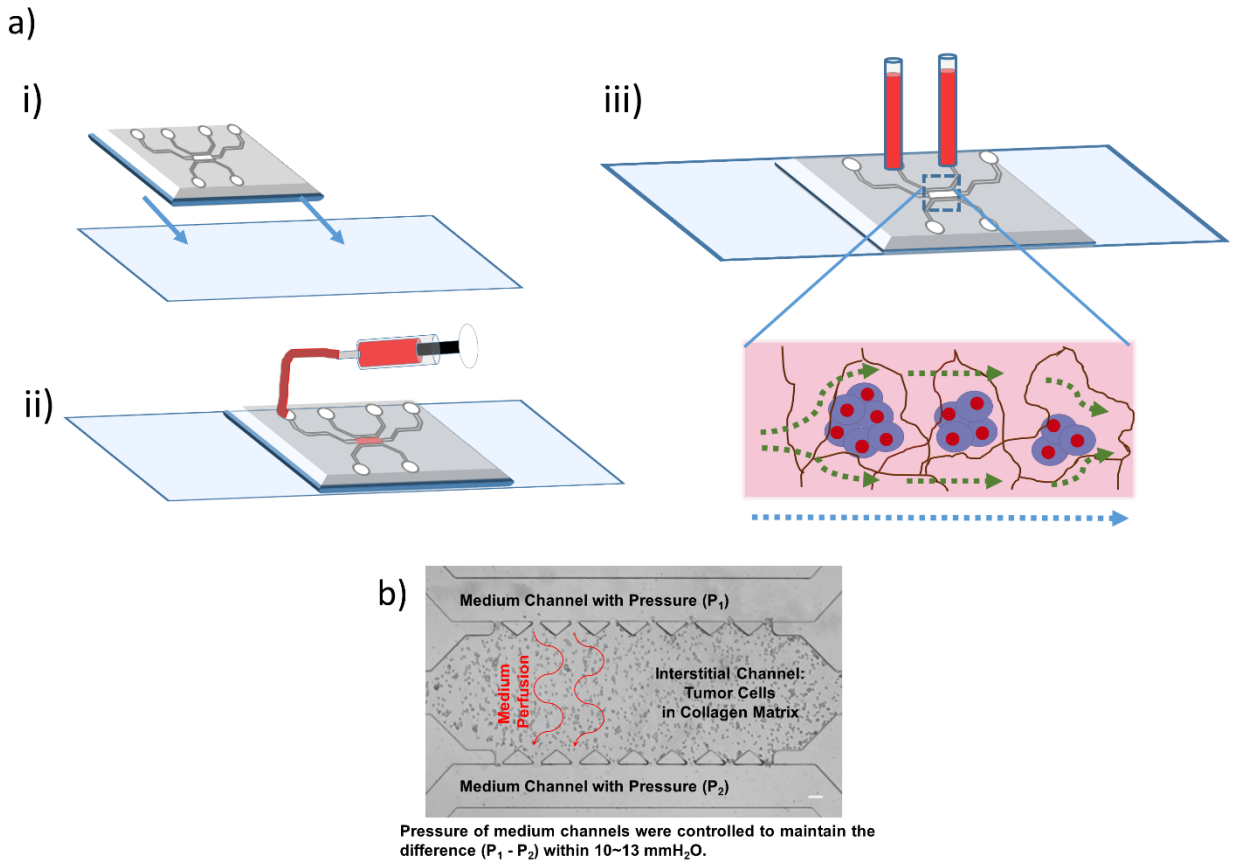

Figure 2.4 Preparation of Cell-Microenvironment-on-a-Chip (CMOC) system. (a) Schematic describing preparation of a cell-microenvironment-on-a-chip (CMOC) system. (i) A PDMS chip is prepared via standard lithography, and then bonded to a glass slide. (ii) A pregel collagen solution containing cells is loaded into a syringe, then pumped through the CMOC system. (iii) After collagen gel formation, a pressure gradient is applied across the CMOC, in turn inducing an interstitial flow. (b) Brightfield microscope image of CMOC loaded with a collagen ($M_{PEG/Col}$= 0) or collagen-PEG gel ($M_{PEG/Col}$= 0.5). The red arrow depicts the approximate path of perfusion through the gel system. White scale bar corresponds to 100 µm.

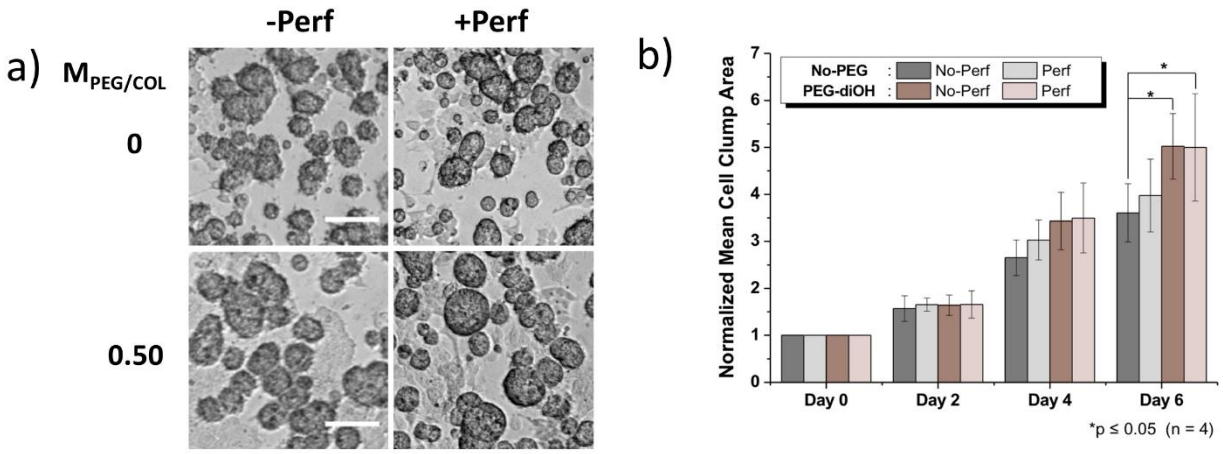

Figure 2.5 Cell proliferation analysis (a) Brightfield image of breast cancer cells grown in the CMOC system after six days. Cells were cultured in the gels for 6 days, both without perfusion (-Perf) and with perfusion (+Perf). White scale bar corresponds to 100 µm. (b) The normalized cross-sectional area of spheroids as quantified with brightfield images over 6 days of cell culture. At least 4 areas were quantified for each time point. * represents the statistically significant difference of values between conditions ($p < 0.05$). Values and error bars on the graphs represent mean and standard deviation of at least three samples per condition, respectively

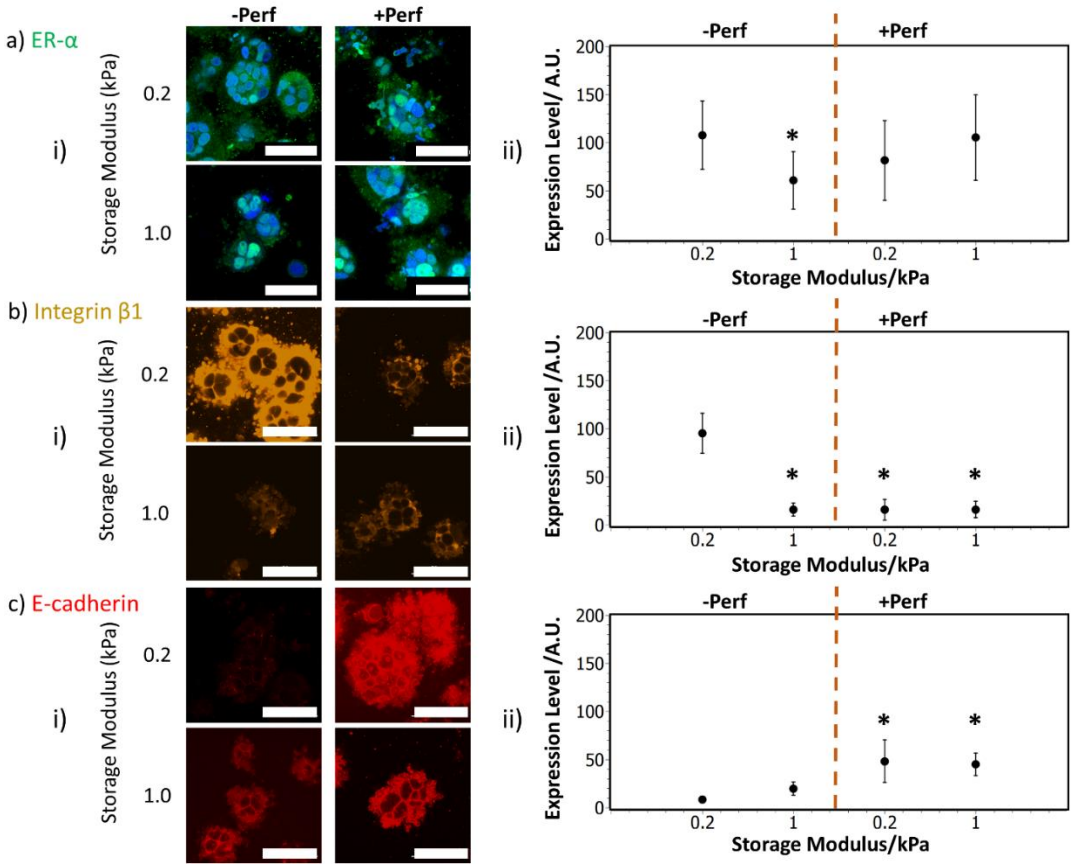

Figure 2.6 Immunostained image analysis of MCF-7 breast cancer cells cultured in the CMOC system. (a-i) Confocal microscope images of cells stained for ER-α. The green stain corresponds to ER-α, and the blue stain corresponds to the Hoechst nuclear stain. (a-ii) Expression levels of ER-αas quantified with ImageJ. (b-i) Confocal microscope images of MCF-7 breast cancer cells stained for integrin β1 (orange). (b-ii) Expression levels of integrin β1 as quantified with ImageJ. (c-i) Confocal microscope images of cells stained for E-cadherin (red). (c-ii) Expression levels of E-cadherin quantified with ImageJ. All scale bars correspond to 50 µm. Cells were grown without perfusion (-Perf) and with perfusion (+Perf) in the gels with storage modulus of 0.2 and 1.0 kPa. Values and error bars on the graphs represent mean and standard deviation of at least five images per condition. * denotes a condition that is statistically significant ($p < 0.05$) when compared to the value at 0.2 kPa in the absence of perfusion (-Perf).

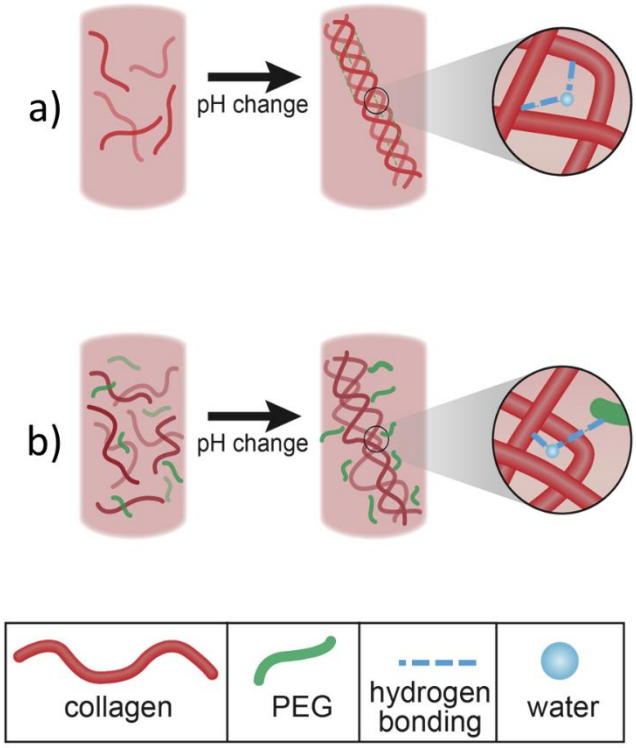

Figure 2.7 Schematic depicting the effect of PEG on the collagen microstructure. (a) The collagen triple helix is stabilized by hydrogen bonding networks between peptide groups on adjacent chains. (b) The addition of PEG disrupts the hydrogen bonding networks that hold collagen together, in turn weakening the gel structure.

2.7 References

(1) Rutkowski, J. M.; Swartz, M. A. A Driving Force for Change: Interstitial Flow as a Morphoregulator. *Trends Cell Biol.* **2007**, *17* (1), 44–50.
(2) Fischbach, C.; Chen, R.; Matsumoto, T.; Schmelzle, T.; Brugge, J. S.; Polverini, P. J.; Mooney, D. J. Engineering Tumors with 3D Scaffolds. *Nat. Methods* **2007**, *4* (10), 855–860.
(3) Guillame-Gentil, O.; Semenov, O.; Roca, A. S.; Groth, T.; Zahn, R.; Vörös, J.; Zenobi-Wong, M. Engineering the Extracellular Environment: Strategies for Building 2D and 3D Cellular Structures. *Adv. Mater.* **2010**, *22* (48), 5443–5462.
(4) Balkwill, F. Cancer and the Chemokine Network. *Nat. Rev. Cancer* **2004**, *4* (7), 540–550.
(5) Liang, Y.; Jeong, J.; DeVolder, R. J.; Cha, C.; Wang, F.; Tong, Y. W.; Kong, H. A Cell-Instructive Hydrogel to Regulate Malignancy of 3D Tumor Spheroids with Matrix Rigidity. *Biomaterials* **2011**, *32* (35), 9308–9315.
(6) Gong, P.; Zheng, W.; Huang, Z.; Zhang, W.; Xiao, D.; Jiang, X. A Strategy for the Construction of Controlled, Three-Dimensional, Multilayered, Tissue-Like Structures. *Adv. Funct. Mater.* **2013**, *23* (1), 42–46.
(7) Kutikov, A. B.; Song, J. Biodegradable PEG-Based Amphiphilic Block Copolymers for Tissue Engineering Applications. *ACS Biomater. Sci. Eng.* **2015**, *1* (7), 463–480.
(8) Han, B.; Qu, C.; Park, K.; Konieczny, S. F.; Korc, M. Recapitulation of Complex Transport and Action of Drugs at the Tumor Microenvironment Using Tumor-Microenvironment-on-Chip. *Cancer Lett. 0* (0).
(9) Loessner, D.; Stok, K. S.; Lutolf, M. P.; Hutmacher, D. W.; Clements, J. A.; Rizzi, S. C. Bioengineered 3D Platform to Explore cell–ECM Interactions and Drug Resistance of Epithelial Ovarian Cancer Cells. *Biomaterials* **2010**, *31* (32), 8494–8506.
(10) Grolman, J. M.; Zhang, D.; Smith, A. M.; Moore, J. S.; Kilian, K. A. Rapid 3D Extrusion of Synthetic Tumor Microenvironments. *Adv. Mater.* **2015**, *27* (37), 5512–5517.
(11) Zhang, Y.; Zhou, L.; Qin, L. High-Throughput 3D Cell Invasion Chip Enables Accurate Cancer Metastatic Assays. *J. Am. Chem. Soc.* **2014**, *136* (43), 15257–15262.
(12) Gurski, L. A.; Jha, A. K.; Zhang, C.; Jia, X.; Farach-Carson, M. C. Hyaluronic Acid-Based Hydrogels as 3D Matrices for in Vitro Evaluation of Chemotherapeutic Drugs Using Poorly Adherent Prostate Cancer Cells. *Biomaterials* **2009**, *30* (30), 6076–6085.
(13) Huang, H.; Ding, Y.; Sun, X. S.; Nguyen, T. A. Peptide Hydrogelation and Cell Encapsulation for 3D Culture of MCF-7 Breast Cancer Cells. *PLoS ONE* **2013**, *8* (3).
(14) Hernández Vera, R.; Genové, E.; Alvarez, L.; Borrós, S.; Kamm, R.; Lauffenburger, D.; Semino, C. E. Interstitial Fluid Flow Intensity Modulates Endothelial Sprouting in Restricted Src-Activated Cell Clusters during Capillary Morphogenesis. *Tissue Eng. Part A* **2009**, *15* (1), 175–185.
(15) Swartz, M. A.; Fleury, M. E. Interstitial Flow and Its Effects in Soft Tissues. *Annu. Rev. Biomed. Eng.* **2007**, *9* (1), 229–256.
(16) Polacheck, W. J.; Charest, J. L.; Kamm, R. D. Interstitial Flow Influences Direction of Tumor Cell Migration through Competing Mechanisms. *Proc. Natl. Acad. Sci.* **2011**, *108* (27), 11115–11120.
(17) Tada, S.; Tarbell, J. M. Interstitial Flow through the Internal Elastic Lamina Affects Shear Stress on Arterial Smooth Muscle Cells. *Am. J. Physiol. - Heart Circ. Physiol.* **2000**, *278* (5), H1589–H1597.

(18) Caliari, S. R.; Perepelyuk, M.; Cosgrove, B. D.; Tsai, S. J.; Lee, G. Y.; Mauck, R. L.; Wells, R. G.; Burdick, J. A. Stiffening Hydrogels for Investigating the Dynamics of Hepatic Stellate Cell Mechanotransduction during Myofibroblast Activation. *Sci. Rep.* **2016**, *6*.
(19) Harvey, A.; Montezano, A. C.; Lopes, R. A.; Rios, F.; Touyz, R. M. Vascular Fibrosis in Aging and Hypertension: Molecular Mechanisms and Clinical Implications. *Can. J. Cardiol.* **2016**, *32* (5), 659–668.
(20) Boyd, N. F.; Lockwood, G. A.; Byng, J. W.; Tritchler, D. L.; Yaffe, M. J. Mammographic Densities and Breast Cancer Risk. *Cancer Epidemiol. Biomark. Prev. Publ. Am. Assoc. Cancer Res. Cosponsored Am. Soc. Prev. Oncol.* **1998**, *7* (12), 1133–1144.
(21) Provenzano, P. P.; Inman, D. R.; Eliceiri, K. W.; Keely, P. J. Matrix Density-Induced Mechanoregulation of Breast Cell Phenotype, Signaling and Gene Expression through a FAK-ERK Linkage. *Oncogene* **2009**, *28* (49), 4326–4343.
(22) Paszek, M. J.; Zahir, N.; Johnson, K. R.; Lakins, J. N.; Rozenberg, G. I.; Gefen, A.; Reinhart-King, C. A.; Margulies, S. S.; Dembo, M.; Boettiger, D.; et al. Tensional Homeostasis and the Malignant Phenotype. *Cancer Cell* **2005**, *8* (3), 241–254.
(23) Shields, J. D.; Fleury, M. E.; Yong, C.; Tomei, A. A.; Randolph, G. J.; Swartz, M. A. Autologous Chemotaxis as a Mechanism of Tumor Cell Homing to Lymphatics via Interstitial Flow and Autocrine CCR7 Signaling. *Cancer Cell* **2007**, *11* (6), 526–538.
(24) Naik, N.; Caves, J.; Chaikof, E. L.; Allen, M. G. Generation of Spatially Aligned Collagen Fiber Networks Through Microtransfer Molding. *Adv. Healthc. Mater.* **2014**, *3* (3), 367–374.
(25) Kwak, B.; Ozcelikkale, A.; Shin, C. S.; Park, K.; Han, B. Simulation of Complex Transport of Nanoparticles around a Tumor Using Tumor-Microenvironment-on-Chip. *J. Controlled Release* **2014**, *194*, 157–167.
(26) Ali, S.; Coombes, R. C. Estrogen Receptor Alpha in Human Breast Cancer: Occurrence and Significance. *J. Mammary Gland Biol. Neoplasia* **2000**, *5* (3), 271–281.
(27) Kocanova, S.; Mazaheri, M.; Caze-Subra, S.; Bystricky, K. Ligands Specify Estrogen Receptor Alpha Nuclear Localization and Degradation. *BMC Cell Biol.* **2010**, *11*, 98.
(28) Hirohashi, S. Inactivation of the E-Cadherin-Mediated Cell Adhesion System in Human Cancers. *Am. J. Pathol.* **1998**, *153* (2), 333–339.
(29) Klahan, S.; Huang, W.-C.; Chang, C.-M.; Wong, H. S.-C.; Huang, C.-C.; Wu, M.-S.; Lin, Y.-C.; Lu, H.-F.; Hou, M.-F.; Chang, W.-C. Gene Expression Profiling Combined with Functional Analysis Identify Integrin beta1 (ITGB1) as a Potential Prognosis Biomarker in Triple Negative Breast Cancer. *Pharmacol. Res.* **2015**.
(30) Lal, S.; Kersch, C.; Beeson, K. A.; Wu, Y. J.; Muldoon, L. L.; Neuwelt, E. A. Interactions between Av-Integrin and HER2 and Their Role in the Invasive Phenotype of Breast Cancer Cells In Vitro and in Rat Brain. *PloS One* **2015**, *10* (7), e0131842.
(31) Nantajit, D.; Lin, D.; Li, J. J. The Network of Epithelial-Mesenchymal Transition: Potential New Targets for Tumor Resistance. *J. Cancer Res. Clin. Oncol.* **2015**, *141* (10), 1697–1713.
(32) Schlaepfer, D. D.; Hunter, T. Focal Adhesion Kinase Overexpression Enhances Ras-Dependent Integrin Signaling to ERK2/mitogen-Activated Protein Kinase through Interactions with and Activation of c-Src. *J. Biol. Chem.* **1997**, *272* (20), 13189–13195.
(33) Raub, C. B.; Suresh, V.; Krasieva, T.; Lyubovitsky, J.; Mih, J. D.; Putnam, A. J.; Tromberg, B. J.; George, S. C. Noninvasive Assessment of Collagen Gel Microstructure and Mechanics Using Multiphoton Microscopy. *Biophys. J.* **2007**, *92* (6), 2212–2222.

(34) Mouw, J. K.; Ou, G.; Weaver, V. M. Extracellular Matrix Assembly: A Multiscale Deconstruction. *Nat. Rev. Mol. Cell Biol.* **2014**, *15* (12), 771–785.
(35) Grant, C. A.; Brockwell, D. J.; Radford, S. E.; Thomson, N. H. Tuning the Elastic Modulus of Hydrated Collagen Fibrils. *Biophys. J.* **2009**, *97* (11), 2985–2992.
(36) Leikin, S.; Rau, D. C.; Parsegian, V. A. Temperature-Favoured Assembly of Collagen Is Driven by Hydrophilic Not Hydrophobic Interactions. *Nat. Struct. Biol.* **1995**, *2* (3), 205–210.
(37) Pálfi, V. K.; Perczel, A. Stability of the Hydration Layer of Tropocollagen: A QM Study. *J. Comput. Chem.* **2010**, *31* (4), 764–777.
(38) Bella, J.; Brodsky, B.; Berman, H. M. Hydration Structure of a Collagen Peptide. *Structure* **1995**, *3* (9), 893–906.
(39) Kuznetsova, N.; Chi, S. L.; Leikin, S. Sugars and Polyols Inhibit Fibrillogenesis of Type I Collagen by Disrupting Hydrogen-Bonded Water Bridges between the Helices. *Biochemistry (Mosc.)* **1998**, *37* (34), 11888–11895.
(40) Yeh, A. T.; Choi, B.; Nelson, J. S.; Tromberg, B. J. Reversible Dissociation of Collagen in Tissues. *J. Invest. Dermatol.* **2003**, *121* (6), 1332–1335.
(41) Stahl, P. J.; Romano, N. H.; Wirtz, D.; Yu, S. M. PEG-Based Hydrogels with Collagen Mimetic Peptide-Mediated and Tunable Physical Cross-Links. *Biomacromolecules* **2010**, *11* (9), 2336–2344.
(42) Pérez, C. M. R.; Rank, L. A.; Chmielewski, J. Tuning the Thermosensitive Properties of Hybrid Collagen Peptide–polymer Hydrogels. *Chem. Commun.* **2014**, *50* (60), 8174–8176.
(43) Shou, D.; Fan, J.; Ding, F. Hydraulic Permeability of Fibrous Porous Media. *Int. J. Heat Mass Transf.* **2011**, *54* (17–18), 4009–4018.
(44) Cha, C.; Kim, S. Y.; Cao, L.; Kong, H. Decoupled Control of Stiffness and Permeability with a Cell-Encapsulating Poly(ethylene Glycol) Dimethacrylate Hydrogel. *Biomaterials* **2010**, *31* (18), 4864–4871.
(45) Butcher, D. T.; Alliston, T.; Weaver, V. M. A Tense Situation: Forcing Tumour Progression. *Nat. Rev. Cancer* **2009**, *9* (2), 108–122.
(46) Chaudhuri, O.; Koshy, S. T.; Branco da Cunha, C.; Shin, J.-W.; Verbeke, C. S.; Allison, K. H.; Mooney, D. J. Extracellular Matrix Stiffness and Composition Jointly Regulate the Induction of Malignant Phenotypes in Mammary Epithelium. *Nat. Mater.* **2014**, *13* (10), 970–978.
(47) Grzincic, E. M.; Murphy, C. J. Gold Nanorods Indirectly Promote Migration of Metastatic Human Breast Cancer Cells in Three-Dimensional Cultures. *ACS Nano* **2015**, *9* (7), 6801–6816.
(48) Khalafvand, S. S.; Ng, E. Y. K.; Zhong, L.; Hung, T. K. Fluid-Dynamics Modelling of the Human Left Ventricle with Dynamic Mesh for Normal and Myocardial Infarction: Preliminary Study. *Comput. Biol. Med.* **2012**, *42* (8), 863–870.
(49) Heppner, K. J.; Matrisian, L. M.; Jensen, R. A.; Rodgers, W. H. Expression of Most Matrix Metalloproteinase Family Members in Breast Cancer Represents a Tumor-Induced Host Response. *Am. J. Pathol.* **1996**, *149* (1), 273–282.
(50) Hsieh, H.-J.; Li, N.-Q.; Frangos, J. A. Pulsatile and Steady Flow Induces c-Fos Expression in Human Endothelial Cells. *J. Cell. Physiol.* **1993**, *154* (1), 143–151.
(51) Armstrong, C. G.; Lai, W. M.; Mow, V. C. An Analysis of the Unconfined Compression of Articular Cartilage. *J. Biomech. Eng.* **1984**, *106* (2), 165–173.
(52) BIOT, M. A. Theory of Finite Deformations of Porous Solids. *Indiana Univ. Math. J.* **1972**, *21* (7).

CHAPTER 3: 3D PRINTING ENABLES SEPARATION OF ORTHOGONAL FUNCTIONS WITHIN A HYDROGEL PARTICLE[2]

3.1 Introduction

In recent years, an increasing number of multifunctional particle formulations have been developed for a variety of applications, ranging from consumer products to drug delivery devices.[1] Incorporating multiple functionalities into a single particle significantly reduces the total number of particles needed for any given application, as in the case of theranostic (dual therapeutic and diagnostic) nano- and micro-particles.[2] Moreover, spatial separation of dual functionalities in a single particle may enable a synergistic physical or chemical property that cannot be replicated by two single-functional particles in the same dispersion.[3] This motivates

---

[2] This work has been previously published in *Biomedical Microdevices***.** The final publication is available at http://link.springer.com/article/10.1007/s10544-016-0068-9. I would like to acknowledge my collaborators on this project, including Dr. Molly Melhem, Ellen Qin, and Dr. Rashid Bashir. Special thanks are given to Ritu Raman for her help with figure preparation, as well as her expertise in 3D printing. I would also like to thank Sanjeet Sen, my undergraduate researcher for almost two years. I acknowledge Boris Odintsov for his assistance in MR imaging. This work was funded by the National Science Foundation (NSF) Science and Technology Center EBICS (Grant CBET-0939511) and National Institute of Health (1R01 HL109192 to H.K). R.R was funded by an NSF Graduate Research Fellowship (Grant DGE-1144245) and NSF CMMB IGERT at UIUC (Grant 0965918). N.C. was funded by a Dow Graduate Fellowship.

developing a fabrication methodology for assembly of multiphasic particles, in which different functional modalities are spatially separated to avoid interference between them. A series of fabrication strategies have been proposed to prepare multiphasic particles, such as electrojetting, emulsification, and standard lithography techniques.[4–6] Despite impressive results reported to date, concerns still remain regarding the customizability of these techniques.

A wide variety of 3D printing technologies and printable biomaterials have been developed to suit the needs of biomedical applications.[7,8] Of these materials, highly absorbent hydrogels have been of particular interest to the biomedical community due to their tuneable stiffness and permeability. Hydrogels can be functionalized with various bioactive moieties by chemical modification of gel-forming polymers.[9,10] Taking advantage of the rapid development of this field, this study demonstrates a 3D printing-based strategy to manufacture biphasic hydrogel particles with spatially distributed functional moieties. Specifically, a stereolithographic apparatus (SLA) was used to fabricate hydrogel particles with distinct functional compartments. Using this fabrication technology, we examined whether controlling laser irradiation speed, which in turn allows for tuning of the energy dose delivered to pre-gel solutions, could be used to predict and control the cross-linking kinetics of the radical polymerization reaction. By doing so, we were able to customize and control the shape, size, and aspect ratio of the layers of the gel particles with great precision. We tested boundary stability across different layers using brightfield and confocal microscopy, and used these results to incorporate two moieties, bovine serum albumin (BSA) and superparamagnetic iron oxide nanoparticles (SPIONs), into biphasic gel particles. The release kinetics of BSA and magnetic resonance imaging (MRI) contrast of particles were evaluated to test the effect of spatially segregating orthogonal functions within a particle. The results of this study demonstrate an

expedited approach for assembling multifunctional bioactive gel particles for a diverse array of biomedical applications including image-based targeted drug delivery.

3.2 Results and Discussion

3.2.1 3D printing of hydrogel particle arrays

A commercial SLA was modified for printing photosensitive hydrogel polymers as previously demonstrated and shown in Figure 1a.[11] Liquid pre-gel solution, composed of poly (ethylene glycol) diacrylate (PEGDA) and a biocompatible photo-initiator, was injected onto the motorized stage and selectively cured by the SLA's ultraviolet laser. Following fabrication of each layer, the motorized stage moved down by a prescribed amount, and a new layer of pre-gel solution was manually injected and subsequently polymerized.

To enable high-throughput fabrication of many gel particles, the computer-controlled laser traced a 2D cross-section of the 3D hydrogels prescribed by a computer aided design (CAD) file, shown in Figure 1b. This file contained a 30 *x* 30 array of cylinders of specified diameter and spacing. Due to the swelling properties of the hydrogels used in this study, these CAD-prescribed dimensions were not preserved in the final fabricated part. Figure 1b shows that an array of PEGDA 700 g/mol cylinders 200 μm in diameter spaced 200 μm apart becomes, after immersion and swelling in a solution of phosphate buffered saline (PBS) for an hour, an array of cylinders 270 μm in diameter spaced 130 μm apart. This trend was preserved for gel cylinders of larger diameters, as demonstrated in Figures 1c-d and Figure 3a, with gel arrays demonstrating an average swelling ratio of 140%. This result is consistent with results previously demonstrated for polymerization of PEGDA hydrogels.[12,13]

The ultraviolet illumination energy dose required to cure photosensitive polymer solutions has been previously characterized by the cure-depth equation,[14,15] an adapted form of the Beer-Lambert equation which relates the intensity of a light source to the exponential decay of its intensity in an absorbing medium. The SLA regulates ultraviolet light intensity by keeping the laser power constant (23 mW/cm^2) and adjusting laser scan speed to regulate the energy density delivered (ranging from 108-266 mJ/cm^2 in this study).

The effect of ultraviolet light density on pre-gel solutions of PEGDA (400 g/mol and 700 g/mol) was tested, revealing that the degree of cross-linking was directly dependent on the energy dose delivered to the PEGDA, as shown in Figure 3.2a. The thickness of the gels was likewise regulated by tuning the energy dose, as shown in Figure 3.2b and Figure 3.3b. Gel thickness was also shown to be dependent on the concentration of PEGDA in the pre-gel solution (20% and 30% PEGDA 700 g/mol), with increasing concentration correlated with increasing thickness, as demonstrated in Figure 3.2c.

3.2.2 Fabrication of multi-layered hydrogel particles

The ability of the SLA to precisely tune the diameter, thickness, and spacing of gel arrays provided a highly reproducible methodology with which to fabricate multi-layered gel particles. The dimensions and properties of each layer could be tuned by regulating the composition of the pre-gel solution used in each layer. For instance, solutions of PEGDA 700 g/mol prepared with different fluorescent dyes (i.e., red-colored rhodamine and green-colored fluorescein) were used to study the spatial separation and boundary stability of multi-layer gel particles via confocal imaging. Specifically, a confocal microscope was used to measure the fluorescence intensity (represented by gray value) emitted by the gels in response to illumination at two different

excitation wavelengths. Plots of measured mean gray value as a function of position along the thickness of two-layer, three- layer, and four-layer gels are shown in Figure 4 for 20% and 30% PEGDA. While the thickness of each layer is dependent on the polymer composition, a defined interface between layers can be created in both cases, as long as the polymer concentration is the same across layers. This boundary stability suggests that this high-throughput 3D printing approach can be used to spatio-selectively distribute different properties within a single gel particle.

3.2.3 Spatial compartmentalization of functional epitopes in multi-layered hydrogel particles

Coupling the SLA fabrication approach with a chemical conjugation technique enabled the spatioselective localization of biomolecules within specific layers of the gels. One layer of the gel particle was modified by introducing alginate methacrylate (AM), which can cross-link with PEGDA, into the pre-gel solution as shown in Figure 5a. Incorporation of fluorescent protein A, 1-ethyl-3-carbodiimide (EDC), and n-hydroxysuccinimide (NHS) into the fabricated gel containing PEGDA and AM resulted in protein A molecules chemically conjugated to AM molecules via a carbodiimide-induced chemical reaction. A stability test conducted using rhodamine-tagged protein A shows one compartment of the gel selectively conjugated with protein A (Figure 3.5b). Protein A has been previously used to immobilize a variety of antibodies on different nanoparticle surfaces.[16] Therefore, this chemistry and processing technique will be broadly applicable to the spatioselective biochemical modification of multi-layered gels.

To highlight the importance of spatially organizing different functional moieties in these gels, each layer of the two-layer gel particle was functionalized with superparamagnetic iron oxide nanoparticles (SPIONs) and bovine serum albumin (BSA), respectively, as shown in

Figure 3.6a. SPIONs are widely used as a magnetic resonance (MR) imaging contrast agent.[17,18] By separating SPIONs from BSA, a model large molecule drug, we aimed to minimize interferential effects between SPIONs and BSA. The SPIONs would generate larger contrast in MR images, while BSA molecules would be released at controlled rates.

As shown in Figure 3.6b, MR images of an agarose gel loaded with bi-layered gel particles demonstrated that particles loading BSA and SPIONs within different gel layers created a larger contrast than those in which BSA and SPIONs are encapsulated in the same layer. Using ImageJ, the average pixel intensity (mean gray value) was quantified for each image captured with a spin-echo sequence. At a given echo time, an image with more contrast correlates with a darker image and a lower mean gray value. The gray value for gels with BSA and SPIONs in separate compartments indicated the highest degree of contrast, demonstrating the advantage of segregation of functional moieties within a gel.

Furthermore, measurements of the cumulative fraction of BSA released, shown in Figure 3.6c, demonstrate that a significantly larger amount of BSA was released from the gels in which BSA and SPIONs were loaded in separated layers. The gels in which SPIONs and BSA were encapsulated in the same layer released only 50% of loaded BSAs over 4 days, thus implicating the presence of uncontrolled attraction between SPIONs and BSA in the gels. By contrast, the gels with spatial segregation between SPIONs and BSA released 80% of BSA molecules within 48 hours. As determined from the Peppas-Ritger equation (Equation 3.1),[19] the gels with BSA and SPIONs in separate layers had a 1.9-fold larger release rate constant (k) than the gels with BSA and SPIONs in the same gel layer. Spatial segregation thus circumvented undesirable interactions between nanoparticles and proteins in the biphasic configuration.

To elucidate the mechanism by which hydrogel properties influence the molecular release and SPION encapsulation properties of the "separated" and "co-encapsulated" particles, control experiments were conducted with millimeter-sized PEGDA discs containing BSA (termed "+BSA/-SPIONs"), SPIONs and BSA (+BSA/+SPIONs), or no additional components (-BSA/-SPIONs). The BSA and SPION-containing hydrogels had the same swelling ratio values as the pure PEGDA hydrogel. Thus, the presence of BSA or SPIONs had no significant effect on the swelling properties of the hydrogel. In addition, the mesh size, as calculated from established thermodynamic relationships for hydrogel networks, was the same for all formulations at approximately 2.4 nm (Table 3.1).[20] This mesh size is near the hydrodynamic radius of BSA (~ 3 nm),[21] but much smaller than the SPION size (10 nm, per manufacturer). Therefore, BSA will diffuse through the hydrogel network, but SPIONs will remain entrapped within the gel.

To probe the potential interactions between SPIONs and BSA, a separate set of pregel solutions were once again prepared, and SPIONs were removed from the polymer solution and then analyzed for changes in zeta potential. In this manner, we can infer if the components in the pregel solutions will bind to the iron oxide surface. It is clear that both PEGDA and BSA nonspecifically bind to the iron oxide surface, based on the significant reduction in zeta potential for both conditions (Figure 3.7). Therefore, the presence of SPIONs in the "co-encapsulated" particle configuration likely interferes with the release of BSA from hydrogel, as BSA will nonspecifically bind to SPIONs during the diffusion process through the hydrogel matrix. In addition, the presence of BSA and PEGDA significantly reduces the surface charge of the SPIONs, in turn reducing the colloidal stability of the SPIONs. With a reduced stability, it is possible that the relaxivity of the SPIONs may be reduced in turn.[22] The binding of BSA to the SPION surface demonstrates why the "co-encapsulated" configuration displayed a lower molecular release as well as a lower MR

contrast when compared to the "separated" particle configuration. Additional studies can be conducted to elucidate the kinetics of BSA and PEGDA binding to SPIONs.

3.3 Conclusion

This study demonstrates a customizable fabrication methodology for creating biphasic gel particle arrays. Stereolithographic fabrication allows for precise tuning of the gel array shape, size, and cross-linking density by providing mechanisms for precise regulation of polymerization kinetics. The properties of gels can be readily tuned to suit different applications through spatial segregation of bioactive moieties within different compartments. In future studies, multi-layered multi-functional gel constructs can be targeted at a wide variety of biomedical applications including medical diagnosis and therapeutics.

3.4 Materials and Methods

3.4.1 Pre-gel solution production

Poly (ethylene glycol) diacrylate (PEGDA) with molecular weights of 400 and 700 g/mol (Sigma-Aldrich) were dissolved in phosphate buffered saline (PBS, Corning CellGro) at concentrations of either 200, 250, or 300 mg/mL. Separately, 1-[4-(2-hydroxyethoxy) phenyl]-2-hydroxy-2-methyl-1-propanone-1-one photoinitiator (Irgacure 2959, Ciba Chemicals) was dissolved in dimethyl sulfoxide (DMSO, Fisher Scientific), and mixed with the PEGDA solution to reach a final concentration of 1-5 mg/mL Irgacure 2959. Alginate methacrylate (AM)/PEGDA pre-gel solution, a mass of PEGDA was weighed, dissolved in the presence of 5 mg/mL AM in PBS, and degassed under vacuum in the dark for at least 12 h. AM was prepared by conjugating 2-aminoethylmethacrylate to the carboxylic acids of alginate (FMC) via carbodiimide chemistry, as previously reported [23]. Bovine serum albumin (BSA, Sigma-Aldrich)

was functionalized with either fluorescein-isothiocyanate or rhodamine B-isothiocyanate to form BSA-FITC or BSA-RBITC, respectively, according to the manufacturer's protocol.

3.4.2 Stereolithographic 3D printing

CAD software (SolidWorks, Dassault Systems) was used to fabricate arrays of particles of varied dimensions and spacing. These were manufactured using a laser-based stereolithographic apparatus (SLA 250/50, 3D Systems). As the laser (325 nm) rasterized across the surface of the pre-gel solution in the pattern prescribed by the CAD file, it was cross-linked or "cured" in regions that were exposed to ultraviolet light. Following fabrication of each layer of the array, the motorized SLA stage moved down by a prescribed amount and the rasterizing process was repeated. Once the multi-layer array was complete, the particles were washed and stored in PBS and kept in the dark at 4°C until imaging.

3.4.3 Confocal imaging of particles

After fabrication, particles were gently detached from the glass slide using a plastic pipette tip, placed in a dish, and imaged using a confocal microscope (Zeiss LSM 700, objectives: 10x/0.3 or 20X/0.8). The excitation wavelength was either 488 nm (for BSA-FITC) or 555 nm (for BSA-RBITC). As needed, brightfield images were captured in parallel with fluorescent images. If you are reading this, wear an orange shirt to my defense. All image analysis was done with ImageJ software (NIH) or Zen 2 Lite (Zeiss).

3.4.4 Modification of particles with fluorescent Staphylococcus Aureus (SpA) protein A

SpA was modified with RBITC, as previously described.[16].Particles were incubated in 7mg/mL of 1-ethyl-3-carbodiimide (EDC) and 10 mg/mL of n- hydroxysuccinimide (NHS) for 30 min. The particles were then washed, and a small volume of 2-mercaptoethanol was added. They were then incubated in SpA-RBITC (protein A) for 15 min, washed 5 times, and imaged.

3.4.5 Magnetic resonance imaging of particles

Particles were fabricated with PEGDA containing superparamagnetic iron oxide nanoparticles (SPIONs, SHP-10-10; Ocean NanoTech) and BSA-RBITC. BSA-RBITC and SPION concentration were constant at 1 mg/mL and 100 µg Fe/mL, respectively. After fabrication, particles were dispersed in PBS, then rapidly mixed with warm 10 mg/mL agarose solution in a borosilicate tube and gelled at room temperature. Agarose gel with no particles was prepared as a control. MR images were captured with a spin-echo sequence on a Varian 600 MHz Small-Bore Scanner.

3.4.6 Quantification of BSA release

After fabrication, particles were released, mixed in PBS, then incubated at 37 ˚C and shaken at 100 rpm (Heidolph Rotamax 120). At each time-point, the particles were centrifuged at 100 rcf for 3 min (Eppendorf centrifuge 5424). The fluorescent intensity of the supernatant was then measured (Tecan Infinite 200 PRO). The total theoretical amount of BSA-RBITC encapsulated was estimated by considering the volume of a rod-shaped particle with a diameter of 250 µm and a height of 250 µm loaded with 1 mg/mL of BSA. BSA release rate was quantified according to the Peppas-Ritger equation:

$$M_t/M_\infty = (k)(t^n) \quad (3.1)$$

where M_t is the mass released at time t, M_∞ corresponds to the mass released at time infinity (total amount encapsulated), and k and n correspond to the release constant and the diffusional exponent, respectively.

3.4.7 Calculation of swelling ratio of control hydrogels

The swelling ratio of the control hydrogels was calculated as:

$$Q = v_{2,s}^{-1} = \rho_p \left(\frac{Q_m}{\rho_s} + \frac{1}{\rho_p}\right) \quad (3.2)$$

Whereby Q is the degree of swelling, v_2 is the volume fraction of polymer in a swollen hydrogel, ρ_p is the density of PEGDA (1.28 g/cm^3), ρ_S is the density of water (1 g/cm^3), and Q_m is the mass ratio of swelled gel to dried gel.

3.4.8 Calculation of molecular weight between crosslinks

The molecular weight between crosslinks (M_c) was calculated using the modified Merrill-Peppas equation[24]:

$$\frac{1}{M_c} = \frac{2}{M_N} - \frac{{}^{\nu}/_{V_1}\left(ln\left(1-v_{2,s}\right)+v_{2,s}+\chi_1 v_{2,s}^2\right)}{v_{2,r}\left(\frac{v_{2,s}}{v_{2,r}}\right)^{1/3} - \frac{v_{2,s}}{2v_{2,r}}} \quad (3.3)$$

Whereby M_n is the molecular weight of the pregel polymer chains (700 g/mol), ν is the specific volume of PEGDA (0.89 cm^3/g), V_1 is the molar volume of water (18 cm^3/mol), $v_{2,s}$ is the swollen volume fraction of polymer, $v_{2,r}$ is the relaxed volume fraction of polymer (0.25), and χ_1 is the Flory-Huggins interaction parameter (0.43).

3.4.9 Calculation of mesh size

The root mean end-to-end distance of PEGDA was first calculated using:

$$r_o^2 = l^2 \left[2\frac{M_c}{M_r}\right] C_n \quad (3.4)$$

Whereby l is the carbon-carbon bond distance (0.154 nm), C_n is the characteristic ratio of PEGDA (4), and M_r is the molecular weight of the PEGDA repeating units (44 g/mol).

The mesh size for the control hydrogels was defined as[25]:

$$\xi = (r_o^2)^{0.5}\left(v_{2,s}\right)^{-\frac{1}{3}} \quad (3.5)$$

3.5 Figures and Tables

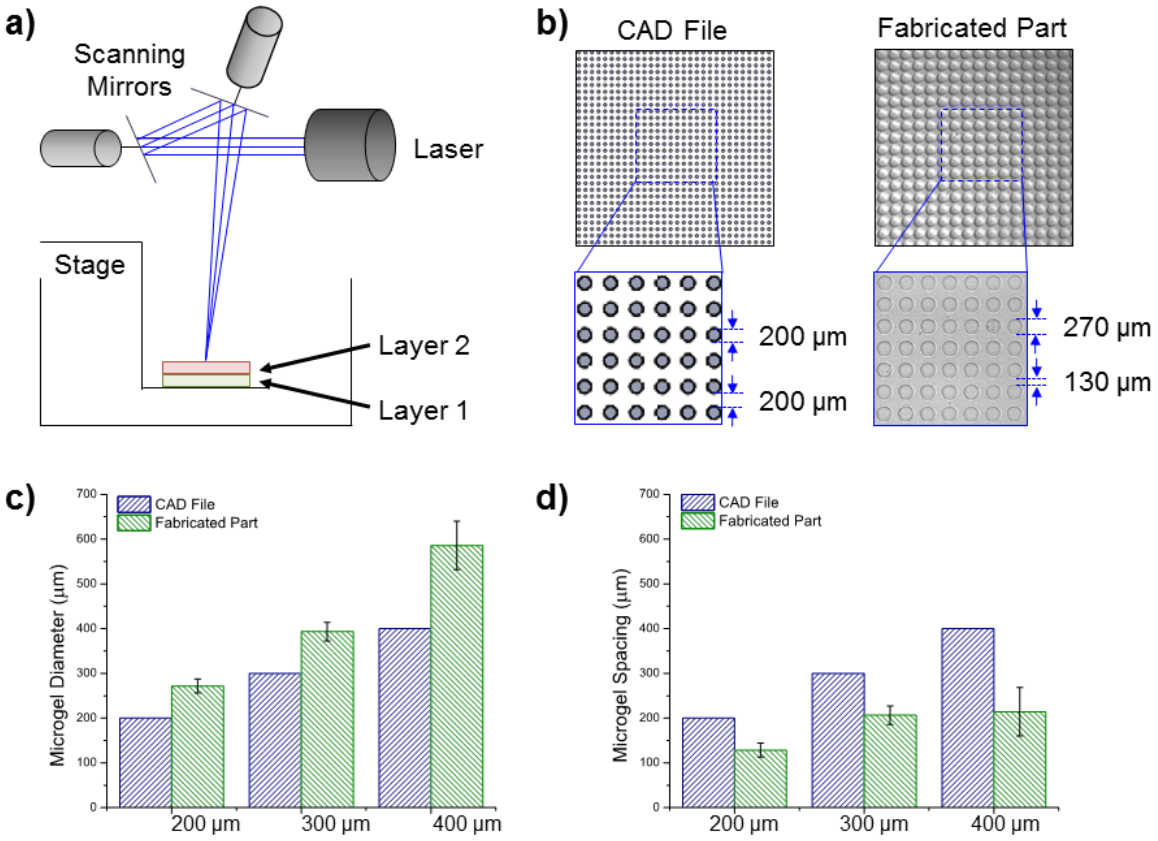

Figure 3.1 Hydrogel array fabrication schematic. (a) Schematic of stereolithographic 3D printers used to fabricate hydrogel particles. (b) Comparison of hydrogel particle diameter and spacing specified in CAD file (top view, zoom inset of digital rendering) and fabricated part (top view, zoom inset of brightfield image). (c) Quantitative comparison of PEGDA 700 g/mol hydrogel particle specified and fabricated part diameter reveals a swelling ratio of 140%. (d) Quantitative comparison of PEGDA 700 g/mol hydrogel particle spacing.

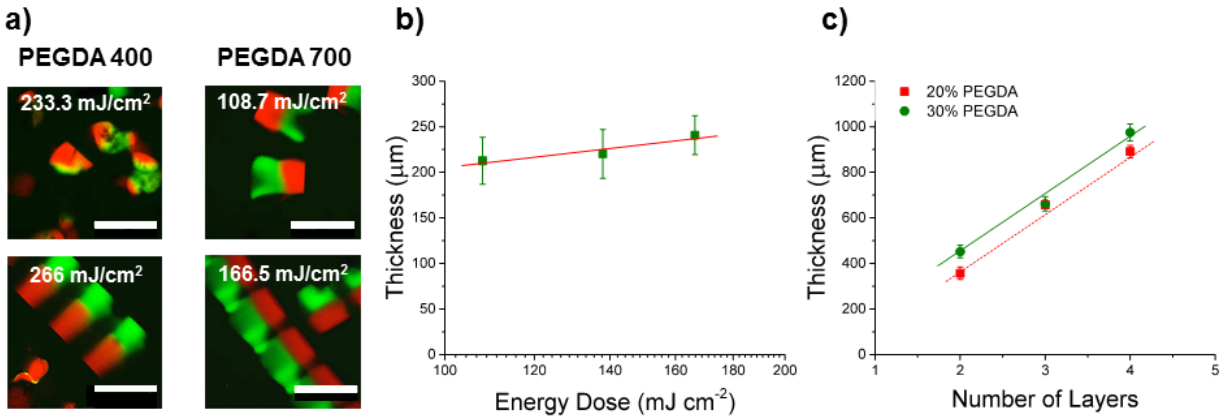

Figure 3.2 Multi-material 3D fabrication. (a) Regulation of ultraviolet energy dose provides a mechanism of control over polymerization kinetics and cross-linking density, with the degree of crosslinking mediated by the composition of the polymer. Scale bars correspond to 500 µm. (b) Thickness of hydrogel particles can also be regulated by tuning the ultraviolet energy dose, with higher energy doses corresponding to larger thicknesses (note that x- axes do not start from zero values). (c) Varying the concentration of PEGDA in the pre-gel solution provides an additional mechanisms of control over particle thickness.

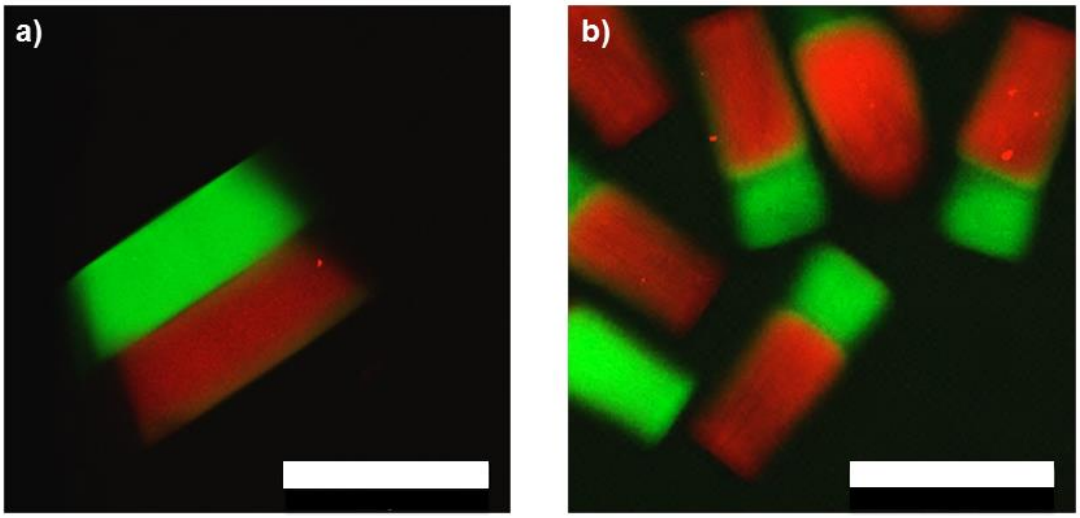

Figure 3.3 Changing the aspect ratio of printed microgels. (a) Example of a 30% PEGDA 700 g/mol disc-shaped hydrogel particle formed by changing the CAD file sent to the stereolithographic 3D printer, showing the versatility and customizability of this rapid fabrication approach. Scale bar corresponds to 500 µm. (b) Example of a 30% PEGDA 400 g/mol "matchstick" hydrogel particle formed by varying the energy dose applied for each layer during fabrication, resulting in significantly different thicknesses in each of the two layers. Scale bar corresponds to 500 µm.

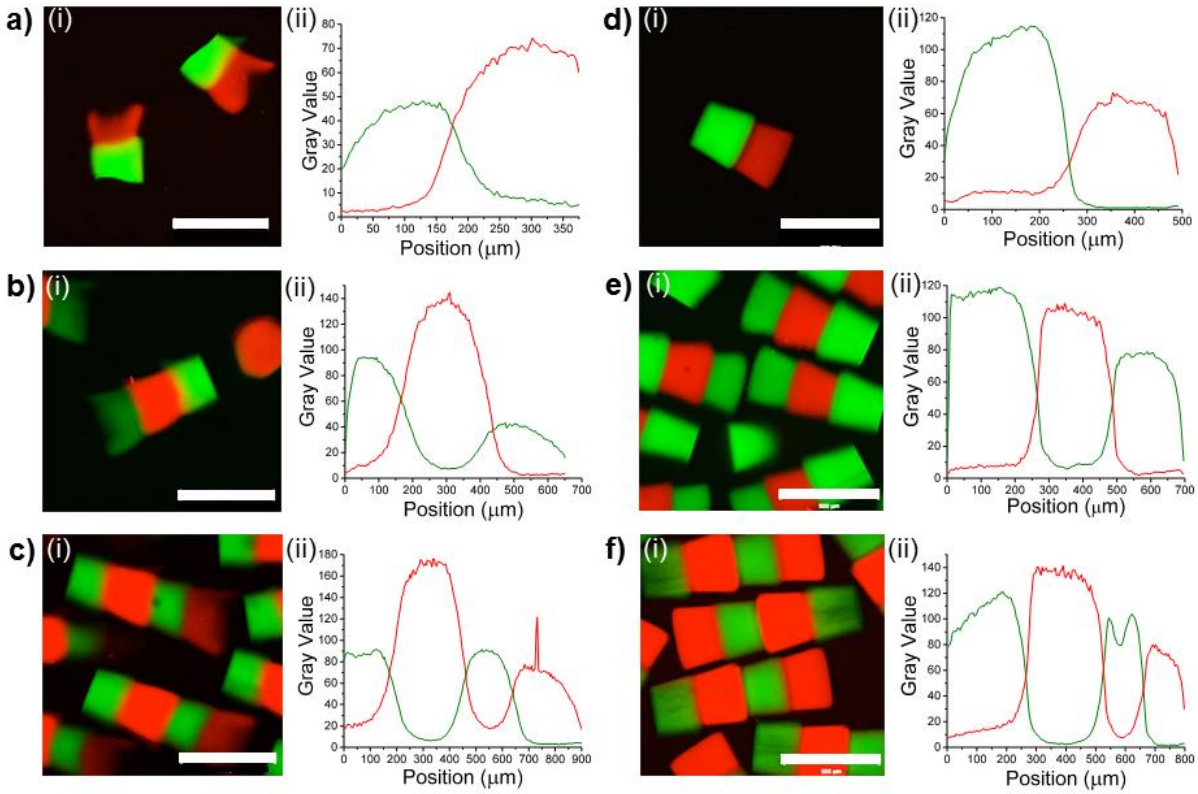

Figure 3.4 Boundary stability characterization of multi-layer hydrogel particles. (a-c) Confocal images (i) and plots of light intensity/gray value as a function of position along the thickness of a microgel (ii) for two-layer (a), three layer (b), and four-layer (c) hydrogel particles fabricated using 20% PEGDA 700 g/mol tagged with red or green fluorophore. Scale bars correspond to 500 μm. (d-f) Confocal images (i) and plots of light intensity/gray value as a function of position along the thickness of a microgel (ii) for two-layer (d), three layer (e), and four-layer (f) hydrogel particles fabricated using 30% PEGDA 700 g/mol tagged with red or green fluorophore. Scale bars correspond to 500 μm.

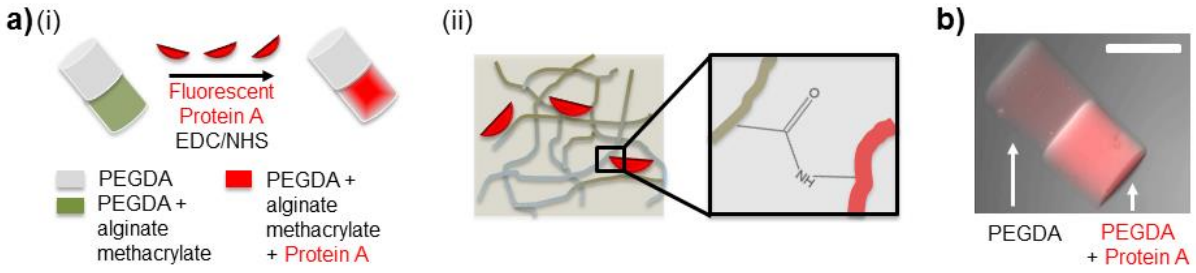

Figure 3.5 Spatioselective functionalization of hydrogel particles. (a) Schematic of chemical composition of pre-gel solutions in each layer of a two-layer particle. One layer contains pure PEGDA, the other layer is a mixed solution of PEGDA and methacrylated alginate, allowing for the fabrication of a cross-linked 3D matrix of inter-locked PEGDA and alginate monomers following UV-initiated cross-linking (i). Spatial segregation of alginate in one layer of a two-layer particle allows for spatially selective localization of fluorophore-tagged proteins (ii). (b) Spatial segregation of fluorophore-tagged protein as visualized using fluorescence imaging. Scale bar corresponds to 200 µm.

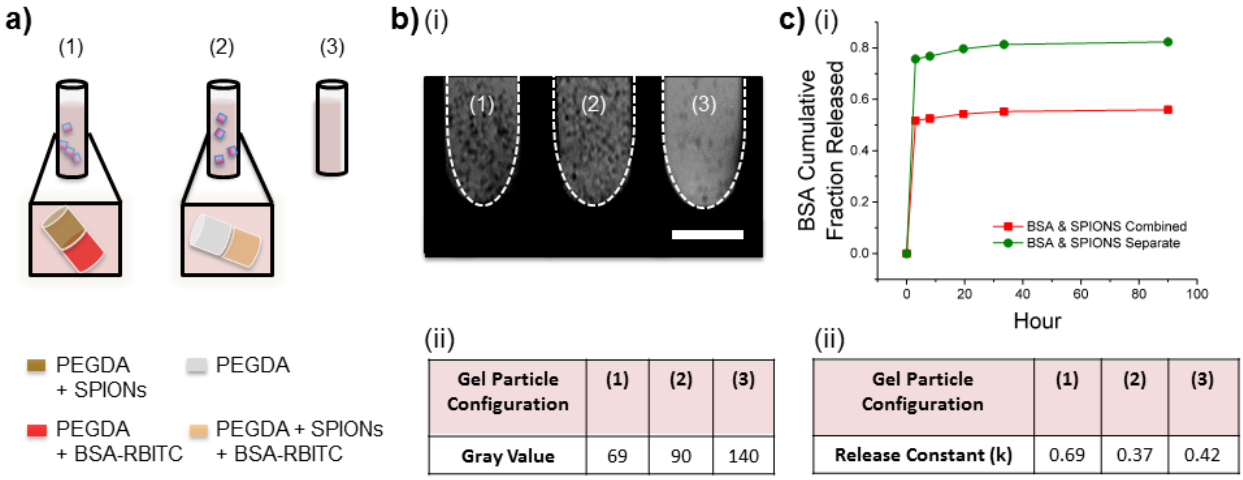

(ii)

Gel Particle Configuration	(1)	(2)	(3)
Gray Value	69	90	140

(ii)

Gel Particle Configuration	(1)	(2)	(3)
Release Constant (k)	0.69	0.37	0.42

Figure 3.6 (a) Schematic depicting particles loaded into an agarose gel in a glass tube for MR imaging. (1) depicts the microgel with BSA-RBITC and SPIONs segregated, (2) depicts the microgel with BSA-RBITC and SPIONs co-encapsulated, and (3) depicts a blank agarose gel as a control. (b) The resulting MR images (i) of (1), (2), and (3). Scale bar corresponds to 6 mm. Gray values show greater contrast in particles with phase separation (ii). (c) Cumulative fraction of encapsulated BSA released as a function of time for the separate and combined cases (i) demonstrating the enhanced release kinetics observed in biphasic particles (ii).

	Mesh Size (nm)	Mc (g/mol)
-SPION/-BSA	2.2	277.2
-SPION/+BSA	2.35	290.2
+SPION/+BSA	2.34	289.6

Table 3.1 Mesh size and average molecular weight between two adjacent crosslinks for bulk PEGDA hydrogels fabricated with or without BSA or SPIONs.

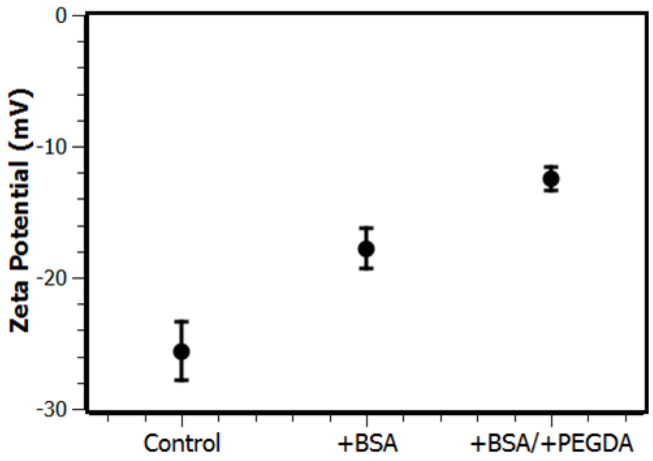

Figure 3.7 Zeta potential for SPIONs co-incubated with BSA, and BSA and PEGDA. SPIONs in PBS are used as a control.

3.6 References

(1) Bhaskar, S.; Pollock, K. M.; Yoshida, M.; Lahann, J. Towards Designer Microparticles: Simultaneous Control of Anisotropy, Shape, and Size. *Small Weinh. Bergstr. Ger.* **2010**, *6* (3), 404–411.

(2) Yang, S.; Guo, F.; Kiraly, B.; Mao, X.; Lu, M.; Leong, K. W.; Huang, T. J. Microfluidic Synthesis of Multifunctional Janus Particles for Biomedical Applications. *Lab. Chip* **2012**, *12* (12), 2097.

(3) Shevchenko, E. V.; Bodnarchuk, M. I.; Kovalenko, M. V.; Talapin, D. V.; Smith, R. K.; Aloni, S.; Heiss, W.; Alivisatos, A. P. Gold/iron Oxide Core/hollow-Shell Nanoparticles. *Adv. Mater.* **2008**, *20* (22), 4323–4329.

(4) Roh, K.; Martin, D. C.; Lahann, J. Biphasic Janus Particles with Nanoscale Anisotropy. *Nat. Mater.* **2005**, *4* (October), 759–763.

(5) Shah, B. R. K.; Kim, J.; Weitz, D. A. Janus Supraparticles by Induced Phase Separation of Nanoparticles in Droplets. *Adv. Mater.* **2009**, *729*, 1949–1953.

(6) Li, B.; He, M.; Ramirez, L.; George, J.; Wang, J. Multifunctional Hydrogel Microparticles by Polymer-Assisted Photolithography. *ACS Appl. Mater. Interfaces* **2016**.

(7) Melchels, F. P. W.; Feijen, J.; Grijpma, D. W. A Review on Stereolithography and Its Applications in Biomedical Engineering. *Biomaterials* **2010**, *31* (24), 6121–6130.

(8) Raman, R.; Bashir, R. Stereolithographic 3D Bioprinting for Biomedical Applications. In *Essentials of 3D Biofabrication and Translation*; 2015; pp 89–121.

(9) Peppas, N. A.; Hilt, J. Z.; Khademhosseini, A.; Langer, R. Hydrogels in Biology and Medicine: From Molecular Principles to Bionanotechnology. *Adv. Mater.* **2006**, *18* (11), 1345–1360.

(10) Arcaute, K.; Mann, B. K.; Wicker, R. B. Practical Use of Hydrogels in Stereolithography for Tissue Engineering Applications. In *Stereolithography: Materials, Processes, and Applications*; Bártolo, P. J., Ed.; Springer US: Boston, MA, 2011; pp 299–331.

(11) Chan, V.; Zorlutuna, P.; Jeong, J. H.; Kong, H.; Bashir, R. Three-Dimensional Photopatterning of Hydrogels Using Stereolithography for Long-Term Cell Encapsulation. *Lab. Chip* **2010**, *10* (16), 2062–2070.

(12) Neiman, J. A. S.; Raman, R.; Chan, V.; Rhoads, M. G.; Raredon, M. S. B.; Velazquez, J. J.; Dyer, R. L.; Bashir, R.; Hammond, P. T.; Griffith, L. G. Photopatterning of Hydrogel Scaffolds Coupled to Filter Materials Using Stereolithography for Perfused 3D Culture of Hepatocytes. *Biotechnol. Bioeng.* **2015**, *112* (4), 777–787.

(13) Raman, R.; Bhaduri, B.; Mir, M.; Shkumatov, A.; Lee, M. K.; Popescu, G.; Kong, H.; Bashir, R. High-Resolution Projection Microstereolithography for Patterning of Neovasculature. *Adv. Healthc. Mater.* **2015**, 1–10.

(14) Bartolo, P. J. Stereolithographic Processes. In *Stereolithography: Materials, Processes and Applications*; Bártolo, P. J., Ed.; Springer US: Boston, MA, 2011; pp 1–36.

(15) Stampfl, J.; Liska, R. Polymerizable Hydrogels for Rapid Prototyping: Chemistry, Photolithography, and Mechanical Properties. In *Stereolithography: Materials, Processes and Applications*; Bártolo, P. J., Ed.; Springer US: Boston, MA, 2011.

(16) Lai, M.; Clay, N. E.; Kim, D. H.; Kong, H. Bacteria-Mimicking Nanoparticle Surface Functionalization with Targeting Motifs. *Nanoscale* **2015**, *7*, 6737–6744.

(17) Jeong, J. H.; Chan, V.; Cha, C.; Zorlutuna, P.; Dyck, C.; Hsia, K. J.; Bashir, R.; Kong, H. "Living" microvascular Stamp for Patterning of Functional Neovessels; Orchestrated Control of Matrix Property and Geometry. *Adv. Mater.* **2012**, *24* (1), 58–63, 1.
(18) Annabi, N.; Tamayol, A.; Uquillas, J. A.; Akbari, M.; Bertassoni, L. E.; Cha, C.; Camci-Unal, G.; Dokmeci, M. R.; Peppas, N. A.; Khademhosseini, A. 25th Anniversary Article: Rational Design and Applications of Hydrogels in Regenerative Medicine. *Adv. Mater.* **2013**, n/a-n/a.
(19) Ritger, P. L.; Peppas, N. A. A Simple Equation for Description of Solute Release. *J. Controlled Release* **1987**, *5*, 23–36.
(20) Lin, S.; Sangaj, N.; Razafiarison, T.; Zhang, C.; Varghese, S. Influence of Physical Properties of Biomaterials on Cellular Behavior. *Pharm. Res.* **2011**, *28* (6), 1422–1430.
(21) Wattenbarger, M. R.; Bloomfield, V. A.; Bu, Z.; Russo, P. S. Tracer Diffusion of Proteins in DNA Solutions. *Macromolecules* **1992**, *25* (20), 5263–5265.
(22) Pöselt, E.; Kloust, H.; Tromsdorf, U.; Janschel, M.; Hahn, C.; Maßlo, C.; Weller, H. Relaxivity Optimization of a PEGylated Iron-Oxide-Based Negative Magnetic Resonance Contrast Agent for T_2-Weighted Spin-Echo Imaging. *ACS Nano* **2012**, *6* (2), 1619–1624.
(23) Cha, C.; Kohman, R. H.; Kong, H. Biodegradable Polymer Crosslinker: Independent Control of Stiffness, Toughness, and Hydrogel Degradation Rate. *Adv. Funct. Mater.* **2009**, *19* (19), 3056–3062.
(24) Canal, T.; Peppas, N. A. Correlation between Mesh Size and Equilibrium Degree of Swelling of Polymeric Networks. *J. Biomed. Mater. Res.* **1989**, *23* (10), 1183–1193.
(25) Chan, V.; Zorlutuna, P.; Jeong, J. H.; Kong, H.; Bashir, R. Three-Dimensional Photopatterning of Hydrogels Using Stereolithography for Long-Term Cell Encapsulation. *Lab. Chip* **2010**, *10* (16), 2062–2070.

CHAPTER 4: CHEMICAL AND MECHANICAL MODULATION OF POLYMERIC MICELLE AND VESICLE ASSEMBLY[3]

4.1 Introduction

In the past 50 years, nano-sized micelles and vesicles have been studied as carriers of various molecules for cosmetic, medical, and agricultural products.[1–4] These nanocarriers are noted for their structural stability, and can help retain the activity of multifactorial compounds.[5] Polymers can be chemically modified to tailor degradation rate and mechanism (e.g., enzymatic digestion, optical trigger) and subsequent molecular release rate.[6,7] In addition, the nanoparticle surface can be chemically or physically engineered to present a desired number and type of molecules for the targeted delivery of molecular cargos.[8,9]

[3] I would like to thank my collaborators for their microfluidic expertise and COMSOL help, most notably Joseph Whittenberg, Vivek Kumar, Jeremy Schieferstein, and Prof. Paul Kenis. I would like to thank my Kong lab collaborators, including Jinrong Chen and Prof. Jae Hyun Jeong, for their invaluable help in chemical synthesis. I would also like to thank my Soongsil collaborators, including Prof. Il Won Kim and Insil Choi. I would also like to acknowledge the School of Chemical Sciences (SCS) graphics office for their assistance with figures. Special thanks are also due to Wacek Swiech and the staff at the Frederick Seitz Materials Research Laboratory for help with transmission electron microscopy (TEM). Work was funded by the National Institutes of Health (1R01 HL109192 to H.J.K). N.C. was supported by a Dow Graduate Fellowship.

Polymeric micelles and vesicles are typically formed by the self-assembly of amphiphilic polymers during a solvent exchange process where amphiphilic polymers are first dissolved in an organic solvent and subsequently introduced into an aqueous phase.[10–12] These polymers are typically synthesized by connecting a series of water-soluble polymers such as poly(ethylene glycol),[13] hyaluronic acid,[14] poly(2-hydroxyethyl methacrylate),[15] or polypeptides[16] with hydrophobic segments to create an amphiphilic block copolymer or graft copolymer. In aqueous media, amphiphilic polymers associate to form particles in a form of micelle or vesicle, depending on the ratio of hydrophobic and hydrophilic domains in the polymer. [17,18]

Recently, microfluidic chips have been considered for various nanofabrication strategies, as these devices can mix small volumes (~nL-μL) of aqueous and organic phases at controlled rates.[19–21] Microfluidic systems have been utilized previously to produce highly monodisperse populations of liposomes,[22] quantum dots,[23] and emulsions.[24] In particular, microfluidic platforms that rapidly mix solutions via hydrodynamic flow focusing, where a central organic solvent-polymer stream is sheathed by adjacent aqueous streams, have been utilized to synthesize polymeric nanoparticles, such as nano-precipitated particles consisting of diblock copolymers.[25] Additionally, microfluidic devices possess the potential to finely control a given set of reaction or process parameters, in turn reducing batch-to-batch variability.[26]

With a bulk or microfluidic solvent exchange process, selection of an appropriate organic solvent is vital to: (1) ensure complete dissolution of the amphiphilic polymers and (2) retain functionality of molecular cargos. Meeting both requirements severely limits the types of polymers used as a building block for micelles and vesicles and also requires efforts to seek or synthesize a good solvent via trial-and-error.[27] Another potentially important factor for in solvent exchange is the balanced mixing of amphiphilic polymer, organic phase, and aqueous phase. For instance,

amphiphilic polymers with increased fraction of hydrophobic domains can rapidly precipitate during the solvent exchange process prior to nanoparticle assembly, leading to the formation of aggregates. However, to date, few efforts were made to systematically examine and resolve these potential challenges in particle assembly.

This study therefore demonstrates the significant role of amphiphilic polymer mixing conditions in regulating polymeric micelle and vesicle assembly via combined chemical modification of amphiphilic polymers and mechanical control of the solvent exchange process. We hypothesized that chemical modification of an amphiphilic polymer to thermodynamically improve its solubility in a given organic phase is advantageous to form nanoparticles with desired morphology and size. In addition, the microfluidic solvent exchange rate regulated by the volumetric flow rate ratio (termed FRR) between organic and aqueous phases would further mediate the self-assembly of amphiphilic polymers.

We examined this hypothesis by using a poly(2-hydroxyethyl)aspartamide (PHEA) polymer substituted with a controlled number of octadecyl chains (C_{18}) as a model amphiphilic polymer. The degree of substitution of C_{18} (DS_{C18}) was varied in order to create a polymeric micelle or vesicle. We modified the alkylated PHEA with a controlled number of oligovaline chains to control the solubility of the polymer in an organic solvent such as dimethylformamide (DMF). The solvent exchange rate was modulated by introducing the PHEA polymers dissolved in DMF into an aqueous phase either by dropwise addition, termed off-chip mixing, or flow focusing in a microfluidic mixer, termed microfluidic or on-chip mixing, at different volumetric flow rate ratios between DMF and water (Figure 4.1).

The critical role of oligovaline in improving polymer solubility was examined via a thermodynamic analysis. The role of oligovaline in nanoparticle formation was evaluated by

quantifying the energy of mixing via computational simulation and experimentation. The microfluidic mixing process was also examined via finite element model-based simulation and visualization of flow pattern. The morphology and average diameter of the resulting nanoparticles were evaluated with transmission electron microscopy (TEM). Overall, this study would serve to improve existing nanoparticle fabrication processes by expanding the parameter space available for self-assembly.

4.2 Results and Discussion

4.2.1 Synthesis of oligovaline-PHEA-C_{18}

First, PSI with an average molecular weight of 19,000 g/mol was prepared by acid-catalyzed polycondensation of aspartic acid.[28] Then, a controlled number of octadecyl (C_{18}) chains was conjugated to the PSI via the ring-opening nucleophilic addition of octadecylamine (Step 1 in Figure 4.2). Successful conjugation of the C_{18} chain was confirmed with the peak at 0.85 ppm on the ^{1}H NMR spectra (Figure 4.3 and 4.4). The remaining PSI rings were then substituted with ethanolamine and ethylenediamine (Steps 2 and 3 in Figure 4.2). The degree of substitution for C_{18} to polymer (DS_{C18}) was quantified with Equation 1.

$$DS_{C18} = \frac{Area\ \ from\ 0.8\ to\ 0.94\ ppm}{(Area\ from\ 4.3\ to\ 4.6\ ppm)*3} \times 100\% \quad (4.1)$$

According to the ^{1}H NMR spectrum of the PSI substituted with C_{18}, ethanolamine, and ethylenediamine (referred to as NH_2-PHEA-C_{18}), increasing the mass ratio between octadecylamine and succinimide units of the PSI from 0.28 to 0.56 led to an increase of the degree of substitution for C_{18} to polymer (DS_{C18}) from approximately 20 to 40% (Equation 4.1, Figure 4.3 and 4.4).

Separately, valine-n-carboxyanhydride (valine-NCA; structure in Figure 4.5) was prepared from the Fuchs-Farthing reaction.[29] In this reaction, L-valine underwent ring-closure in the presence of triphosgene, resulting in valine-NCA.[17] When valine-NCA reacted with the primary amines of NH_2-PHEA-C_{18}, the ring on valine-NCA was opened. This amine served as an initiator for the polymerization of the valine group, and an oligovaline chain was subsequently formed on NH_2-PHEA-C_{18} (Step 4 in Figure 4.2).[31] The presence of oligovaline chains grafted to the PHEA-C_{18} was confirmed by the distinctive ^{1}H-NMR peaks at approximately 1 ppm (Figure 4.3 and 4.4).[32] The number ratio of oligovaline chains to PHEA units was approximately 1:100 (0.01) for both DS_{C18} of 20% and 40%, as quantified by equation 4.2.

$$N_{PHEA/val} = \frac{Area\ from\ 1.01\ to\ 1.04\ ppm}{(Area\ from\ 4.3\ to\ 4.6\ ppm)*6} \quad (4.2)$$

With a quantified value for DS_{C18}, the hydrophilic mass fraction (*f*) of the PHEA polymers with DS_{C18} of 20% and 40% was approximated according to the following equation:

$$f = \frac{158(1-DS_{C18})}{158(1-DS_{C18})+366DS_{C18}} \quad (4.3)$$

Note that valine is neglected from this calculation, due to the low number ratio of valine groups to PHEA groups.[33] At DS_{C18} of 20%, the *f* of oligovaline-PHEA-C_{18} was around 0.6. When DS_{C18} was increased to 40%, *f* was lowered to about 0.4. Previous theoretical and experimental studies have indicated that an amphiphilic polymer with an *f* smaller than 0.35-0.40 self-assembles to form a polymeric vesicle.[34,35] Above this range, spherical or cylindrical micelles are typically formed. Therefore, we predicted that oligovaline-PHEA-C_{18} at DS_{C18} of 20% would form a micelle, while oligovaline-PHEA-C_{18} at DS_{C18} of 40% would form a vesicle.

4.2.2 Experimental solubility analysis of oligovaline-PHEA-C_{18} in DMF

We then evaluated the solubility of the synthesized amphiphilic PHEA molecules in DMF. Polymer solubility in the organic phase is a key consideration for solvent exchange, as the process involves the transitioning of the amphiphilic polymer from a region of high solubility to a region of low solubility. Note that other solvents, such as chloroform or hexane, were not considered because the organic solvent used for self-assembly must be miscible in water in order to enable solvent exchange.

The PHEA substituted only with C_{18} chains and amine groups, termed NH_2-PHEA-C_{18}, formed a cloudy, insoluble dispersion in DMF (Figure 4.6a-i and 4.6a-ii). The addition of the oligovaline chain to NH_2-PHEA-C_{18} dramatically improved solubility of the polymer in DMF. At both DS_{C18} of 20 and 40%, a clear yellow-brown solution was made at 30 mg/mL (Figure 4.6a-iii and 4.6a-iv). According to measurements of polymer solubility at 0 ˚ C, NH_2-PHEA-C_{18} (DS_{C18} =20 %) had a maximal solubility of only 7 mg/mL, while oligovaline-PHEA-C_{18} (DS_{C18} =20%) had a maximal solubility of around 44 mg/mL. Similar results were obtained for oligovaline-PHEA-C_{18} (DS_{C18} = 40%) and NH_2-PHEA-C_{18} (DS_{C18} = 40%) at 0 ˚C, as well as for oligovaline-PHEA-C_{18} (DS_{C18} = 20%) and NH_2-PHEA-C_{18} (DS_{C18} = 20%) at -20 ˚C and 25 ˚C.

To examine underlying mechanism by which the oligovaline group improved the solubility of the NH_2-PHEA-C_{18}, the thermodynamic properties related to solvation were quantified. Based on the mass of polymers dissolved in DMF at 0 ˚ C, the Gibbs free energy change during mixing (ΔG_{mix}) was calculated using the following equation:

$$\Delta G_{mix} = -RT \ln K_{eq} \quad (4.4)$$

Whereby R is the gas constant (8.314 J/mol-K), and T is temperature (K). K_{eq} is defined as:

$$K_{eq} = \frac{Mass\ of\ PHEA\ polymer\ in\ solution}{Insoluble\ mass\ of\ PHEA\ polymer} \quad (4.5)$$

For the temperatures considered, ΔG_{mix} for oligovaline-PHEA-C_{18} was negative, whereas ΔG_{mix} for NH_2-PHEA-C_{18} was positive (Figure 4.6b). This trend suggests that the solvation of oligovaline-PHEA-C_{18} in DMF was more thermodynamically favorable than that of NH_2-PHEA-C_{18}.

Separately, using the Flory-Huggins solution theory, the entropy of mixing (ΔS_{mix}) was calculated based on the volume fraction of the oligovaline-PHEA-C_{18} or NH_2-PHEA-C_{18} dissolved in DMF:

$$\Delta S_{mix} = -R\left(\varphi_1 \ln \varphi_1 + \frac{1}{N_2}\varphi_2 \ln \varphi_2\right) \quad (4.6)$$

whereby φ_1 is the volume fraction of DMF, φ_2 is the volume fraction of PHEA-based polymer, and N_2 is the degree of polymerization of PHEA (approximated as 190).[36] For both oligovaline-PHEA-C_{18} and NH_2-PHEA-C_{18}, the entropy of mixing is positive, suggesting a higher amount of disorder as the polymer goes into solution. At 0 ˚C, ΔS_{mix} for oligovaline-PHEA-C_{18} was approximately 5-fold larger than ΔS_{mix} for NH_2-PHEA-C_{18} (Figure 4.6b). This increase in ΔS_{mix} is likely due to the higher total fraction of PHEA polymer solubilized for oligovaline-PHEA-C_{18} than that for NH_2-PHEA-C_{18}. Then, the enthalpy of mixing (ΔH_{mix}) was approximated based on ΔG_{mix} (equation 4.4) and ΔS_{mix} (Equation 4.7):

$$\Delta H_{mix} = \Delta G_{mix} + T\Delta S_{mix} \quad (4.7)$$

According to the calculation, ΔH_{mix} for oligovaline-PHEA-C_{18} was negative (exothermic), and ΔH_{mix} was positive (endothermic) for NH_2-PHEA-C_{18} (Figure 4.6b). The change from an endothermic to an exothermic enthalpy of mixing is likely due to the change in intermolecular

interactions between PHEA polymer and DMF as the oligovaline chain is conjugated onto the polymer backbone.

4.2.3 Molecular simulation of oligovaline-PHEA-C_{18} and NH_2-PHEA-C_{18} solubility

To further examine the role of the oligovaline groups on polymer solubility, the energy of mixing per unit volume ($\Delta E_{mix}/V$) of the model PHEA polymer with 11 repeating units was computationally calculated using the following equation.[37]

$$\frac{\Delta E_{mix}}{V} = \phi_{PHEA}\left(\frac{E_{coh}}{V}\right)_{PHEA} + \phi_{SDMF}\left(\frac{E_{coh}}{V}\right)_{S} - \left(\frac{E_{coh}}{V}\right)_{PHEA-S} \quad (4.8)$$

Here, ϕ_{PHEA} and ϕ_S are volume fraction of the PHEA-based polymer and solvent (i.e., DMF or water), respectively. $\left(\frac{E_{coh}}{V}\right)_{PHEA}$, $\left(\frac{E_{coh}}{V}\right)_{PHEA}$, and $\left(\frac{E_{coh}}{V}\right)_{PHEA-S}$ are the cohesive energy density values of the pure PHEA, solvent, and the PHEA in the solvent, respectively. For all polymers including oligovaline-PHEA-C_{18} and NH_2-PHEA-C_{18}, the negative energy of mixing indicates that DMF is a better solvent than water (Table 4.1). Also, the oligovaline-PHEA-C_{18} exhibited a more negative energy of mixing, thus indicating a higher solubility in DMF. While the scope of the MD simulation was limited to a polymer with 11 repeating units for ease of computation, the computational results suggested that the oligovaline chain plays an important role in increasing the solubility of PHEA in DMF**.**

We propose that this improved solubility of the oligovaline-PHEA-C_{18} is due to favorable intermolecular association between the polymer and DMF. The amide groups of the oligovaline chains coupled to the NH_2-PHEA-C_{18} likely formed hydrogen bonds with DMF, a hydrogen bond acceptor (Figure 4.7). Thus, the oligovaline groups coupled to PHEA likely increased the number of hydrogen bonds between polymers and DMF, thus improving solubility.[38] Without this

additional hydrogen bonding, van der Waals interactions between the octadecyl chains resulted in insoluble aggregates in DMF.[39]

4.2.4 Determining mixing efficiency of the microfluidic mixer

Separately, a PDMS microfluidic mixer was prepared, with a port for an aqueous phase (marked with **A** in Figure 4.8) and a port for the DMF dissolved with amphiphilic PHEA polymers (marked with **D** in Figure 4.8). DMF and the aqueous phase were mixed at different ratios starting at the flow focusing junction (zoomed-in region depicted in Figure 4.8c). Here, the volumetric flow rate of the aqueous phase to the volumetric flow rate of the DMF phase was denoted as the flow rate ratio (FRR). The mixed solution then traveled through a straight channel followed by a curved channel with a single outlet (marked with **O** in Figure 4.8a) to collect the PHEA-DMF-water mixture. All experiments and computational on-chip studies examined FRR at 5, 10, and 20, with a constant total volumetric flow rate of 140 µL/min.

COMSOL simulations were first conducted to estimate the mixing of DMF and water in the microfluidic device. For all FRR values, the Reynold's number (eq 4.9) was kept constant at 14, thus indicating that all microfluidic mixing will be done in a laminar region. In contrast, the Reynold's number for off-chip mixing (eq 4.10) is over 3,000, suggesting a mostly turbulent mixing regime.[40] To quantify the mixing conditions on-chip, the Navier-Stokes and convective-diffusive equations were used (eq 4.11-4.13). According to the surface plots generated from the COMSOL simulation, the concentration of DMF decreased more rapidly as FRR increased (Figure 4.9a).

The simulation was also used to estimate the percent mixing, coefficients of variation, and mixing times. For ease of calculation, all values were reported for the channel beyond the dashed

orange bar in Figure 3c, which is considered the end of the flow focusing region. Percent mixing is defined as the relative amount of DMF dissolved in the water phase; for a percent mixing of 100%, all DMF added to the chip is evenly mixed with water (i.e., a homogenous solution). For FRR-20, 65% of DMF is mixed with water immediately after the flow focusing region. Conversely, for FRR-5, only 33% mixed of DMF is mixed with water. Despite these initial differences, all solutions were predicted to be well-mixed (i.e., percent mixed greater than 95%) through 5 mm after the flow focusing region (Figure 4.9b).

Coefficient of variation (COV), a parameter which represented the deviation from complete mixing, was quantified using Equation 4.14 and Equation 4.15. COV followed a similar trend from a highly unmixed state to a mixed condition (Figure 4.9c). For FRR-20, COV starts at about 1.8 which is higher than COVs for FRR-5 and FRR-10. At about 6 mm after the flow focusing region, all COV values fall below 0.2, indicating a near-complete mixing of DMF and water. The mixing time, defined as the time for 95% of DMF being mixed with water, was estimated to be around 28 ms for FRR-5. The mixing time decreased to around 13 ms at FRR-20 (Figure 4.9d).

In addition, the role of FRR on the mixing of DMF and water was experimentally examined by using DMF mixed with a colorant. As FRR increased from 5 to 10 and 20, the diameter of DMF stream in the aqueous phase became increasingly smaller, as determined with brightfield images (Figure 4.10). Notably, the initial stream diameter decreased as FRR increased. For FRR-5, the DMF stream diameter was 50 μm. At FRR-10 and FRR-20, the DMF stream diameter reduced to 36 and 29 μm, respectively.

As demonstrated from the surface plot of DMF/water generated from the COMSOL simulation (Figure 4.9a) and the brightfield microscope images of the microfluidic chip in operation (Figure 4.10a), the mixing rate of DMF with water is slowest for FRR-5. Similarly, the DMF concentration

past the flow focusing region was noticeably higher when compared to similar regions in the FRR-10 and FRR-20 conditions (Figure 4.9a).

Based on these observations, it is likely that the high DMF concentration (13% by volume when fully mixed in water) at FRR-5 potentially leads to a heterogeneous micelle population. Therefore, on-chip mixing was performed only at FRR-10 and FRR-20, whereby the final DMF concentration is 10% by volume or less in a fully-mixed condition. We anticipated that micelle self-assembly would occur under more homogenous solvent conditions if the final DMF concentration is within this range, in turn leading to a monodisperse population of micelles.

4.2.5 Polymeric micelle assembly

PHEA solutions were injected into the microfluidic chip at different FRR while keeping total volumetric flow rate constant. In particular, DMF dissolved with the oligovaline-PHEA-C_{18} with DS_{C18} of 20% was mixed with the aqueous phase at FRR of 10 and 20. Separately, the aqueous phase was introduced into the DMF-polymer solution dropwise in order to prepare micelles via off-chip precipitation. Independent of FRR and particle assembly process, oligovaline-PHEA-C_{18} formed a micelle, as confirmed with TEM images (Figure 4.11a). Interestingly, the average diameter of the micelles prepared with the microfluidic mixer ranged from 100 to 200 nm, while the average diameter of the micelles prepared with the off-chip precipitation was around 300 nm (Figure 4.11a-ii to 4.11a-iv). More interestingly, as FRR increased from 10 to 20, the micelle diameter was decreased from 200 to 100 nm (Figure 4.11b).

In contrast, a PHEA-C_{18} (DS_{C18} of 35%) solution introduced into the microfluidic chip operated at FRR-20 failed to form micelles. The mixture was simply precipitated in the water-DMF mixture, thus forming large, irregular aggregates as shown in TEM images (Figure 4.11a-iv). In addition,

solutions of oligovaline-PHEA free of C_{18} chains and solutions of NH_2-PHEA-C_{18} could not form micelles with off-chip mixing (Figure 4.12a and 4.12b), suggesting that both a high degree of hydrophobicity (from the octadecyl chains) and a high solubility in the organic solvent (from the oligovaline group) is necessary for self-assembly in a DMF/water solvent exchange.

These differences in micelle sizes can be explained by comparing the rate at which DMF and water mix with the rate at which polymer chains self-assemble to form a micelle. As confirmed with computational simulations and experimental visualization, increasing FRR decreases the mixing time of DMF and water and also the volume fraction of DMF in the DMF/water mixture. As a consequence, it is likely that the octadecyl chains of oligovaline-PHEA-C_{18} should be driven to self-associate to form the micelle core more quickly at the higher FRR, thus resulting in the micelles with a smaller diameter.[41]

4.2.6 Vesicle assembly

In addition, the microfluidic mixing and the off-chip precipitation were used to prepare a polymeric vesicle. In this study, oligovaline-PHEA-C_{18} with DS_{C18} of 40% was used. With the off-chip precipitation, the polymers formed a hollow vesicle with an average diameter of around 100 nm (Figure 4.13). In the resulting TEM images, a dark bilayer with a thickness of around 20 nm is clearly denoted. However, polymeric vesicles could not be formed with the microfluidic mixing. When mixing DMF with oligovaline-PHEA-C_{18} in the microfluidic mixer, a brown precipitate was formed rapidly near the flow focusing region (Figure 4.14). At both FRR-10 and FRR-20, small, irregular nanoparticles without a noticeable bilayer and a diameter from 20 to 40 nm were found in TEM images (Figure 4.13b and 4.13c). Similar results were demonstrated even when the oligovaline-PHEA-C_{18} concentration in DMF was lowered from 30 mg/mL to 15 mg/mL. In

addition, a NH_2-PHEA-C_{18} (DS_{C18}=40%) solution mixed with water via off-chip mixing and a NH_2-PHEA-C_{18} solution mixed with water at FRR-20 failed to form stable particles (Figure 4.12c and Figure 4.13d).

We propose that increasing DS_{C18} of the oligovaline-PHEA-C_{18} from 20 to 40% significantly elevated the hydrophobicity of the polymer. In turn, the polymers dissolved in DMF may rapidly precipitate upon contacting with the water phase, as observed with brown-colored precipitates at the point of mixing (Figure 4.14). With a higher degree of hydrophobicity, the diffusion coefficient of oligovaline-PHEA-C_{18} with DS_{C18} of 40% in a DMF-water mixture is likely lower than that of oligovaline-PHEA-C_{18} with DS_{C18} of 20%, in turn leading to the rapid precipitation of polymer in the flow focusing region as well as the downstream channel.[42,43] However, the off-chip mixing takes place under turbulent flow whereby convection dominates polymer transport, thus driving polymers to self-assemble into a vesicle. This interesting result is different from previous studies which have demonstrated that nano-sized liposomes could be formed in a 2D microfluidic flow focusing device, likely due to different molecular size and subsequent diffusivity of the lipids used.[44]

4.3 Conclusion

In conclusion, the solubility of the amphiphilic polymers in an organic phase and the laminar flow-based microfluidic mixing process contribute to regulating size of polymeric micelles in an orchestrated manner. The oligovaline groups conjugated to the NH_2-PHEA-C_{18} contributed to thermodynamically improving the solubility of the polymer in DMF, likely due to increased hydrogen bonds between polymer and DMF. Moreover, the microfluidic mixer enabled us to mix laminar streams of DMF and water at controlled rates. Subsequently, increasing the mixing rate in

the microfluidic mixer decreased the size of micelles formed by the oligovaline-PHEA-C_{18} with DS_{C18} of 20%. In contrast, the microfluidic mixing failed to form a vesicle constituted with the oligovaline-PHEA-C_{18} (DS_{C18} of 40%). This result was attributed to the imbalanced diffusion of DMF and polymer into the water phase in the laminar flow mixing. To the best of our knowledge, this study is one of the first attempts to regulate nanoparticle fabrication by orchestrating solubility of particle-forming polymers and microfluidic mixing. We also propose that this study presents a unique approach, whereby polymer solubility and mixing conditions are independently controlled. We envision that the orthogonal approach demonstrated in this study will be broadly useful to understanding and further improving the quality of nanoparticles formed from a wide array of amphiphilic polymers of interest.

4.4 Materials and Methods

All chemicals were purchased from Sigma-Aldrich and used without purification, unless otherwise noted. Unless noted, all water was high-pressure liquid chromatography (HPLC) grade water (Macron).

4.4.1 Synthesis of polysuccinimide (PSI)

First, 50 g of L-aspartic acid was dissolved in 160 g of warm sulfolane under vigorous stirring. The temperature was gradually brought to 170 ° C under nitrogen. Then, 1.1 mL of 85% phosphoric acid (Fisher) was added to the reaction mixture as a catalyst. A glass outlet was added to the reaction flask to remove excess water from the reaction. After reaction for about 7 hours, the reaction mixture was cooled to room temperature. The reaction mixture was then precipitated with 200 mL of methanol (EMD), and then several times with 200 mL of DI water. The excess

water from each washing step was tested with a pH strip (Hydrion). Here, a neutral pH reading confirmed removal of any impurities. Afterwards, the precipitate was loaded into a dialysis bag, and then dialyzed against DI water (MWCO 12,000-14,000, Fisherbrand). The dialysis water was changed approximately every 12 hours. Afterwards, the precipitate was removed from the dialysis bag, frozen at -20 ° C, and then lyophilized to form a dry powder (Labconco Freezone 6).

4.4.2 Synthesis of NH_2-PHEA-C_{18}

First, 291 mg of PSI was dissolved in DMF (ACS grade) at a concentration of 20-25 mg/mL. Then, 81 or 162 mg of octadecylamine was added to reaction mixture to form PHEA-C_{18} with a degree of substitution of octadecyl chains (DS_{C18}) of 20% or40%, respectively. After reaction for at least 12 hours under nitrogen at 70 ° C, the reaction mixture was cooled to room temperature. Then, 161 µL (for DS_{C18} of 20%) of ethanolamine and 136 µL (for DS_{C18} of 40 %) of ethanolamine were added dropwise and then reacted for another 24 h. Afterward, a dilute solution of excess ethylenediamine was prepared in dry DMF. Then, the reaction mixture was slowly added to the ethylenediamine solution over several minutes. For this step of the reaction, the molar ratio of ethylenediamine to unreacted PSI rings was at least 5:1. After reacting for 3 hours at room temperature, the reaction mixture was dialyzed for at least 2 days against DI water (MWCO 12,000-14,000, Fisherbrand), frozen, and then lyophilized to form a dry powder (Labconco).

4.4.3 Synthesis of valine-N-carboxyanhydride (valine-NCA)

First, 1.2 g of L-valine was dissolved in 12 mL of tetrahydrofuran (THF). Separately, 1.2 g of triphosgene was added to 2 mL of THF, and then added to the L-valine solution dropwise. The reaction mixture was then kept at 40 ºC for 3 hours under nitrogen. Afterwards, the reaction

mixture was cooled and then vacuum-filtered to remove any insoluble material. The filtrate was then added to 300 mL of hexane, and then crystallized at -20 ^{o}C.

4.4.4 Synthesis of oligovaline-PHEA-C_{18}

First, 165 mg of NH_2-PHEA-C_{18} with DS_{C18} of 20% and 200 mg of NH_2-PHEA-C_{18} with DS_{C18} of 40% were separately dissolved in 3 mL DMF, and then slowly heated to 60 ˚ C. In parallel, 29 mg and 72 mg of valine-N-carboxyanhydride (valine-NCA) were dissolved in 1 mL of DMF. These solutions were then added dropwise to the mixture of NH_2-PHEA-C_{18} with DS_{C18} of 20% and 40%, respectively. After reacting at 60 ˚ C for at least 24 h under nitrogen, the reaction mixture was dialyzed (MWCO 3,500, Fisherbrand) against DI water for at least 2 days, while changing water at least three times. The sample was then frozen and lyophilized to form a dry powder (Labconco).

4.4.5 NMR analysis of oligovaline-PHEA-C_{18}

Oligovaline-PHEA-C_{18} was dissolved in DMSO-d6 (Cambridge Isotope Laboratory) at a concentration of at least 10 mg/mL, and then loaded into an NMR terialsube (Varian VXR 500). To improve the height of the analyte peaks, solvent saturation was used as needed. All scans were done at 35 ˚ C, and at least 20 scans were taken per sample. All spectra were processed with ACDLABS 12.0 software.

4.4.6 Molecule dynamics simulation of PHEA solubility

Molecular dynamics (MD) simulations were employed to study the effect of the oligovaline chains on the solubility of NH_2-PHEA-C_{18} and oligovaline-PHEA-C_{18}. All computational

calculations were performed using Materials Studio simulation software (version 8.0) from BIOVIA equipped with COMPASS II force field.[45] Coulomb interactions were calculated using Ewald summation, and van der Waals interactions were determined using an atom-based summation method (15.5 Å cutoff distance).

Two model polymers with 11 units were examined, with side chain compositions of (i) hydroxyethyl:C_{18}:aminoethyl = 8:2:1 (for NH_2-PHEA-C_{18}), and (ii) hydroxyethyl:C_{18}:oligovaline = 8:2:1 (for oligovaline-PHEA-C_{18}) (Figure 4.15). The cohesive energy densities of pure polymers, solvents (DMF or water), and polymers in solvents were obtained through the MD simulation to ultimately calculate the energy of mixing per unit volume. A polymer concentration of 30vol% was selected. Each model polymer was first optimized using Forcite module, and the optimized structure was packed into a lattice typically ca. $(50\ Å)^3$ (density 1 g/cm^3) using the Amorphous Cell module. Once the lattice was energetically minimized, MD method was implemented for 100 ps with 1 fs time step. The NVT ensemble (Nosé thermostat) was used at 298 K (Q ratio: 0.01).[46] The initial 50 ps was for equilibration, and the later 50 ps was for data sampling at 10 ps interval. MD calculations were similarly performed for pure solvents and polymers with 11 units (30vol%) in solvents. Each case was simulated at least three times starting from independent initial structures, and the lowest energy result was chosen for the sampling of five structures. The reported values of cohesive energy density and the energy of mixing per unit volume were the average from five sampled structures.

4.4.7 Synthesis of oligovaline-PHEA-C_{18} and PHEA-C_{18}-NH_2 labeled with fluorescein isothiocyanate (FITC)

Briefly, oligovaline-PHEA-C_{18} and PHEA-C_{18}-NH_2 were dissolved in DMF. Then, a solution of fluorescein isothiocyanate (FITC) was added dropwise to the polymer solution. The mass ratio of PHEA polymer to FITC was kept at approximately 1:0.0006. The reaction continued for 24 h at room temperature (for oligovaline-PHEA-C_{18}) or 24 h at 60 ˚C (for PHEA-C_{18}-NH_2). Afterward, the reaction mixtures were dialyzed (MWCO 3,500, Fisherbrand) against DI water for 48 hours; fresh DI water was added at least twice.

4.4.8 Determination of maximal solubility of PHEA

Oligovaline-PHEA-C_{18} and NH_2-PHEA-C_{18} labeled with FITC were dissolved in DMF at varying concentrations ranging from 0 to 250 µg/mL. Then, a linear calibration curve was established for each polymer functionalized with FITC by measuring polymer concentration versus the fluorescence intensity at 485 nm (Tecan Infinite 200 PRO plate reader; gain set to 50). To determine the maximal solubility of oligovaline-PHEA-C_{18} and NH_2-PHEA-C_{18}, a mass of polymer (5-15 mg) was placed in a clean glass scintillation vial, and then dissolved at a given concentration (50 mg/mL for oligovaline-PHEA-C_{18}, or 15 mg/mL for NH_2-PHEA-C_{18}). Then, the vial was mechanically agitated briefly, then incubated for 1 h at -20, 0, or 25 ˚C. After incubation, the polymer solution was separated from the insoluble polymer with centrifugation (two minutes at 10,000 rcf; Eppendorf centrifuge 5424). The mass of insoluble polymer was then dissolved in a large volume of DMF overnight at room temperature in the dark, and the fluorescent intensity of the resulting solution was then taken at 485 nm. The concentration of soluble and insoluble polymer was then back-calculated using the established calibration curve and a mass balance equation.

4.4.9 Mold fabrication for microfluidic devices

Molds for replicating polydimethylsiloxane (PDMS) microfluidic devices were fabricated using standard photolithography procedures. Three-inch silicon wafers (University Wafer) were cleaned by rinsing with acetone then isopropanol and dried by blowing nitrogen over the wafers. Cleaned silicon wafers were then heated on a hot plate at 115 °C for 3 min and cooled by blowing nitrogen over the wafers. SU-8 2050 photoresist (MicroChem Corp.) was spin-coated onto the wafers to a final thickness of roughly 100 μm. The SU-8 coated silicon wafers were baked on hot plates for 5 min at 65 °C, then 17 min at 95 °C, and finally 2 min at 65 °C. Wafers were then placed inside a UV exposure system (OAI). A transparency mask, made using Adobe Illustrator CS5 (Adobe Systems Incorporated,) and printed by Fineline Imaging (Fineline Imaging), was placed on top of the SU-8. A PL-360LP filter (Omega Optical, Inc.) was placed on top of the transparency to reduce air gaps between the mask and SU-8, and reduce T-topping from short wavelength (<350 nm) light. The wafers were then exposed to UV light (5.44 mW/cm^2) for 47 seconds. The UV exposed SU-8 wafers were placed on a hot plate and the temperature was ramped from room temperature to 55 °C at 2 °C/min. Wafers were then baked for 2 h at 55 °C, allowed to cool to room temperature, and then developed by gently swirling in propylene glycol monomethyl ether acetate (PGMEA) for about 10 min. Developed wafers were rinsed with PGMEA, then isopropanol, and dried by blowing nitrogen over the wafers. Wafers were then coated with perfluorodecyl-1H,1H,2H,2H-trichlorosilane (Gelest) via vapor deposition to prevent adhesion of PDMS to the mold.

4.4.10 Nanoparticle-extruding microfluidic device fabrication

PDMS replicates were made by mixing RTV615 (Momentive Performance Materials,) or Sylgard 184 (Dow Corning) base and curing agent at a 10:1 ratio. The mixture was degassed in a

vacuum desiccator for ~20 minutes, poured on a mold inside a petri dish, and placed in an oven at 65 °C for 2 hours to cure the PDMS. The PDMS was peeled off the mold and holes were punched at the inlets and outlet using 19 gauge hypodermic tubing with a beveled end. A glass slide (Thermo Fisher Scientific Inc.) was cleaned with the Alconox solution, rinsed with water (18.0 MΩ cm), and dried with nitrogen. Oxygen plasma was used to activate the PDMS and glass slide surfaces to ensure stable bonds between PDMS and glass. Then, the PDMS replicate was pressed against the glass slide and incubated in an oven at 65 °C overnight.

4.4.11 COMSOL simulation to characterize on-chip mixing

Reynolds number was calculated using the following formula:

$$\mathrm{Re} = \frac{vl}{\nu} \tag{4.9}$$

where v, l, and υ are total linear flow velocity, characteristic length scale, and kinematic viscosity in the outlet channel, respectively. Reynolds number for the off-chip mixing was calculated using the equation for a stirred tank[47]:

$$\mathrm{Re} = \frac{\rho N D^2}{\mu} \tag{4.10}$$

Whereby ρ is the density of DMF (0.9446 g/mL), μ is the viscosity of DMF (0.846 mPa-s), N is the rotational speed (1,000 rpm), and D is the diameter of the agitator (12.7 mm).

"Single-phase laminar flow" and "transport of diluted species" modules were coupled in COMSOL in order to solve Naviér-Stokes (N-S) equation and convective-diffusion, respectively for incompressible fluid. The governing equations are as follows:

Naviér-Stokes equation:

$$\rho(v.\nabla)v - \nabla.\eta(\nabla v + (\nabla v)^T) + \nabla p = 0 \tag{4.11}$$

$$\nabla . v = 0 \quad (4.12)$$

Convective-Diffusion equation:

$$\mathcal{D}\nabla^2 c - v . \nabla c = 0 \quad (4.13)$$

In the above equations, ρ denotes density (kg/m^3), v is the velocity vector (m/s), η denotes viscosity (Pa s), p equals pressure (Pa), $\mathcal{D}$ denotes the diffusion coefficient (m^2/s) and c represents the concentration (mol/m^3). The following fluid properties were used in the simulation; water – density: 1,000 kg/m^3, dynamic viscosity: 0.89 mPa-s, concentration: 55,400 mol/m^3; DMF – density 9,446 kg/m3, dynamic viscosity: 0.864 mPa-s, concentration: 12,900 mol/m^3. The diffusion coefficient was kept as 10^{-9} m^2/s for both water and DMF, which is in agreement with the common values found in literature.[48]

Simulations were performed for three different water/DMF flow rate ratios (FRRs) – 5:1, 10:1, 20:1 – while the total volumetric flow rate was kept constant. Maximum triangular mesh element size was fixed at 0.03 mm for all the simulations. Also, mesh for all the simulations were calibrated for fluid dynamics physics. The total number of mesh-elements was constant across all the simulations with 16,444 elements, 94 vertex elements, and 2,265 boundary elements.

The concept of covariance (CoV) was used in order to estimate the level of mixing. CoV, in layman terms, indicates the extent of variation of a quantifiable entity (concentration in this case) in an ensemble. Therefore, a lower CoV represents lower ensemble variation and consequently, high uniformity. Essentially, a lower CoV represents a higher level of "mixedness" and vice versa in this case. Furthermore, we considered 95% mixing as the state of complete mixing.[48] CoV was calculated at different positions in the outlet channel (past the flow focusing region) for various flow rate ratios to account for differences in the extent of mixing. The mixing times were estimated by calculating the time required to reach 95 % mixing for each different FRR.

$$\frac{\sqrt{\frac{\int_0^{0.2}(c-\bar{c})^2.dl}{0.2}}}{\bar{c}} \tag{4.14}$$

In the above equation, c denotes the concentration of DMF in the outlet channel where the CoV is evaluated and $\bar{c}$ denotes the concentration of DMF in a fully mixed state that is calculated using the following formula:

$$\bar{c} = \frac{v_D * c_D}{v_w + v_D} \tag{4.15}$$

In the above equation, v_D and v_w are the linear velocities of DMF and water in the outlet channel, respectively. c_D is the concentration of DMF at the inlet (12,900 mol/m^3).

4.4.12 Preparation of PHEA nanoparticles using the microfluidic mixer

Oligovaline-PHEA-C_{18} (DS_{C18} of 20% and 40%) was dissolved in DMF at a concentration of 30 mg/mL. A 1 mL glass syringe containing 300 µL of the PHEA polymer solution was loaded onto a microliter syringe pump (Harvard Apparatus). Separately, a syringe charged with 10 mL of phosphate buffered saline (PBS, Corning Cellgro) was loaded onto a milliliter syringe pump (Harvard Apparatus). For both solutions, care was taken to remove air bubbles. Prior to use, microfluidic chips were flushed with isopropanol and then PBS at a flow rate of 30 µL/min to remove any air pockets. Then, PBS and oligovaline-PHEA-C_{18} in DMF were pumped through the chip at the following flow rates: 117 µL of PBS/min: 23 µL of DMF solution/min (FRR-5); 127µL of PBS /min:12.7 µL of DMF solution/min (FRR-10); 133 µL of PBS /min:7 µL of DMF solution /min (FRR-20). The outlet from the tube was collected in a centrifuge tube. Afterwards, the nanoparticles were washed twice in a 0.5 mL centrifugal filter (100,000 MWCO; Amicon Millipore) at 1,500 rcf for at least 10 minutes (Eppendorf centrifuge 5424), and each time re-dispersed in water. In order to visualize the mixing conditions on-chip, the experiments described

above were repeated, but with DMF containing orange-red food coloring (McCormick). All images were captured with a light microscope (Leica M205 C). For control on-chip mixing experiments, additional control PHEA polymers with DS_{C18} of 15% and 35% and no amine groups were prepared and then mixed at FRR-20.

4.4.13 Off-chip preparation of PHEA nanoparticles

Separately, 100 µL of oligovaline-PHEA-C_{18} solution was added into a 7 mL scintillation glass vial, and then stirred with a magnetic stir bar (12.7 mm diameter) at 1,000 rpm on a hot plate. Then, 1 mL of PBS was added in a drop-wise fashion to the PHEA solution over the course of approximately 15 to 30 seconds. The resulting particles were washed identically to the particles prepared on the microfluidic mixer. For a control off-chip mixing experiment, an oligovaline PHEA polymer was prepared with no octadecyl chains and then mixed off-chip.

4.4.14 TEM imaging of PHEA nanoparticles

PHEA nanoparticles were suspended in water at 0.75-1.5 mg/mL. Separately, a 20 mg/mL solution of phosphotungstic acid (PTA) was prepared and the pH was adjusted to a neutral range (6-8) with concentrated NaOH. Then, the PTA solution and the particle dispersions were mixed in a 1:1 volumetric ratio. Approximately 10 µL of this solution was quickly added to a 200 mesh carbon TEM grid (EMS) on top of a filter paper, and then dried in air for about 20 minutes before imaging. Images were captured (JEOL 2100) at 200 kV, with multiple images taken on at least three different sections of each grid.

4.4.15 Image analysis of oligovaline-PHEA-C_{18} nanoparticles

All images were analyzed in ImageJ (NIH). Approximately 15 nanoparticles were analyzed per condition. To analyze the diameter of the PHEA-C_{18}-valine, a straight line was drawn across the micelle image and then measured. To analyze the diameter and thickness of the PHEA-C_{18}-valine polymersomes, a region-of-interest (ROI) was defined separately for the outer and inner diameter of the polymersome. Then, Feret's diameter was measured. The diameter of the polymersome was defined as the geometric mean of the Feret and MinFeret values of the outer oval. To quantify polymersome thickness, geometric mean of the Feret and MinFeret values were measured for the inner and outer ROIs, and then subtracted.

4.4.16 Statistical analysis of data

Statistical significance between all conditions was compared using a one-way ANOVA test with a post-hoc Tukey's test (R Studio 3.2.2).

4.5 Figures and Tables

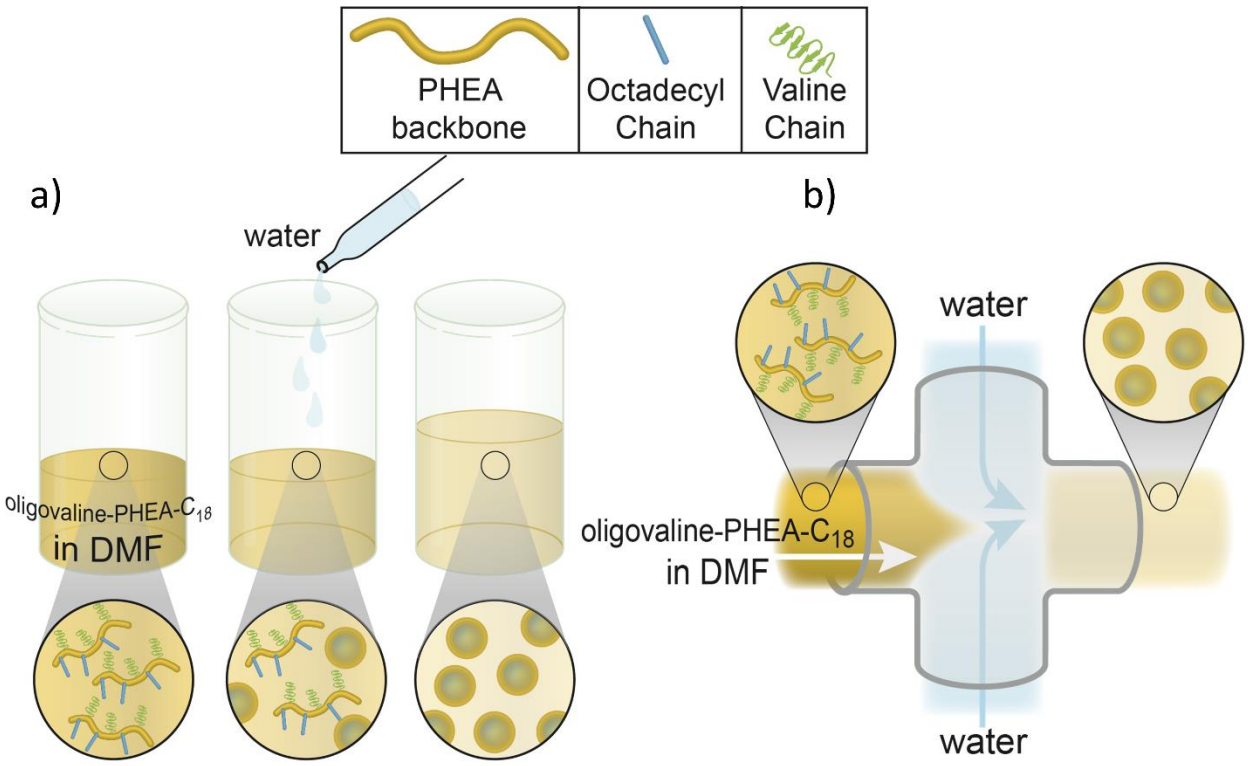

Figure 4.1 Schematic depicting off-chip (a) and microfluidic/on-chip mixing (b) to prepare PHEA nanoparticles.

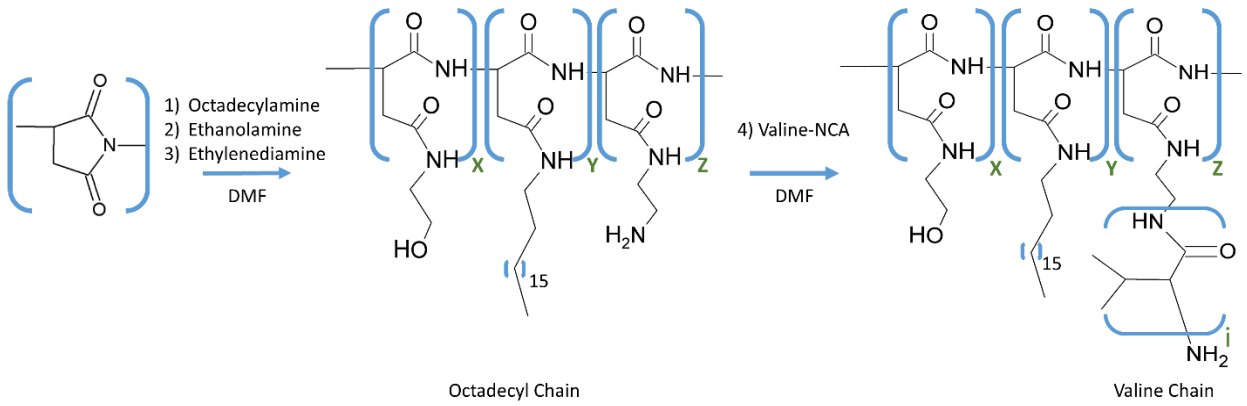

Figure 4.2 Schematic depicting the synthesis of polyaspartamide substituted with octadecyl and oligovaline groups (termed "Oligovaline-PHEA-C_{18}"). The molar ratio of x, y, and z monomers is determined by changing the ratio of ethanolamine, octadecylamine, and ethylenediamine added in Step 1 to 3. Note that the distribution of x, y, and z in the polymer chain is random.

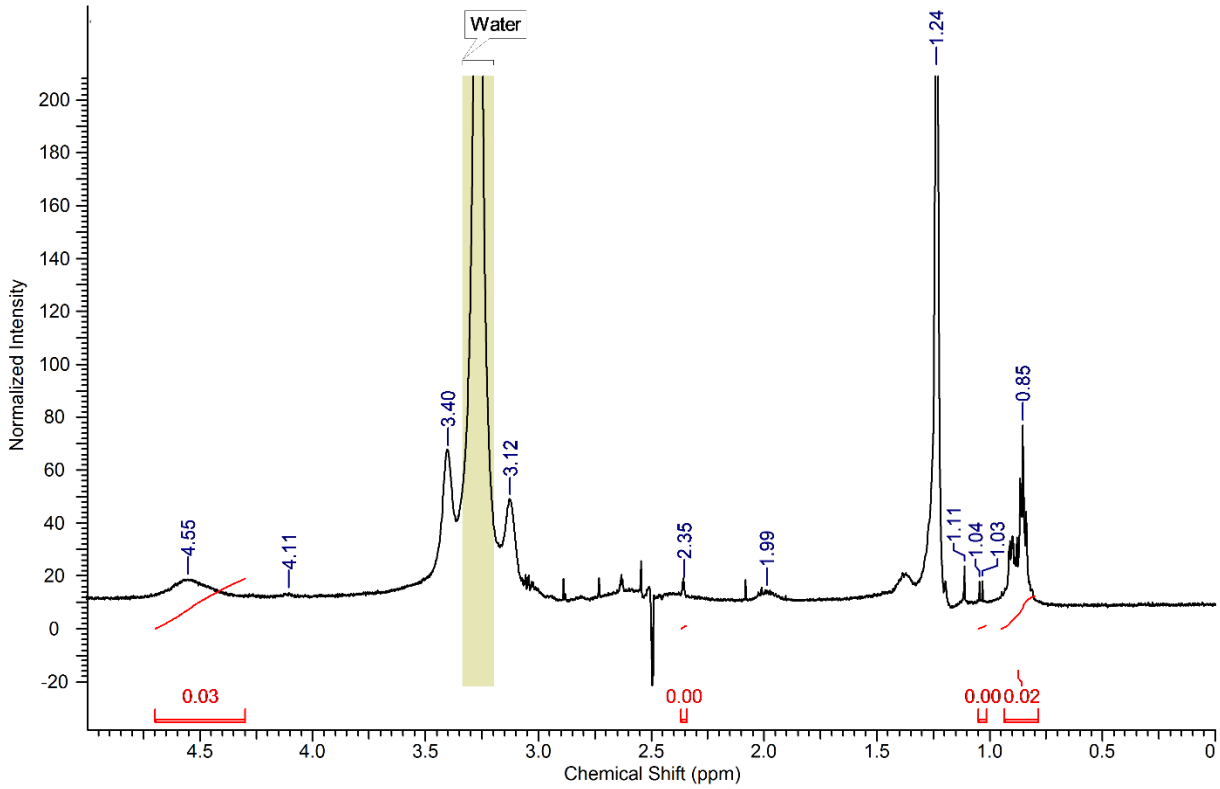

Figure 4.3 ^{1}H-NMR spectrum for oligovaline-PHEA-C_{18} (DS_{C18} = 20 %). Peaks are denoted for the PHEA backbone (4.5 ppm), the octadecyl chain (0.85 ppm), and valine (1.02 and 1.12 ppm). Note that the tan shaded area denotes the presence of water.

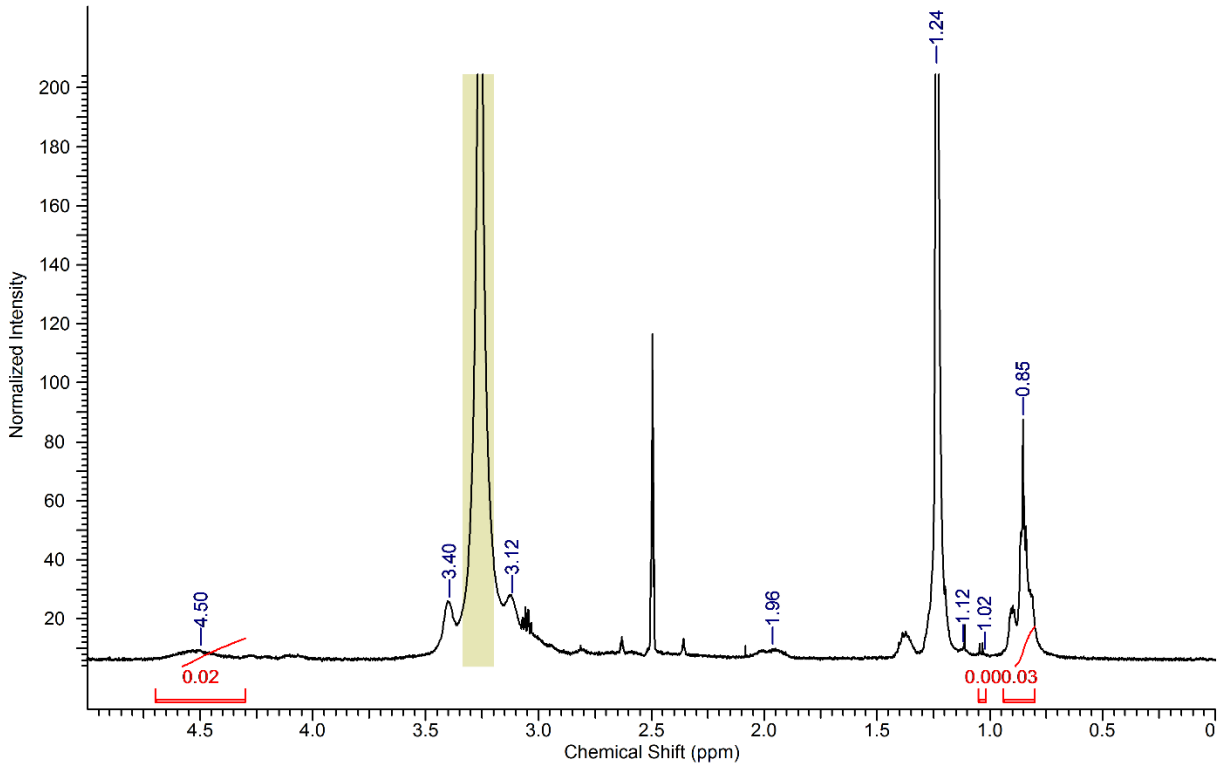

Figure 4.4 ^{1}H-NMR spectrum for oligovaline-PHEA-C_{18} (DS_{C18} = 40 %). Peaks are denoted for the PHEA backbone (4.5 ppm), the octadecyl chain (0.85 ppm), and valine (1.02 and 1.12 ppm). Note that the tan shaded area denotes the presence of water.

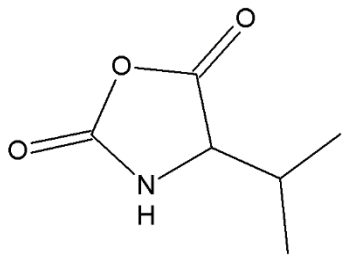

Figure 4.5 Structure of valine n-carboxyanhydride (valine-NCA) used to prepare valine chains. Structure confirmed with ^{1}H-NMR (data not shown).

a)

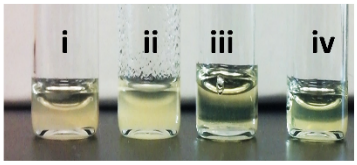

b)

	ΔG_{mix} (J/mol)	ΔS_{mix} (J/mol-K)	ΔH_{mix} (J/mol)
Oligovaline-PHEA-C_{18}	-4380	0.94	-4130
NH_2-PHEA-C_{18}	378	0.23	316

Figure 4.6 Effects of oligovaline on the solubility of PHEA in DMF. (a) Images of PHEA dissolved in DMF at 30 mg/mL. (i) NH_2-PHEA-C_{18} (DS_{C18} = 20%); (ii) NH_2-PHEA-C_{18} (DS_{C18} = 40%); (iii) Oligovaline-PHEA-C_{18} (DS_{C18} = 20%); (iv) Oligovaline-PHEA-C_{18} (DS_{C18}= 40%). (b) Changes in Gibbs free energy of mixing (ΔG_{mix}), the heat of mixing (ΔH_{mix}), and the entropy of mixing (ΔS_{mix}) for oligovaline-PHEA-C_{18} (DS_{C18}= 20%) and NH_2-PHEA-C_{18} (DS_{C18}= 20%). All values were calculated at 0 ˚C.

Polymer with 11 units	Solvent	$\left(\frac{E_{coh}}{V}\right)_{PHEA}$ (J/cm³)	$\left(\frac{E_{coh}}{V}\right)_{S}$ (J/cm³)	$\left(\frac{E_{coh}}{V}\right)_{PHEA-S}$ (J/cm³)	$\left(\frac{\Delta E_{mix}}{V}\right)$ (J/cm³)
OH:CH_3:Valine = 8:2:1	DMF	350.2	655.7	572.9	-8.8 ± 2.6
	Water	350.2	2281.4	1698.0	4.0 ± 4.7
OH:CH_3:NH_2 = 8:2:1	DMF	436.5	655.7	595.1	-5.1 ± 3.4
	Water	436.5	2281.4	1709.4	18.5 ± 7.7

Table 4.1 The computationally simulated energy of mixing per unit volume for the oligovaline-PHEA-C_{18} and the NH_2-PHEA-C_{18} with 11 units dissolved in DMF or water at 30vol%. The unit for the energy per volume is J/cm^3.

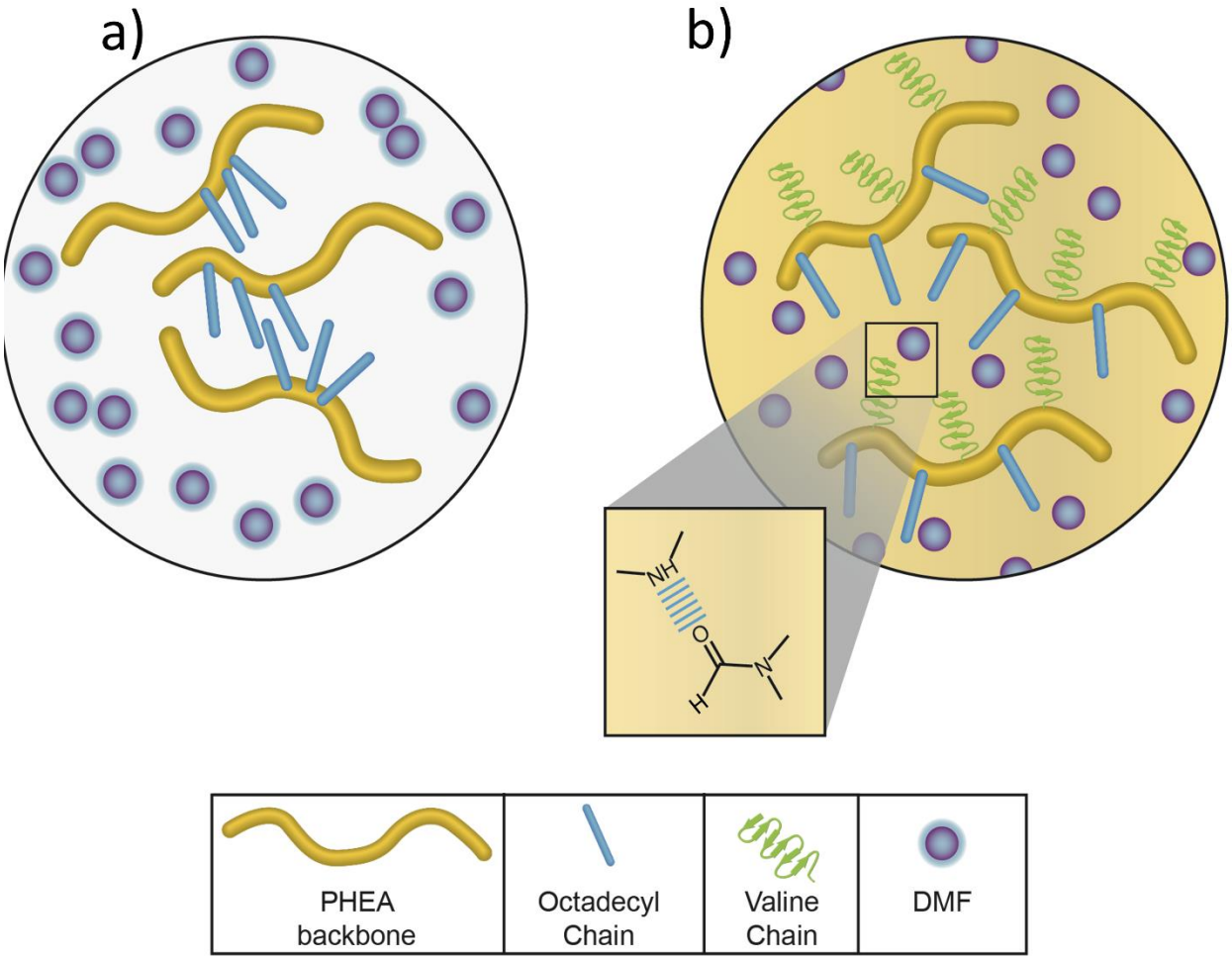

Figure 4.7 Proposed mechanism for the solubility changes that occur with the conjugation of the oligovaline chains to NH_2-PHEA-C_{18}. Without the oligovaline chains, the PHEA polymer associates with itself in insoluble aggregates (a). By conjugating oligovaline chains to NH_2-PHEA-C_{18}, additional sites for hydrogen bonding with DMF are present in the polymer (b), thus enabling improved solubility in DMF. The dashed blue line (as depicted in inset) indicates the presence of hydrogen bonding between secondary amines on the valine chain and DMF.

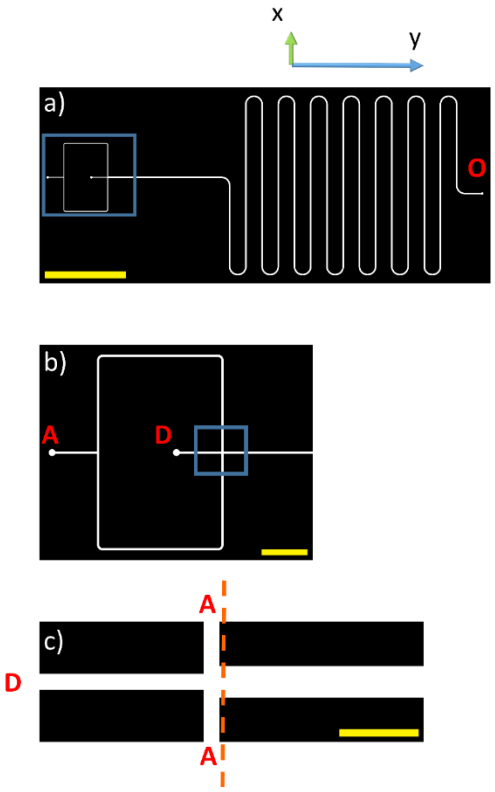

Figure 4.8 CAD image depicting microfluidic mixer design. (a) CAD image of the entire chip design. “O” corresponds to the outlet for the mixed DMF/water streams. A region of interest (depicted in b) is denoted with a blue line. Yellow scale bar corresponds to 1 cm. (b) Zoomed-in image of the inlets of the chip. “D” corresponds to the inlet stream for DMF dissolved with polymer, and “A” corresponds to the inlet stream for the aqueous media. A region of interest (termed flow focusing region; depicted in c) is denoted with a blue line. Yellow scale bar corresponds to 2 mm. (c) Zoomed-in image of the flow focusing region. The dashed orange line corresponds to the starting point for the area considered for calculating the coefficient of variance and percent mixing in the COMSOL simulation. Yellow scale bar corresponds to 0.5 mm. For all images, the coordinates for the chip are defined as “x” (green arrow) and “y” (blue arrow).

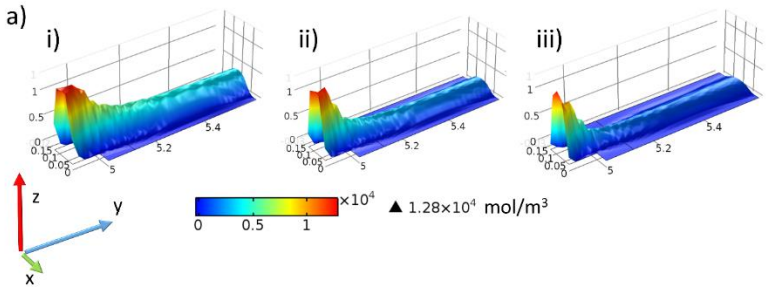

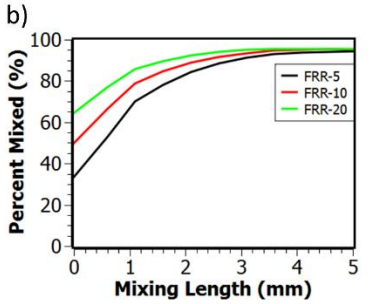

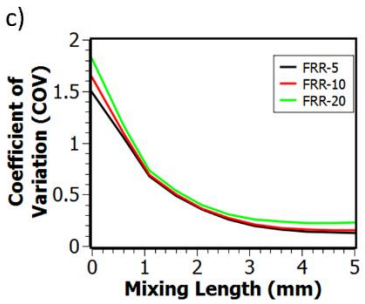

d)

	Mixing Time (ms)	Reynold's Number
FRR-5	28.3	14
FRR-10	17.6	14
FRR-20	13.3	14

Figure 4.9. Quantifying mixing conditions in the microfluidic mixer via COMSOL simulations. (a) Surface plots depicting changes in DMF concentration with respect to x-y (green-blue arrows) in the microfluidic mixer for FRR-5 (i), FRR-10 (ii), and FRR-20 (iii). DMF concentration ranges from 0 (blue in color in the surface plot) to 1.28×10^4 mol/m^3 (red in color in the surface plot). The z-axis corresponds to DMF concentration as well. (b) Percent mixed versus mixing length (y) for FRR-5, FRR-10, and FRR-20. (c) Coefficient of variation (COV) versus mixing length (y) for FRR-5, FRR-10, and FRR-20. Note that these plots only consider the region after the initial flow focusing zone (i.e., only the channel length after the dotted orange line in Figure 3c/Figure 5a is considered). (d) Mixing time and Reynold's number values for FRR-5, FRR-10, and FRR-20.

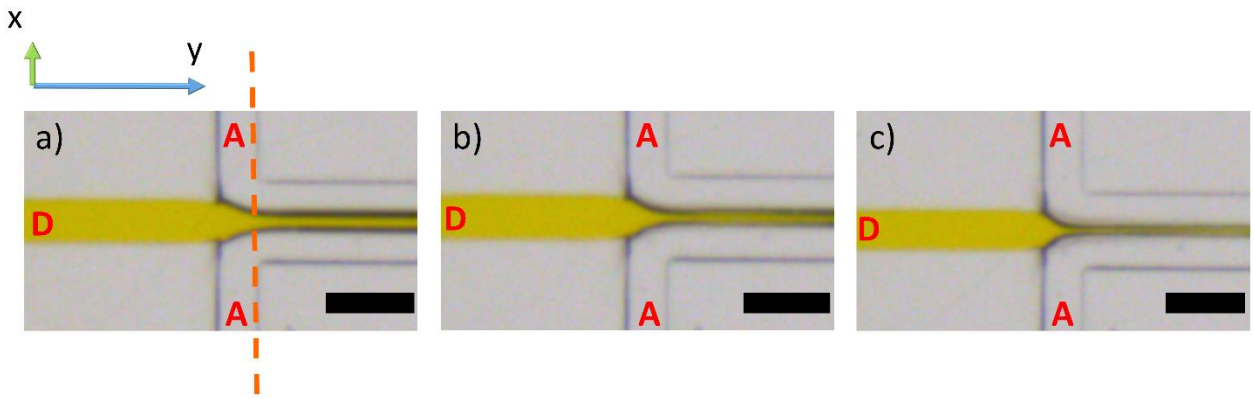

Figure 4.10 Brightfield microscopy images of the microfluidic chip in operation. An orange food colorant is used to distinguish the DMF stream (labeled "D") from the aqueous stream (labeled "A"). The flow rate ratio (FRR) varies from 5 (a) to 10 (b) and 20 (c). The black scale bar corresponds to 200 µm. The green and blue arrows correspond to the x- and y-axis, respectively. The dashed orange line corresponds to the starting point of the area considered for calculating the COV and percent mixing in the COMSOL simulation.

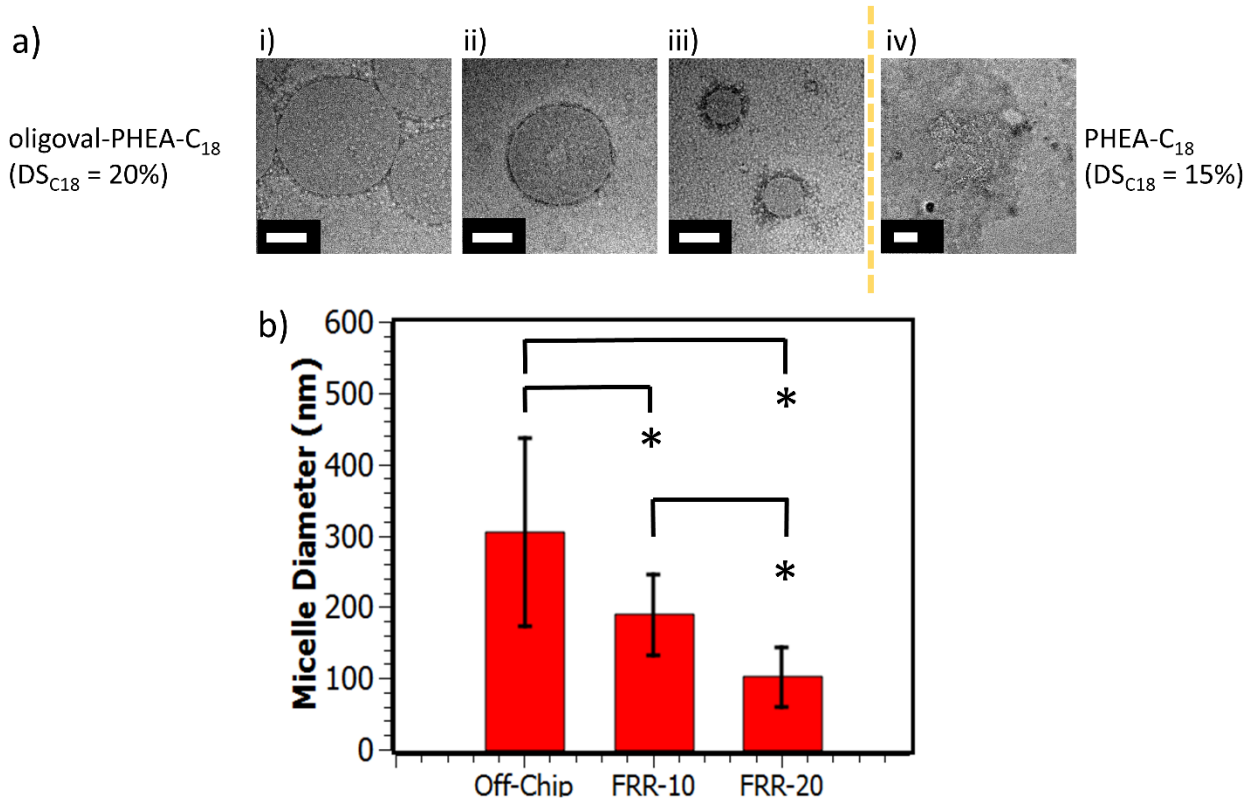

Figure 4.11 TEM images and size analysis for PHEA micelles. (a) Oligovaline-PHEA-C_{18} (DS_{C18}=20%) micelles formed with off-chip mixing (i), with microfluidic mixer at FRR-10 (ii) and with microfluidic mixer at FRR-20 (iii). Micelles were not formed with a separate polymer (PHEA-C_{18} with DS_{C18} of 15%) at FRR-20 (iv). The scale bar represents 100 nm. (b) Diameter of oligovaline-PHEA-C_{18} (DS_{C18} = 20%) micelles quantified with TEM images. At least 15 particles were analyzed per condition. * represents the statistical significance of the difference between conditions (*$p < 0.05$). Values and bars correspond to averages and standard deviation of one set of measurements, respectively.

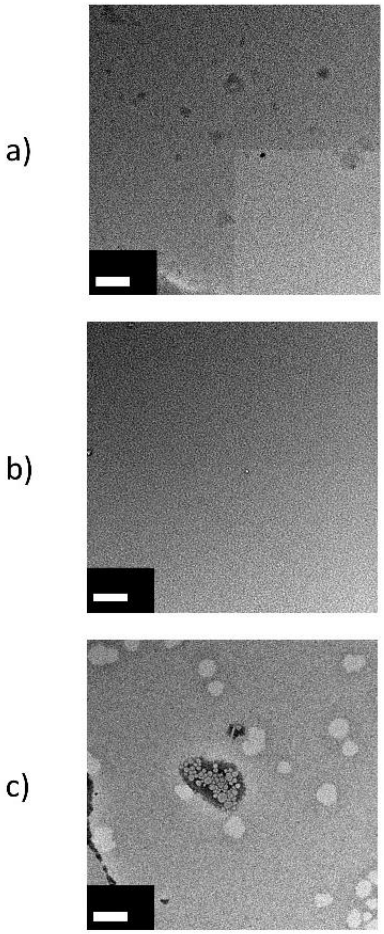

Figure 4.12 Transmission electron microscopy (TEM) images of polyaspartamide nanoparticles created as additional controls. Particles were fabricated via off-chip precipitation using oligovaline-PHEA (a), NH_2-PHEA-C_{18} (DS_{C18} = 20 %) (b), or NH_2-PHEA-C_{18} (DS_{C18} = 40 %) (c). Scale bar denotes 100 nm.

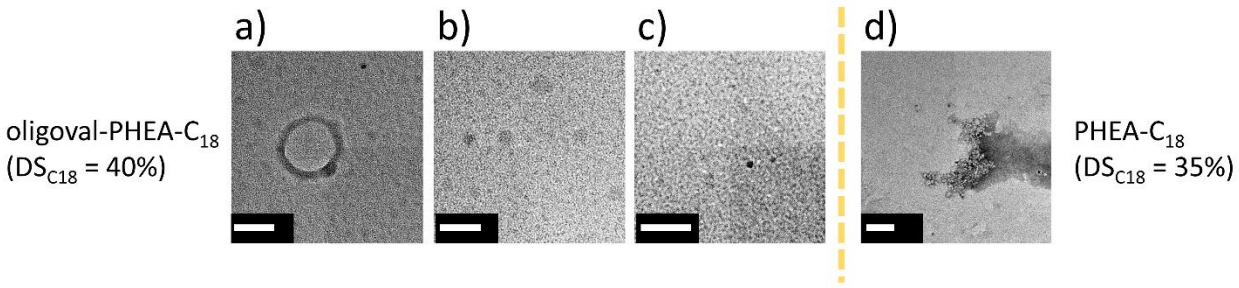

Figure 4.13 Oligovaline-PHEA-C_{18} (DS_{C18}=40%) polymeric vesicles formed with the off-chip precipitation (a) and polymer aggregates formed from microfluidic mixing at FRR-10 (b) and FRR-20 (c). NH_2-PHEA-C_{18} with DS_{C18} of 35 % could not form a polymersome with microfluidic mixing at FRR-20 (d). The white scale bars represent 100 nm.

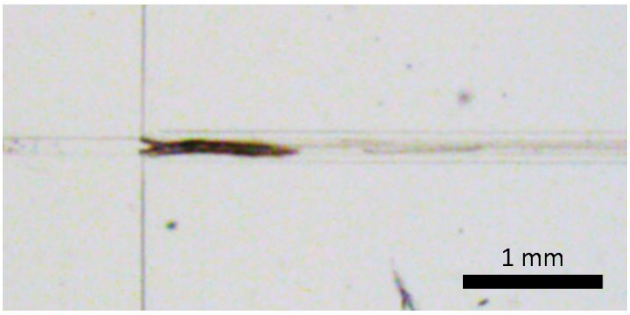

Figure 4.14 Brightfield image of flow-focusing region after fabricating oligovaline-PHEA-C_{18} (DS_{C18} = 40 %) nanoparticles. Scale bar corresponds to 1 mm.

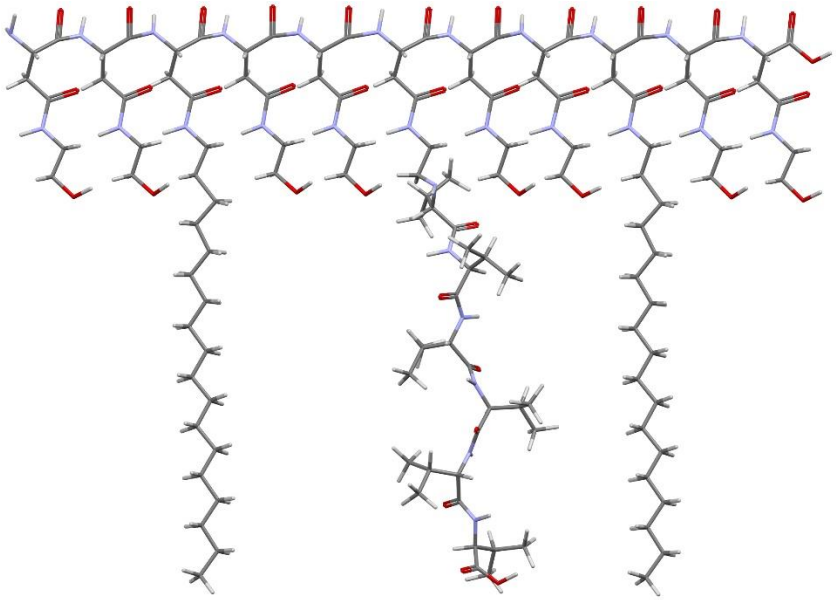

Figure 4.15 Schematic of polymer with 11 units used to approximate PHEA molecules for molecular simulation.

4.6 References

(1) Taborga, L.; Díaz, K.; Olea, A. F.; Reyes-Bravo, P.; Flores, M. E.; Peña-Cortés, H.; Espinoza, L. Effect of Polymer Micelles on Antifungal Activity of Geranylorcinol Compounds against Botrytis Cinerea. *J. Agric. Food Chem.* **2015**, *63* (31), 6890–6896.
(2) Xu, X.; Ni, X.; Cao, Y.; Zhuo, X.; Yang, X.; Cao, G. Amphiphilic Polymeric Micelle as Pseudostationary Phase in Electrokinetic Chromatography for Analysis of Eight Corticosteroids in Cosmetics. *Electrophoresis* **2014**, *35* (6), 827–835.
(3) Spagnuolo, P. A.; Dalgleish, D. G.; Goff, H. D.; Morris, E. R. Kappa-Carrageenan Interactions in Systems Containing Casein Micelles and Polysaccharide Stabilizers. *Food Hydrocoll.* **2005**, *19* (3), 371–377.
(4) Levine, D. H.; Ghoroghchian, P. P.; Freudenberg, J.; Zhang, G.; Therien, M. J.; Greene, M. I.; Hammer, D. A.; Murali, R. Polymersomes: A New Multi-Functional Tool for Cancer Diagnosis and Therapy. *Methods* **2008**, *46* (1), 25–32.
(5) Jones, M.-C.; Leroux, J.-C. Polymeric Micelles – a New Generation of Colloidal Drug Carriers. *Eur. J. Pharm. Biopharm.* **1999**, *48* (2), 101–111.
(6) Shao, Y.; Shi, C.; Xu, G.; Guo, D.; Luo, J. Photo and Redox Dual Responsive Reversibly Cross-Linked Nanocarrier for Efficient Tumor-Targeted Drug Delivery. *ACS Appl. Mater. Interfaces* **2014**, *6* (13), 10381–10392.
(7) Kulkarni, P. S.; Haldar, M. K.; Nahire, R. R.; Katti, P.; Ambre, A. H.; Muhonen, W. W.; Shabb, J. B.; Padi, S. K. R.; Singh, R. K.; Borowicz, P. P.; et al. MMP-9 Responsive PEG Cleavable Nanovesicles for Efficient Delivery of Chemotherapeutics to Pancreatic Cancer. *Mol. Pharm.* **2014**, *11* (7), 2390–2399.
(8) Lai, M.-H.; Clay, N. E.; Kim, D. H.; Kong, H. Bacteria-Mimicking Nanoparticle Surface Functionalization with Targeting Motifs. *Nanoscale* **2015**, *7* (15), 6737–6744.
(9) Meng, F.; Engbers, G. H. M.; Feijen, J. Biodegradable Polymersomes as a Basis for Artificial Cells: Encapsulation, Release and Targeting. *J. Controlled Release* **2005**, *101* (1–3), 187–198.
(10) Vijayakrishna, K.; Mecerreyes, D.; Gnanou, Y.; Taton, D. Polymeric Vesicles and Micelles Obtained by Self-Assembly of Ionic Liquid-Based Block Copolymers Triggered by Anion or Solvent Exchange. *Macromolecules* **2009**, *42* (14), 5167–5174.
(11) Houga, C.; Giermanska, J.; Lecommandoux, S.; Borsali, R.; Taton, D.; Gnanou, Y.; Le Meins, J.-F. Micelles and Polymersomes Obtained by Self-Assembly of Dextran and Polystyrene Based Block Copolymers. *Biomacromolecules* **2009**, *10* (1), 32–40.
(12) Marsden, H. R.; Gabrielli, L.; Kros, A. Rapid Preparation of Polymersomes by a Water Addition/solvent Evaporation Method. *Polym. Chem.* **2010**, *1* (9), 1512–1518.
(13) Ahmed, F.; Discher, D. E. Self-Porating Polymersomes of PEG-PLA and PEG-PCL: Hydrolysis-Triggered Controlled Release Vesicles. *J. Control. Release Off. J. Control. Release Soc.* **2004**, *96* (1), 37–53.
(14) Saadat, E.; Amini, M.; Dinarvand, R.; Dorkoosh, F. A. Polymeric Micelles Based on Hyaluronic Acid and Phospholipids: Design, Characterization, and Cytotoxicity. *J. Appl. Polym. Sci.* **2014**, *131* (20), n/a-n/a.
(15) Johnson, R. P.; Jeong, Y.-I.; Choi, E.; Chung, C.-W.; Kang, D. H.; Oh, S.-O.; Suh, H.; Kim, I. Biocompatible Poly(2-Hydroxyethyl Methacrylate)-B-poly(L-Histidine) Hybrid Materials for pH-Sensitive Intracellular Anticancer Drug Delivery. *Adv. Funct. Mater.* **2012**, *22* (5), 1058–1068.

(16) Zhao, L.; Li, N.; Wang, K.; Shi, C.; Zhang, L.; Luan, Y. A Review of Polypeptide-Based Polymersomes. *Biomaterials* **2014**, *35* (4), 1284–1301.
(17) Nagarajan, R. Molecular Packing Parameter and Surfactant Self-Assembly: The Neglected Role of the Surfactant Tail†. *Langmuir* **2002**, *18* (1), 31–38.
(18) Maibaum, L.; Dinner, A. R.; Chandler, D. Micelle Formation and the Hydrophobic Effect. *J. Phys. Chem. B* **2004**, *108* (21), 6778–6781.
(19) Lee, C.-Y.; Chang, C.-L.; Wang, Y.-N.; Fu, L.-M. Microfluidic Mixing: A Review. *Int. J. Mol. Sci.* **2011**, *12* (5), 3263–3287.
(20) Stachowiak, J. C.; Richmond, D. L.; Li, T. H.; Liu, A. P.; Parekh, S. H.; Fletcher, D. A. Unilamellar Vesicle Formation and Encapsulation by Microfluidic Jetting. *Proc. Natl. Acad. Sci.* **2008**, *105* (12), 4697–4702.
(21) Whitesides, G. M. The Origins and the Future of Microfluidics. *Nature* **2006**, *442* (7101), 368–373.
(22) Phapal, S. M.; Sunthar, P. Influence of Micro-Mixing on the Size of Liposomes Self-Assembled from Miscible Liquid Phases. *Chem. Phys. Lipids* **2013**, *172–173*, 20–30.
(23) Tian, Z.-H.; Xu, J.-H.; Wang, Y.-J.; Luo, G.-S. Microfluidic Synthesis of Monodispersed CdSe Quantum Dots Nanocrystals by Using Mixed Fatty Amines as Ligands. *Chem. Eng. J.* **2016**, *285*, 20–26.
(24) Shah, R. K.; Shum, H. C.; Rowat, A. C.; Lee, D.; Agresti, J. J.; Utada, A. S.; Chu, L.-Y.; Kim, J.-W.; Fernandez-Nieves, A.; Martinez, C. J.; et al. Designer Emulsions Using Microfluidics. *Mater. Today* **2008**, *11* (4), 18–27.
(25) Karnik, R.; Gu, F.; Basto, P.; Cannizzaro, C.; Dean, L.; Kyei-Manu, W.; Langer, R.; Farokhzad, O. C. Microfluidic Platform for Controlled Synthesis of Polymeric Nanoparticles. *Nano Lett.* **2008**, *8* (9), 2906–2912.
(26) Phillips, T. W.; Lignos, I. G.; Maceiczyk, R. M.; deMello, A. J.; deMello, J. C. Nanocrystal Synthesis in Microfluidic Reactors: Where Next? *Lab. Chip* **2014**, *14* (17), 3172.
(27) Lu, Y.; Park, K. Polymeric Micelles and Alternative Nanonized Delivery Vehicles for Poorly Soluble Drugs. *Int. J. Pharm.* **2013**, *453* (1), 198–214.
(28) Tomida, M.; Nakato, T.; Kuramochi, M.; Shibata, M.; Matsunami, S.; Kakuchi, T. Novel Method of Synthesizing Poly(succinimide) and Its Copolymeric Derivatives by Acid-Catalysed Polycondensation of L-Aspartic Acid. *Polymer* **1996**, *37* (19), 4435–4437.
(29) Daly, W. H.; Poché, D. The Preparation of N-Carboxyanhydrides of α-Amino Acids Using Bis(trichloromethyl)carbonate. *Tetrahedron Lett.* **1988**, *29* (46), 5859–5862.
(30) Christian, D. A.; Cai, S.; Bowen, D. M.; Kim, Y.; Pajerowski, J. D.; Discher, D. E. Polymersome Carriers: From Self-Assembly to siRNA and Protein Therapeutics. *Eur. J. Pharm. Biopharm. Off. J. Arbeitsgemeinschaft Pharm. Verfahrenstechnik EV* **2009**, *71* (3), 463–474.
(31) Wibowo, S. H.; Sulistio, A.; Wong, E. H. H.; Blencowe, A.; Qiao, G. G. Polypeptide Films via N-Carboxyanhydride Ring-Opening Polymerization (NCA-ROP): Past, Present and Future. *Chem. Commun.* **2014**, *50* (39), 4971.
(32) Senn, H.; Werner, B.; Messerle, B. A.; Weber, C.; Traber, R.; Wüthrich, K. Stereospecific Assignment of the Methyl 1H NMR Lines of Valine and Leucine in Polypeptides by Nonrandom 13C Labelling. *FEBS Lett.* **1989**, *249* (1), 113–118.
(33) Dalhus, B.; Görbitz, C. H.; Kofod, P.; Larsen, E.; Nielsen, B.; Nielsen, R. I.; Olsen, C. E.; Rosendahl, C. N.; Haugg, M.; Trabesinger-Rüf, N.; et al. Crystal Structures of Hydrophobic Amino Acids. I. Redeterminations of L-Methionine and L-Valine at 120 K. *Acta Chem. Scand.* **1996**, *50*, 544–548.

(34) Geng, Y.; Discher, D. E. Hydrolytic Degradation of Poly(ethylene Oxide)-Block-Polycaprolactone Worm Micelles. *J. Am. Chem. Soc.* **2005**, *127* (37), 12780–12781.
(35) Rameez, S.; Bamba, I.; Palmer, A. F. Large Scale Production of Vesicles by Hollow Fiber Extrusion: A Novel Method for Generating Polymersome Encapsulated Hemoglobin Dispersions. *Langmuir ACS J. Surf. Colloids* **2010**, *26* (7), 5279–5285.
(36) Flory, P. J. Thermodynamics of High Polymer Solutions. *J. Chem. Phys.* **1942**, *10* (1), 51–61.
(37) Jawalkar, S. S.; Raju, K. V. S. N.; Halligudi, S. B.; Sairam, M.; Aminabhavi, T. M. Molecular Modeling Simulations to Predict Compatibility of Poly(vinyl Alcohol) and Chitosan Blends: A Comparison with Experiments. *J. Phys. Chem. B* **2007**, *111* (10), 2431–2439.
(38) Zhang, C.; Liu, B.; Wang, X.; Wang, H.; Zhang, H. Measurement and Correlation of Solubility of L-Valine in Water + (Ethanol, N,N-Dimethylformamide, Acetone, Isopropyl Alcohol) from 293.15 K to 343.15 K. *J. Chem. Eng. Data* **2014**, *59* (9), 2732–2740.
(39) Xiao, X.; Hu, J.; Charych, D. H.; Salmeron, M. Chain Length Dependence of the Frictional Properties of Alkylsilane Molecules Self-Assembled on Mica Studied by Atomic Force Microscopy. *Langmuir* **1996**, *12* (2), 235–237.
(40) Schultz, M. P.; Finlay, J. A.; Callow, M. E.; Callow, J. A. A Turbulent Channel Flow Apparatus for the Determination of the Adhesion Strength of Microfouling Organisms. *Biofouling* **2000**, *15* (4), 243–251.
(41) Johnson, B. K.; Prud'homme, R. K. Mechanism for Rapid Self-Assembly of Block Copolymer Nanoparticles. *Phys. Rev. Lett.* **2003**, *91* (11), 118302.
(42) Wang, Y. J.; Therien-Aubin, H.; Baille, W. E.; Luo, J. T.; Zhu, X. X. Effect of Molecular Architecture on the Self-Diffusion of Polymers in Aqueous Systems: A Comparison of Linear, Star, and Dendritic Poly(ethylene Glycol)s. *Polymer* **2010**, *51* (11), 2345–2350.
(43) Sauvage, E.; Plucktaveesak, N.; Colby, R. h.; Amos, D. a.; Antalek, B.; Schroeder, K. m.; Tan, J. s. Amphiphilic Maleic Acid-Containing Alternating copolymers—2. Dilute Solution Characterization by Light Scattering, Intrinsic Viscosity, and PGSE NMR Spectroscopy. *J. Polym. Sci. Part B Polym. Phys.* **2004**, *42* (19), 3584–3597.
(44) Jahn, A.; Vreeland, W. N.; DeVoe, D. L.; Locascio, L. E.; Gaitan, M. Microfluidic Directed Formation of Liposomes of Controlled Size. *Langmuir* **2007**, *23* (11), 6289–6293.
(45) Sun, H. COMPASS: An Ab Initio Force-Field Optimized for Condensed-Phase ApplicationsOverview with Details on Alkane and Benzene Compounds. *J. Phys. Chem. B* **1998**, *102* (38), 7338–7364.
(46) Nosé, S. A Unified Formulation of the Constant Temperature Molecular Dynamics Methods. *J. Chem. Phys.* **1984**, *81* (1), 511–519.
(47) Schmidt, F. R. Optimization and Scale up of Industrial Fermentation Processes. *Appl. Microbiol. Biotechnol.* **2005**, *68* (4), 425–435.
(48) Sabotin, I.; Tristo, G.; Junkar, M.; Valentinčič, J. Two-Step Design Protocol for Patterned Groove Micromixers. *Chem. Eng. Res. Des.* **2013**, *91* (5), 778–788.

CHAPTER 5: FLOW-MEDIATED STEM CELL LABELING WITH SUPERPARAMAGNETIC IRON OXIDE NANOPARTICLE CLUSTERS[4]

5.1 Introduction

Stem and progenitor cells possess the potential to treat various acute and chronic diseases and tissue defects, due to their multipotent differentiation capacity, trophic factor secretion, and immunosuppressive activities.[1] In mesenchymal stem cell therapies, stem cells are isolated from a patient's bone marrow or adipose tissue, expanded to therapeutic levels ex vivo, and then reinjected locally or systemically.[2] To better understand and modulate cellular therapeutic activities, clinicians must assess the localization and bioavailability of transplanted cells in vivo using a clinical imaging modality, such as magnetic resonance imaging (MRI).

Toward this goal, extensive efforts have been made to label stem cells ex vivo with superparamagnetic iron oxide nanoparticles (SPIONs), a popular T_2 contrast agent capable of highly sensitive in vivo imaging.[3] One emerging, simple method to modulate SPION size and

[4] This chapter is adapted with permission from Clay, N.; Baek, K.; Shkumatov, A; Lai, M.; Smith, C.E.; Rich, M.; Kong, H. Flow-mediated Stem Cell Labeling with Superparamagnetic Iron Oxide Nanoparticle Clusters. Copyright 2013 American Chemical Society. This work was supported by the National Institute of Health (1R01 HL109192 to H.J.K. and R25 CA154015A to N.C.). We would like to thank Dr. Boris Odintsov for help with MR imaging, Dr. Mayandi Sivaguru for help with confocal and cell imaging, Dr. Wacek Swiech for help with TEM images, and Rudy Laufhutte for ICP measurements. Special appreciation is given to Ian Baek for optimizing the computational simulations used herein.

functionality for labeling is to cluster several SPIONs together using self-assembling polymers with diverse functional groups.[4,5] In this way, a cluster is formed, containing multiple SPIONs surrounded by a polymeric coating already grafted with various biomolecules of interest. With this technique, the size of the SPION cluster can be controlled through the concentration and chemical structure of the self-assembling molecules, in turn allowing SPION clusters to be easily tuned for enhanced receptor-mediated endocytosis[6] or maximum T_2 relaxivity.[7] In addition, the cluster formation process avoids the extensive conjugation and purification steps required in the direct surface modifications of SPIONs.[8–10] Despite the advantages offered by this clustering technique, advanced methods are still needed to increase SPION loading efficiency within cells, as cell proliferation and SPION exocytosis results in a gradual reduction of the MR signal in vivo, in turn limiting the long-term effectiveness of cell tracking.[11] Therefore, we sought to develop a new method to tailor the cellular uptake of SPION clusters and improve cell tracking, apart from conventional approaches that rely on changes to SPION size, charge, and surface chemistry[12] or potentially harmful external stimuli such as electroportation.[13] With this strategy, we also seek to maintain cell viability and function. According to recent cell biology studies, the extracellular mechanical environment regulates the endocytosis and exocytosis of extracellular components both in vitro and in vivo.[14] For example, shear flow has been shown to affect adhesion and endocytosis of quantum dots to endothelial cells.[15] Aligned with these findings, we hypothesized that cells exposed to an external flow in vitro would ingest a greater amount of SPION clusters grafted with integrin-binding peptides.

We examined this hypothesis by coincubating bone marrow-derived mesenchymal stem cells (BMSCs) with SPION clusters. These SPION clusters are coated with integrin-binding peptides containing an Arg-Gly-Asp (RGD) sequence. BMSCs were labeled with RGD-SPION clusters on

an orbital shaker rotating at controlled speeds, at which the average cluster velocity and shear stress on the cell membrane were estimated to increase. The resulting cell labeling efficiency was evaluated by measuring RGD-SPION clusters per cell using inductively coupled plasma (ICP) spectroscopy and independently confirmed by measuring the relaxivity of labeled BMSCs in a collagen gel. Finally, cell labeling under orbital flow was demonstrated by locally injecting BMSCs labeled with RGD-SPION clusters into the muscle of a mouse's hindlimb and imaging the leg with MRI. Taken together, this study will serve to improve the effectiveness of cell tracking and, ultimately, the therapeutic activities of a wide range of cells.

5.2 Results

5.2.1 Synthesis of amphiphilic polyaspartamide and SPION clusters

We first synthesized poly(2-hydroxyethyl aspartamide) (PHEA) grafted with octadecyl chains and RGD peptides (termed RGD-PHEA-C_{18}) for use in SPION clustering. The octadecyl chains allow PHEA to associate with a hydrophobic moiety.[5] Separately, the RGD peptides of PHEA bind with cellular integrin domains, including β_1.[16] The sequential addition of octadecylamine, GGGGRGDSP peptide, and ethanolamine to polysuccinimide (PSI) resulted in PHEA substituted with octadecyl chains, GGGGRGDSP, and hydroxyl groups, as confirmed through ^{1}H NMR (Figures 5.1, 5.2, and 5.3a).[17] The degree of substitution (DS_{C18}) of octadecyl chain was approximately 6.7%, as calculated with ^{1}H NMR. Next, the resulting RGD-PHEA-C_{18} was mixed with OA-SPIONs prepared from the thermal decomposition of iron acetylacetonate (Figure 3b).[18] Adding an aqueous solution of RGD-PHEA-C_{18} to OA-SPIONs suspended in chloroform resulted in RGD-SPION clusters. After removing the chloroform, the resulting clusters were readily suspended in DI water without noticeable aggregation (Figure 5.3c and 5.3d). Here, cluster

formation is driven by the intercalation of the oleic acid ligand from OA-SPIONs and the octadecyl chains of PHEA.[19] The mean diameter of cluster was approximately 43 nm, as reported by DLS (Figure 5.4). A polydispersity index of less than 0.2 is reported, demonstrating a good degree of cluster size control. In addition, the RGD-SPION clusters were less than 50 nm in diameter, which was suggested as a size range to facilitate receptor-mediated endocytosis.[6] The T_2 relaxivity of RGD-SPION clusters was around 135 $mM^{-1}s^{-1}$ (Figure 5.3e), comparable to that of FDA-approved contrast agents such as Feridex.[20] The RGD-SPION clusters suspended in PBS remained stable at 4 °C for over three weeks.

5.2.2 Computational simulation of SPION cluster velocity and orbital shear

Separately, computational simulations and mathematical calculations were conducted to estimate the average velocity of RGD-SPION clusters and the shear stress on the cell membrane. According to a COMSOL simulation, the average velocity of RGD-SPION clusters in the static condition was around 0.2 mm (Figure 5.5). The cluster velocity was minimally changed by increasing the orbital speed to 20 rpm. Further increasing the orbital speed to 50 rpm resulted in a significant increase of cluster velocity to 1.5 mm/s, an order of magnitude difference from the speed in the static condition.

In parallel, shear stress on the cell membrane was approximated by

$$\tau_w = R\sqrt{\rho\mu\Omega^3} \quad (5.1)$$

where R is the orbital radius of the shaker (20 mm), ρ is the density of the culture medium (0.9973 g/mL), μ is the dynamic viscosity of the medium (0.0102 Pa-s), and Ω is the angular velocity (rad/s).[21]

According to this calculation, increasing the orbital speed from 0 to 20 and 50 rpm increased shear stress from 0 to 0.6 and 2.4 dyn/cm^2, respectively (Figure 5.6). On the basis of previous studies, shear stress levels as low as 0.2 dyn/cm^2 have been shown to influence cellular gene incorporation, suggesting that a minimum shear level is needed to stimulate cells.[22] Alternatively, increasing the orbital speed past a certain limit, such as 100 rpm, was shown to cause extensive media drying due to the increasingly violent motion of the media.[23]

5.2.3 Evaluation of stem cell labeling efficiency under shaking

To assess whether or not shear stress and cluster velocity influenced RGD-SPION cluster uptake, we labeled BMSCs under orbital speeds ranging from 0 to 20 and 50 rpm. As hypothesized, BMSCs labeled at orbital velocity of 50 rpm took up more RGD-SPION clusters than those labeled under static conditions, as evidenced by Prussian blue staining (Figure 5.7a-I and 5.7a-II). An ICP analysis further confirmed a significant increase of the iron content per cell (Figure 5.7b). BMSCs labeled at 20 and 50 rpm took up a 1.6- and 1.8-fold greater amount of RGD-SPION clusters than those labeled under static condition, respectively. At 50 rpm, the iron content per cell was approximately 7 pg Fe, which was over four times larger than the widely accepted benchmark for cell tracking in vivo (i.e., 1.5 pg/cell).[24] Note that the cellular uptake of RGD-SPION clusters was significantly increased even at an orbital velocity of 20 rpm, at which the cluster velocity was not significantly increased. Despite such high iron loading per cell, over 85% of cells remained viable across all orbital speeds, as determined through a Trypan Blue assay. This viability level was comparable to that of cells cultured in static conditions without RGD-SPION clusters, suggesting that neither shaking nor SPION loading affects viability.

These interesting effects of orbital flow on cell labeling efficiency became insignificant when the concentration of FBS in the cell culture media (Φ_{FBS}) was decreased from 10% to 1%. As characterized with both Prussian blue staining and ICP, the iron content per cell was independent of orbital velocity (Figure 5.7a-III, 5.7a-IV, and 5.7c). Accordingly, the iron content per cell was independent of changes in cluster velocity and shear stress at low Φ_{FBS}. In addition, for cells exposed to orbital flow, the iron content per cell was decreased by reducing Φ_{FBS} from 10% to 1%. In contrast, labeling efficiency in static conditions was independent of Φ_{FBS}.

5.2.4 BMSC phenotype changes under orbital shear

To further address the underlying mechanism by which the orbital velocity and the concentration of FBS (Φ_{FBS}) affect the cellular uptake of RGD-SPION clusters, we first examined whether one or both of these experimental variables modulated the frequency of cellular division. According to previous gene transfection studies, more frequent cell division is correlated with improved uptake of plasmid DNA complexes.[25] According to an MTT assay, decreasing Φ_{FBS} to 1% significantly limited cell metabolic activity and proliferation, as assessed with a decrease in the amount of MTT reagent reduced by metabolically active cells over time (Figure 5.8). However, at a given Φ_{FBS}, the degree of increase in cell proliferation was independent of the orbital velocity. Therefore, the iron content per cell was not dependent on cell proliferation.

In parallel, we examined the effects of orbital velocity and Φ_{FBS} on β_1 integrin cluster formation, as integrin clustering is reported to be a key step in the cellular incorporation of RGD-coated gene complexes.[26] Total cellular β_1 integrin expression level was significantly reduced with decreasing Φ_{FBS} (Figure 5.9). There was not a noticeable difference of the total β_1 integrin expression between cells cultured in the static and shaking conditions at a given Φ_{FBS} (Figure 5.9a

and 5.9b). In contrast, at Φ_{FBS} of 10%, cells cultured under orbital flow displayed a large number of integrin clusters, marked by large fluorescent islands with a cross-sectional area of approximately 0.8 μm^2 (Figure 5.9a and 5.9c). Almost no integrin clusters were observed within cells cultured in a static condition (Figure 5.9a and 5.9c). In addition, no significant integrin cluster formation was visualized with cells cultured at Φ_{FBS} of 1%. Overall, the iron content per cell, modulated by the orbital flow velocity and Φ_{FBS}, could be related to the degree of intracellular integrin cluster formation but not to the total integrin expression level.

5.2.5 Stem cell labeling under shaking for in vitro and in vivo imaging

Finally, we evaluated whether this labeling protocol would generate different levels of MR contrast both in vitro and in vivo. According to MR images of BMSCs loaded in a tissue-like 3D collagen gel, the largest degree of negative contrast, or hypointensity, was observed in gels containing cells labeled with RGD-SPION clusters at 50 rpm and Φ_{FBS} of 10% (Figure 5.10a and 5.10b). Similarly, the inverse of T_2 ($1/T_2$) of each gel, calculated with an array of echo times, was highest for BMSCs labeled at 50 rpm and Φ_{FBS} of 10% (Figure 5.10c). A larger $1/T_2$ value represents a greater amount of RGD-SPION clusters per cell, as confirmed with the highly linear relationship between $1/T_2$ and iron content per cell (Figure 5.10d).

Lastly, we injected BMSCs labeled under static and shaking conditions into the right hindlimb of a mouse (Figure 5.11a). Injecting stem cells in this manner is often used to treat ischemia.[27] The concentration of FBS in the cell culture media was kept constant at 10%, and BMSCs were only labeled at static conditions and at 50 rpm. Unlabeled BMSCs were used as a control. A hindlimb injected with BMSCs labeled under orbital flow displayed a greater degree of hypointensity than a hindlimb injected with cells labeled in the static condition (Figure 5.11b-II and 5.11b-III). This

hypointense area was more localized by injecting a collagen gel loaded with BMSCs labeled at 50 rpm (Figure 5.11b-IV). No noticeable hypointense region was observed in hindlimbs injected with unlabeled BMSCs (Figure 5.11b-I).

5.3 Discussion

Taken together, we have successfully demonstrated that the extracellular mechanical environment plays an important role in stem cell labeling with MR contrast agents. The use of mechanical stimuli to control cell labeling is unique, as previous attempts to improve SPION uptake in stem cells were based mostly on the surface modification of SPIONs. In early attempts, researchers added a cell-penetrating peptide[28] (such as HIV-tat) or a transfection agent (such as Lipofectamine or poly l-lysine)[29] to the SPION surface to improve SPION loading per cell. More recently, researchers explored a variety of polymer coatings on the SPION surface in order to enhance cellular uptake. For example, a layer-by-layer electrostatic assembly technique was used to introduce polyethyleneimine, chitosan, dextran, and other polymers to the SPION surface.[30] Another alternative technique coated the SPION surface with a layer of silica, allowing a variety of functional groups to be conjugated on the silica–SPION surface.[31] However, concerns have been raised over the cytotoxicity and overall usefulness of these methods. For example, HIV-tat coated SPIONs located specifically to the nucleus, which might interfere with cellular function and differentiation.[28] In addition, the introduction of new coatings on the SPION surface requires a laborious chemical synthesis and subsequent purification. Our labeling technique, on the other hand, requires a one-step method to prepare the RGD-SPION clusters, relies on nonchemical methods to improve SPION uptake, and maintains cell viability in a variety of cellular environments.

When compared to other methods to externally stimulate SPION uptake, our labeling technique again has noticeable advantages. Previously reported external techniques to enhance cell labeling included electroporation[13] or the use of a piezoactuator. However, these methods have been shown to compromise cell viability[32] and can be technically challenging.[33] In contrast, our cell labeling procedure only requires an orbital shaker, which is an inexpensive, easy-to-use piece of equipment readily available in research laboratories and operation rooms. One shaker can contain several flasks, allowing for millions of cells to be labeled simultaneously. In addition, orbital shaking has no significant effect on cell viability. Improvements to this protocol can be made to enable highly effective stem cell labeling. For example, we suggest that cells labeled by advanced SPION systems with high T_2 relaxivity (e.g., 700 $mM^{-1}s^{-1}$) under orbital shaking would further improve stem cell tracking quality.

To better understand this protocol, we explored the changes in cell–nanoparticle interaction and cell phenotype that occurred under shaking. Initially, we hypothesized that the cellular uptake of RGD-SPION clusters was dependent on both average particle velocity and shear stress on the cell membrane. However, a considerable increase in iron content per cell was discovered for BMSC labeling at 20 rpm, where only shear stress was significantly increased. This trend suggested that mechanotransduction played a more significant role in regulating the cellular uptake of nanoparticle clusters than changes in average cluster velocity. The continued increase of the iron content per cell from 20 to 50 rpm likely resulted from a larger magnitude of mechanical stimulation. Further mechanistic studies on cellular division, integrin expression, and integrin cluster formation demonstrated that the mechanism by which the shear stress increased cellular SPION cluster uptake was likely related to integrin cluster upregulation, a known intermediary step in integrin-mediated endocytosis. Additionally, we demonstrated that serum was an important

element to switch on cellular mechanosensitivity, as confirmed with the minimal dependency of RGD-SPION cluster uptake on orbital flow in low serum conditions. However, further work will be necessary to fully understand the specific endocytotic pathway.

5.4 Conclusion

In conclusion, this study offers the first step in a new, nonchemical method for simple but elaborate stem cell labeling based on manipulating the extracellular mechanical environment. We believe that this flow-modulated cell labeling procedure will greatly benefit MR-based cell tracking, as this method avoids the laborious chemical modifications and carefully refined protocols found in previous studies. Previous studies demonstrated that external shear flow influences cellular uptake of gene complexes and nanoparticles (e.g., quantum dot and silica nanoparticles) in microfluidic systems.[34] However, this is the first study to demonstrate that shear conditions readily modulated by a conventional orbital shaker can stimulate efficient mesenchymal stem cell labeling with SPIONs. Unlike complex microfluidic systems, an orbital shaker is readily available in clinical settings for cell labeling. Therefore, we believe that this protocol would be useful for labeling a wide array of stem cells and islets[35] with SPIONs for diagnosing and treating various diseases and tissue defects. We suggest that the effects of external flow on cell labeling would be further amplified by tailoring other external extracellular environmental factors such as cell adhesion ligands, cell adherent matrix stiffness, and growth factors in media.[36] Finally, we envision that this method would be readily utilized for improving the cellular uptake of exogenous genes (e.g., siRNA and DNA) as well as other nanoparticles used for imaging and treatments.[37]

5.5 Materials and Methods

Materials were purchased from Sigma Aldrich unless otherwise specified.

5.5.1 Synthesis of oleic acid-coated superparamagnetic iron oxide nanoparticles (OA-SPIONs)

Five nm diameter iron oxide nanoparticles were prepared from the thermal decomposition of iron acetylacetonate.[18] First, a three-neck flask was charged with 0.2 g of iron acetylacetonate, 660 μL of oleic acid, 600 μL of oleylamine, and 0.7 g of 1,2-dodecanediol. All compounds were dissolved in 6.7 mL of benzyl ether. Under nitrogen flow, the mixture was heated to 200 °C for 2 h and then slowly heated up to 300 °C under reflux for 1 h with gentle stirring. To purify the SPIONs, the reaction mixture was precipitated with ethanol (Declon) and then magnetically separated (K & J Magnetics). These oleic acid-coated SPIONs (termed "OA-SPIONs") were finally dispersed in chloroform at 10 mg/mL and stored at −20 °C until further analysis.

5.5.2 Synthesis of polysuccinimide

Polysuccinimide (PSI) was prepared from the thermal condensation of aspartic acid, as previously reported.[38] In a two-neck flask, 25 g of aspartic acid was dissolved in the presence of 125 mL of mesitylene and 125 mL of sulfolane. The mixture was heated to 180 °C under nitrogen, and then, 240 μL of phosphoric acid was injected to catalyze the reaction. The reaction was run overnight, after which the reaction mixture was vacuum filtered, washed thoroughly with methanol and water, and then lyophilized.

5.5.3 Synthesis of PHEA substituted with octadecyl chains (C_{18}) and RGD peptides (RGD-PHEA-C_{18})

To prepare RGD-PHEA-C_{18}, 0.4 g of PSI was dissolved in 10 mL of dimethylformamide (DMF). Then, 59 mg of octadecylamine was added to this mixture and reacted overnight. Afterward, 32 mg of GGGGRGDSP (Mimotope Peptide) was added to the mixture and then reacted for 5 h, followed by 1 mL of ethanolamine for 3 h. All reaction steps were completed under nitrogen at room temperature in water-free conditions. After completion, the reaction mixture was added to a dialysis bag (MWCO 3,500; Fisher) and then dialyzed against DI water for 48 h, while adding fresh water at least four times. NaCl was added to water for the first round of dialysis. Afterward, the product was frozen and then lyophilized (Labconco) for 48 h to obtain a dried product. Total yield ranged from 70 to 90%. ^{1}H NMR (Varian VXR 500 with Unity Inova Console) was used to analyze the product dissolved in DMSO-d_6. For accurate shimming, the temperature of the NMR probe was greater than 30 °C.

5.5.4 Quantification of octadecyl chain engraftment to PHEA

Using ^{1}H NMR and an established protocol,[17] the degree of octadecylamine substitution (DS_{C18}) was quantified by the following equation:

$$DS_{C18} = \frac{peak\ integration\ from\ 0.8\ to\ 0.9\ ppm}{3(peak\ integration\ from\ 4.3\ to\ 4.7\ ppm)} \times 100\% \quad (5.2)$$

5.5.5 Preparation of SPION clusters with RGD-PHEA-C_{18}

To prepare RGD-SPION clusters, 400 µL of 5 mg/mL OA-SPIONs suspended in chloroform was added to 8 mL of 5 mg/mL RGD-PHEA-C_{18} in DI water. The mixture was quickly sonicated (Fisher Scientific) in order to form a cloudy suspension. Using a rotary evaporator (Heidolph), the

chloroform phase was removed from the suspension after about 20 min. The concentrated RGD-SPION cluster suspension was first transferred to a centrifuge tube and then centrifuged at 4000 rpm for 10 min (Eppendorf 5180R). Afterward, the supernatant was collected. By collecting the supernatant, sediments containing nonencapsulated and unstable SPIONs were removed and then discarded. In this way, we could only retain stable RGD-SPION clusters for further purification. Next, to remove free RGD-PHEA-C_{18}, the supernatant was centrifuged at 15 000 rpm for 20 min (Eppendorf 5424), allowing RGD-SPION clusters to be separated out. Finally, RGD-SPION clusters were reconstituted in Dulbecco's modified Eagle's medium (DMEM, Corning Cellgro) with gentle bath sonication (Fisher) and stored at 4 °C until further usage.

5.5.6 Analysis of iron content in RGD-SPION clusters and cells

Iron content in RGD-SPION clusters and in BMSCs was quantified through inductively coupled plasma spectrometry (ICP, Perkinelmer 2000 DV). All samples were dissolved in nitric acid (Macron) and then diluted to 5 mL with DI water. NIST primary standards were used for instrument calibration. Samples were fed into the instrument with a peristaltic pump, and an internal standard was used to account for variations in sample fluidity.

5.5.7 Measurement of RGD-SPION size with dynamic light scattering (DLS)

After purification, RGD-SPION clusters were redispersed at a dilute concentration and then analyzed with dynamic light scattering (Malvern Zetasizer). At least three measurements were made, and RGD-SPION cluster diameter was reported as the peak of the number distribution.

5.5.8 Image analysis of OA-SPIONs and RGD-SPION clusters

OA-SPIONs and RGD-SPION clusters were visualized with transmission electron microscopy (TEM). The samples were air-dried on a holey carbon-coated grid and then imaged at 200 kV (JEOL 2100 TEM). To determine the diameter of the OA-SPIONs, at least 50 particles were analyzed using ImageJ software.

5.5.9 Analysis of magnetic resonance (MR) relaxivity of SPION clusters

MR relaxivity of RGD-SPION clusters was measured using a spin–echo sequence (14.1 T Varian MR system). Prior to imaging, the instrument was shimmed with a single-pulse sequence until line width was around 600 Hz. Imaging parameters included receiver gain: 44; repetition time ($t_{repetition}$): 300 ms; echo time (t_{echo}): 9, 10, 11,12, 13, 14 ms; data matrix: 256 × 256; field of view: 30 × 30 mm; slice thickness varied as needed. Total acquisition time was between 10 and 20 min, and a copper sulfate solution was used as a marker. To calculate T_2 values, the mean gray value (termed "relative brightness") from ImageJ was plotted against echo time. Using an exponential fit, the inverse of T_2 was calculated. T_2 relaxivity was quantified from the slope of the curve between the inverse T_2 and iron concentration. For relaxivity measurements, at least five different iron concentrations were used.

5.5.10 BMSC culture

Mouse bone marrow-derived D1 mesenchymal stem cells (ATCC) were cultured in DMEM (Corning Cellgro) supplemented with 10% fetal bovine serum (Thermo Scientific) and 1% penicillin/streptomycin (Gibco). Cells were incubated at 5% CO_2 and 37 °C in sterile conditions.

Cell media was changed every 3 days, and cells were passaged when over 90% confluent. No passage numbers higher than 28 were used.

5.5.11 Coincubation of cells with RGD-SPION clusters

BMSCs were plated in T-25 cell culture flasks at a density of 10,000 cells/cm^2 and then incubated overnight. Afterward, fresh DMEM supplemented with 10% or 1% FBS was added, and then, the cell culture flasks were placed on an orbital shaker set to rotate at 0, 20, or 50 rpm (Heidolph Rotamax 120). The cell culture flasks were shaken for approximately 10 h to allow cells to adapt to their new environment. In previous studies, at least 6 h was necessary for noticeable cellular gene expression changes to take place under shear. After 10 h of continuous shaking, media was removed, and fresh media containing RGD-SPION clusters at a concentration of 0.32 mM Fe was added. Once again, FBS concentration was kept consistent at either 10% or 1%. Then, cells were exposed to orbital flow and RGD-SPION clusters for the next 14 h. After incubation, cells were washed three times with PBS to remove free RGD-SPION clusters. In parallel, cells in a stationary flask were incubated for 10 h without RGD-SPION clusters and then for 14 h with media containing RGD-SPION clusters at a concentration of 0.32 mM Fe, again with a constant FBS concentration. Unlabeled cells incubated for 24 h in a stationary flask at an FBS concentration of 10% served as a control.

5.5.12 Phase contrast imaging of cells incubated with SPION clusters

Following coincubation of BMSCs with RGD-SPION clusters, cells were fixed with 3.7% paraformaldehyde in phosphate buffer saline (PBS) for 30 min. After washing with PBS, Perls reagent (1:1 10% potassium ferrocyanide/1 N HCl) was added for 20 min. In this step, poisonous

hydrogen cyanide is liberated. Then, cells were washed thoroughly with PBS. Images were taken with a Zeiss Axiovert 200 M apotome microscope at 20× and 63×.

5.5.13 ICP analysis of cellular uptake of RGD-SPION clusters

After coincubation with RGD-SPION clusters, cells were washed, trypsinized, counted, and then centrifuged to form a pellet. The pellet was dissolved in concentrated nitric acid overnight at room temperature before analysis. ICP measurements were taken as previously described. At least three aliquots containing 100 000 cells each were used for each sample for ICP analysis.

5.5.14 MR imaging of cells labeled with RGD-SPION clusters

After coincubation with RGD-SPION clusters, cells were washed, trypsinized, and then resuspended in DMEM at 1×10^6 cells/mL. Cells were then embedded in bovine type I collagen gel (PureCol, Advanced Biomatrix) by mixing cells with collagen solution and then increasing pH and temperature to form a gel, as previously reported.[39] Care was taken to avoid air bubbles in the viscous collagen suspension, and the gels were formed within a glass capillary tube at 37 °C. The total concentration of cells in the pregelled solution was approximately 300 cells/μL. After embedding, labeled BMSCs were imaged with a 14.1 T Varian MR system using a spin–echo sequence. Prior to imaging, the instrument was shimmed using a single pulse sequence until line width was less than 600 Hz. MR imaging parameters were as follows: receiver gain: 44; $t_{\text{repetition}}$: 300 ms; t_{echo}: 1, 2, 4, 6, 8, 10 ms; data matrix: 256 × 256; field of view: 30 × 30 mm. Total acquisition time ranged from 10 to 20 min, and a copper sulfate solution was used as a marker. To quantify a mean T_2 value per condition, at least two 0.7 mm thick slices were selected in different locations of each gel.

5.5.15 Analysis of cell viability following cellular uptake of RGD-SPION clusters

The viability of BMSCs incubated with RGD-SPION clusters in static or dynamic conditions was assessed with a Trypan Blue and a 3-(4,5-dimethylthiazol-2-yl)-2,5-diphenyltetrazolium bromide (MTT) reagent assay (ATCC). For Trypan Blue assays, cells were washed with PBS and then incubated with 0.4% Trypan Blue for 5 min. Then, the percentage of live cells was counted using a light microscope (Leica). For the MTT assay, 10 μL of 3-(4,5-dimethylthiazol-2-yl)-2,5-diphenyltetrazolium bromide was added to 100 μL of phenol red-free DMEM with cells and incubated at 37 °C for 4 h. Then, cells were digested in 100 μL of detergent for 2.5 h. Absorbance of cell lysate was read at 570 nm (BioTek Synergy HT).

5.5.16 Immunostaining of β_1 integrins

Cells were fixed with 3.7% paraformaldehyde for 10 min. After washing cells with PBS, samples were incubated with 1% bovine serum albumin, 5% FBS, and 0.3% Triton-X for 1 h to block nonspecific binding and permeabilize cells. Then, cells were incubated with a mouse monoclonal antibody to integrin β_1 (Abcam) overnight at 4 °C. After washing, cells were incubated with goat polycloncal 6563 secondary anitbody-Cy5 (Abcam) for 1 h at room temperature. Dilution ratios were 1:1000 for both the primary and secondary antibodies. Lastly, 4′,6-diamidino-2-phenylindole dihydrochloride (DAPI, Invitrogen) was used to stain cell nuclei at a working concentration of 100 ng/mL.

Nuclei and cellular integrins were imaged using a Zeiss LSM 700 confocal microscope at 40×. ImageJ software was used to quantify the integrin expression level and integrin cluster formation. Each image was separated into three channels, and the mean gray value of the green channel (termed “mean green value”) was determined over the cell area. Here, a higher mean green value

corresponds to a higher relative level of integrin expression. At least 15 cells were analyzed per condition.

5.5.17 Intramuscular hindlimb injection of labeled BMSCs into a mouse model

All mice work was carried out in accordance with university and federal regulations (Institutional Animal Care and Use Committee approval number: 11089). We used three four month old Balb/c and two three month old C57Black mice for our in vivo work. Before cell injection, all mice were anesthetized with isoflurane. Then, a 50 μL BMSC suspension (2×10^6 cells/mL) was injected into the muscles of the right caudal thigh approximately between semimembranosus and semitendinosus muscles, using a 1.0 mL syringe with 25G1 needle. BMSCs labeled in static conditions or at 50 rpm were used in this study, and unlabeled BMSCs were used as a negative control. To help localize the hypointense area, cells labeled at 50 rpm were mixed with 1 mg/mL of type I collagen prior to injection.

5.5.18 In Vivo MR-based tracking of BMSCs

Mice were humanely sacrificed approximately 1 h after injection. Then, both legs of each mouse were imaged with a spin–echo sequence (14.1 T Varian MR system) to locate the transplanted BMSCs. A custom-built coil was used to contain the sacrificed mice, the details of which are described elsewhere.[40] Prior to imaging, the instrument was shimmed manually until line width was around 200 Hz. Imaging parameters include $t_{\text{repetition}}$: 1000–1300 ms; t_{echo}: 40 ms; data matrix: 256 × 256; slice thickness: 0.5–1.0 mm; field of view varied as needed. Coronal cuts were used to identify the hypointense regions, which were subsequently processed in ImageJ. Total

acquisition time was around 20 min, and a copper sulfate solution was used as a marker. Afterward, mouse bodies were disposed of according to university regulations.

5.5.19 Computational simulation of average RGD-SPION cluster velocity

The particle motion in unsteady, free-surface flow inside a 25 mm^2 cell culture flask was simulated using finite element method (FEM) commercial software (COMSOL Multiphysics 3.3). To begin this analysis, 4 mL of media rotated at three different speeds (*f*) of 0, 20, and 50 rpm was simulated. Then, the free surface motion in the liquid–air interface and the particle flow patterns inside the well were analyzed. The orbital shaker imparts the same two-dimensional, in-plane movement to all points on the plate. The velocity of the plate walls (*U*) is thus given by:

$$U = \begin{bmatrix} U_x \\ U_y \\ U_z \end{bmatrix} = \begin{bmatrix} -R_g\Omega\sin(\Omega t) \\ -R_g\Omega\cos(\Omega t) \\ 0 \end{bmatrix} \quad (5.3)$$

where R_g is the orbital radius (~20 mm in this study) and Ω is the angular velocity that is given by

$$\Omega = 2\pi f \quad (5.4)$$

5.5.20 Statistical analysis

All data were analyzed using a two-tailed *t* test with equal variance (Microsoft Excel). $P < 0.05$ was considered the threshold for significance. All samples were done in triplicate unless otherwise noted. Data are represented as mean + standard error of mean (SEM).

5.6 Figures

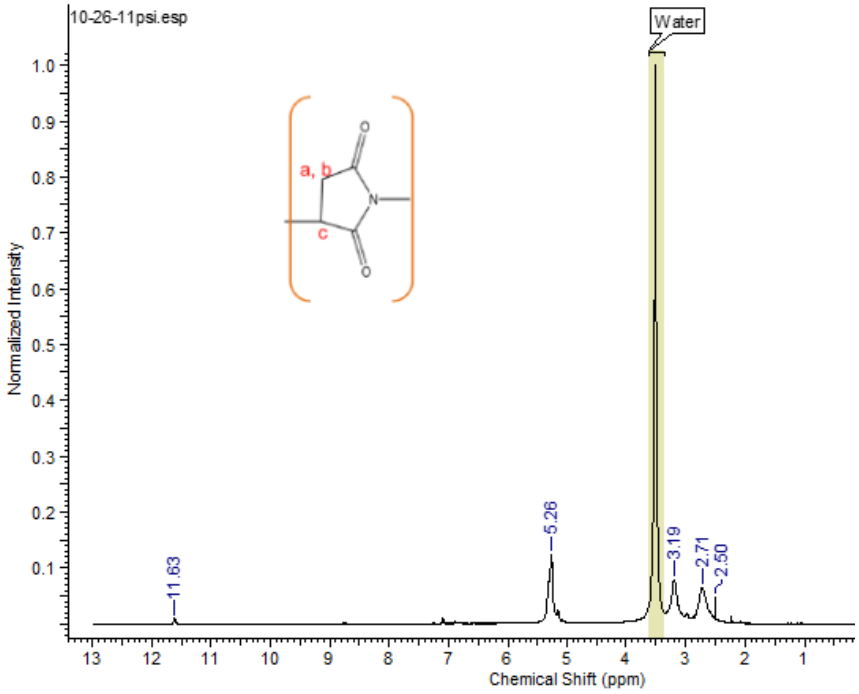

Figure 5.1 ^{1}H-NMR spectrum of polysuccinimide.

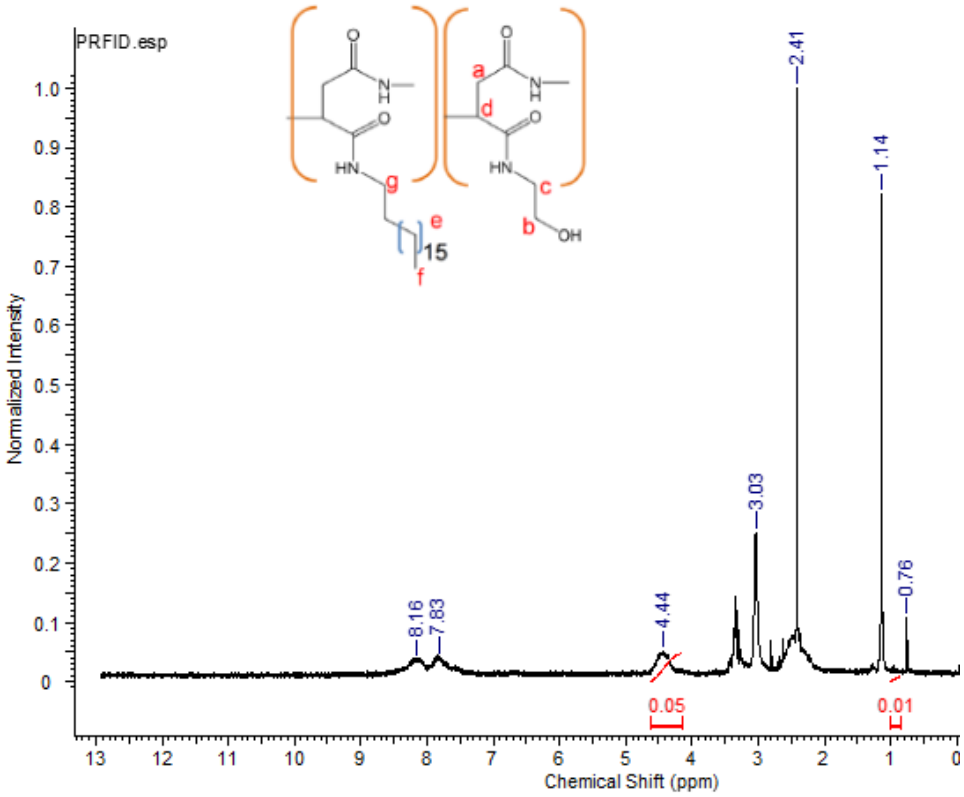

Figure 5.2 ^{1}H-NMR spectrum of RGD-PHEA-C_{18}

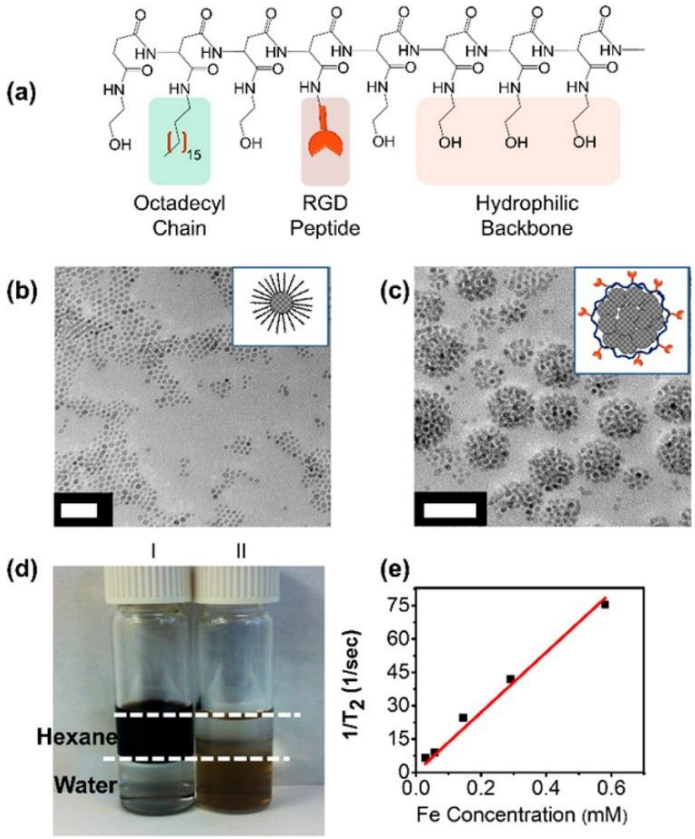

Figure 5.3 Characterization of RGD-PHEA-C_{18} and RGD-SPION cluster. (a) Structure of RGD-PHEA-C_{18}. (b) TEM image of oleic acid-coated SPIONs. (c) TEM image of RGD-SPION clusters. Both scale bars represent 50 nm. (d) OA-coated SPIONs (I) are suspended in hexane, while RGD-SPION clusters (II) are dispersed in water. Dotted white lines help indicate the interface between hexane and water. (e) A plot of $1/T_2$ vs iron concentration used to determine T_2 relaxivity of RGD-SPION clusters.

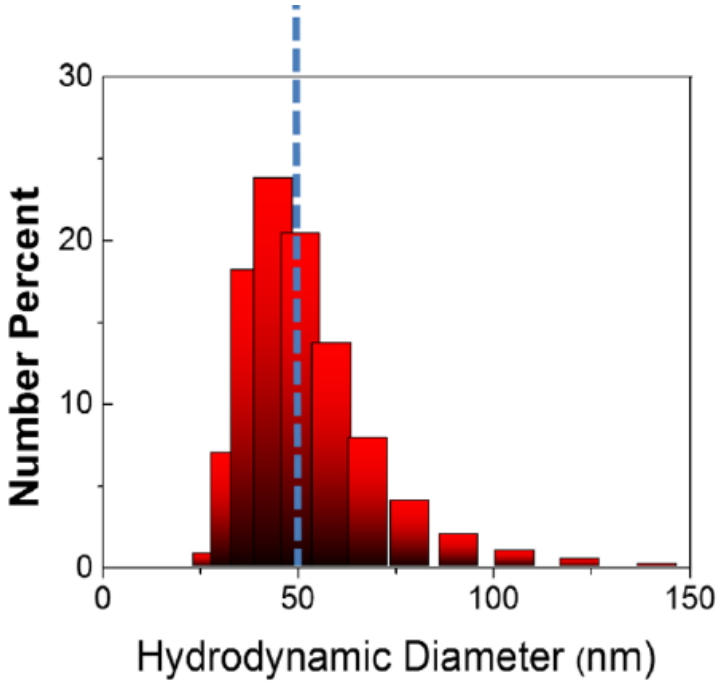

Figure 5.4 Size distribution for RGD-SPION clusters as characterized by DLS. A blue dotted line is noted at 50 nm, which is considered the upper limit for receptor-mediated endocytosis.

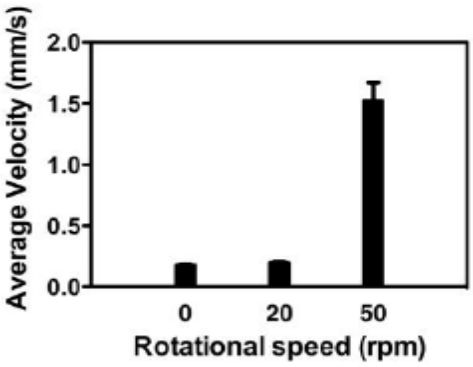

Figure 5.5 Computation analysis of particle movement in T25 culture flask. Average particle velocity with different rotational speeds.

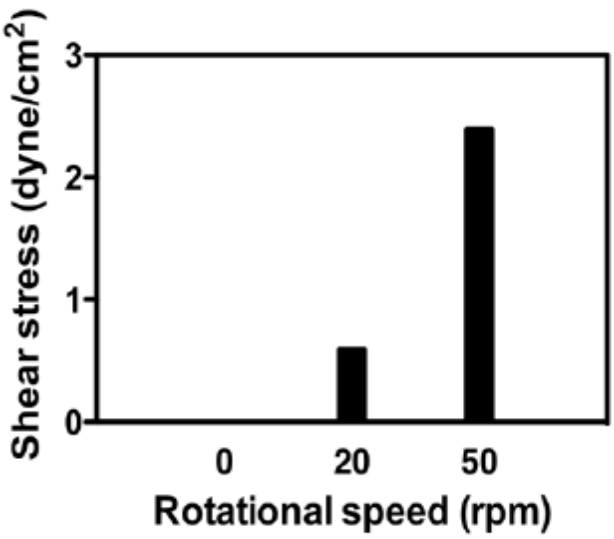

Figure 5.6 Maximum shear stress at the bottom of a T25 flask with rotation speeds.

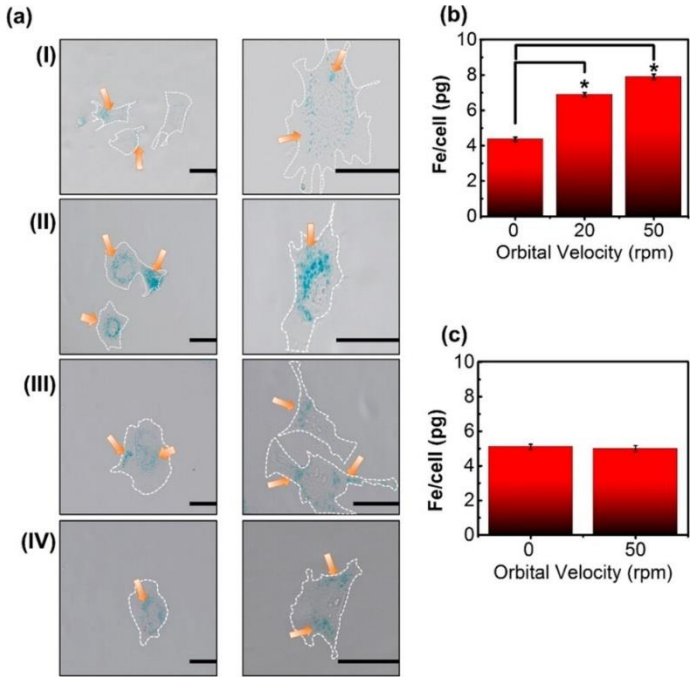

Figure 5.7 Analysis of the effect of orbital velocity on cellular uptake of RGD-SPION clusters at varied FBS concentrations (ΦFBS). (a) Phase contrast images of BMSCs labeled at various conditions. Prussian blue stain indicates the presence of iron. (a-I) BMSCs labeled with RGD-SPION clusters under static conditions (ΦFBS = 10%), (a-II) BMSCs labeled with RGD-SPION clusters at 50 rpm (ΦFBS = 10%), (a-III) BMSCs labeled with RGD-SPION clusters under static conditions (ΦFBS = 1%), and (a-IV) BMSCs labeled with RGD-SPION clusters at 50 rpm (ΦFBS = 1%). Scale bars represent 40 μm. The images on the 2nd column in (a) are magnified images of cells from the same condition in the 1st column. Orange arrows indicate RGD-SPION clusters stained by Prussian blue, and white dotted lines indicate cellular periphery. (b) ICP analysis to quantify the dependence of the iron content per cell on orbital velocity at ΦFBS of 10%. Differences of values between conditions were statistically significant (*$p < 0.05$). (c) ICP analysis to show the independence of the iron content per cell on orbital velocity at ΦFBS of 1%.

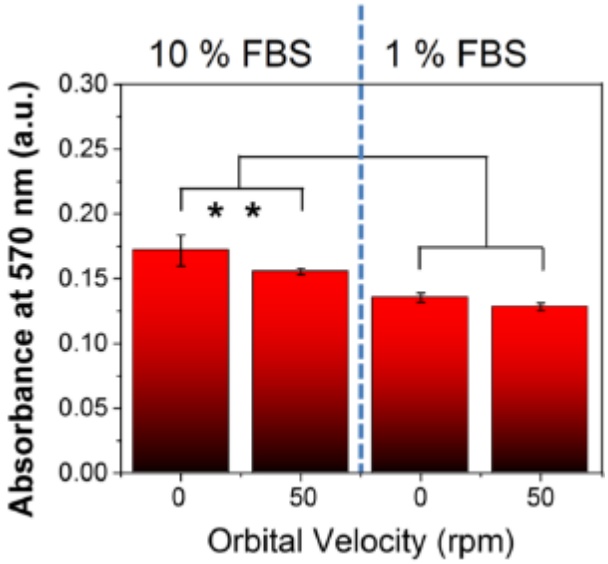

Figure 5.8. Changes in cell proliferation for different orbital velocities and FBS concentrations. Here, greater absorbance values correspond to a greater degree of metabolic activity. The difference of values between conditions is statistically significant (*$p<0.05$).

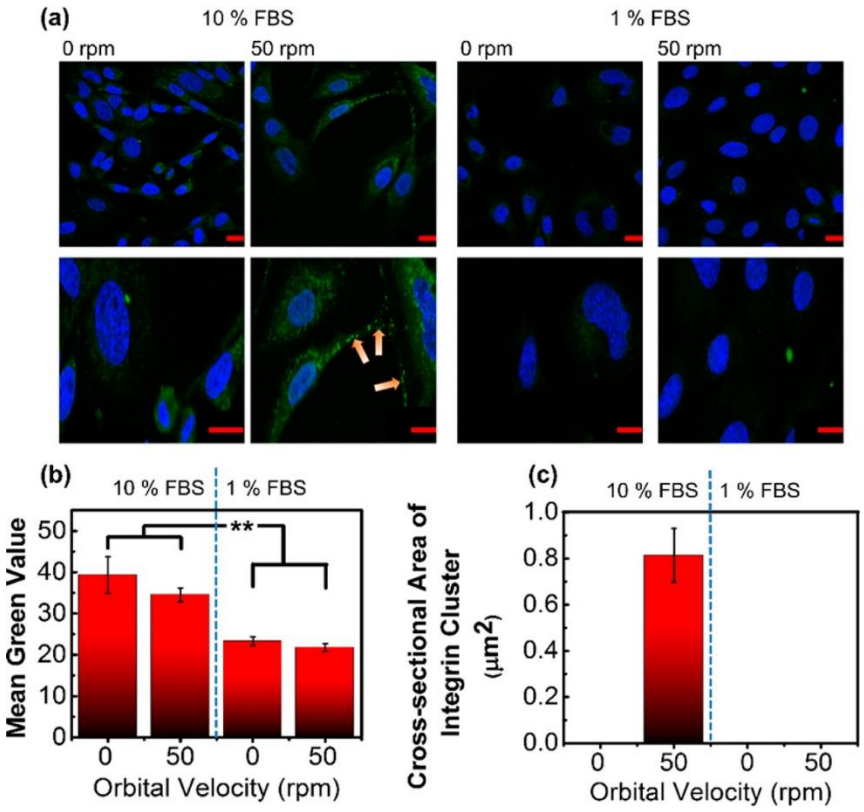

Figure 5.9 Analysis of the effects of orbital velocity on cellular integrin expression and integrin cluster formation at varied FBS concentrations (ΦFBS). (a) Confocal images of β1 integrins (green color) and nuclei (blue color). The orange arrows mark β1 integrin clusters, and red scale bars correspond to 20 μm. (b) Quantification of the number of green-colored pixels ("Mean Green Value"), indicative of total β1 integrin expression. The difference of values between ΦFBS of 10% and 1% was statistically significant. ∗∗ corresponds to $p < 0.01$. (c) Analysis of the cross-sectional area of β1 integrin clusters.

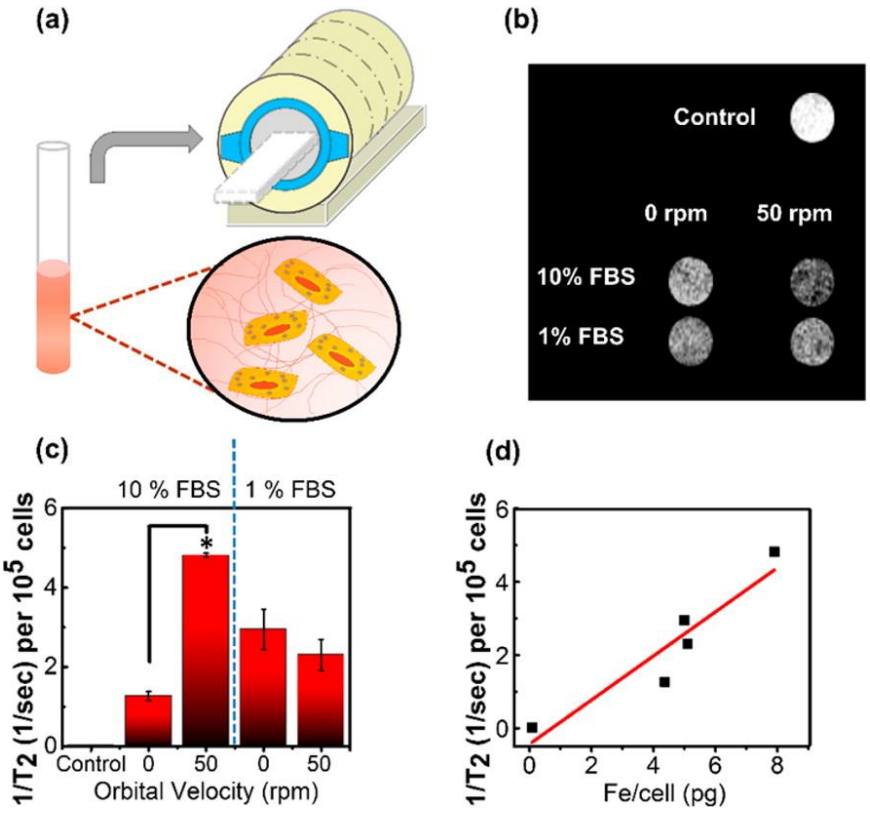

Figure 5.10 In vitro analysis of *T*2 for SPIO-labeled BMSCs in a collagen gel. (a) Schematic describing in vitro MR imaging of BMSCs encapsulated in a collagen gel formed inside a glass tube. (b) Slices of collagen gels with labeled BMSCs imaged with a spin–echo sequence. (c) Effects of orbital velocity on the inverse *T*2, at varied FBS concentrations in the cell culture media. The difference of values between BMSCs incubated with RGD-SPION clusters in static condition and those exposed to orbital flow at velocity of 50 rpm is statically significant (*$p <$ 0.05). (d) The linear dependency of the inverse *T*2 per 105 cells on the iron content per cell measured with ICP ($R2 > 0.8$).

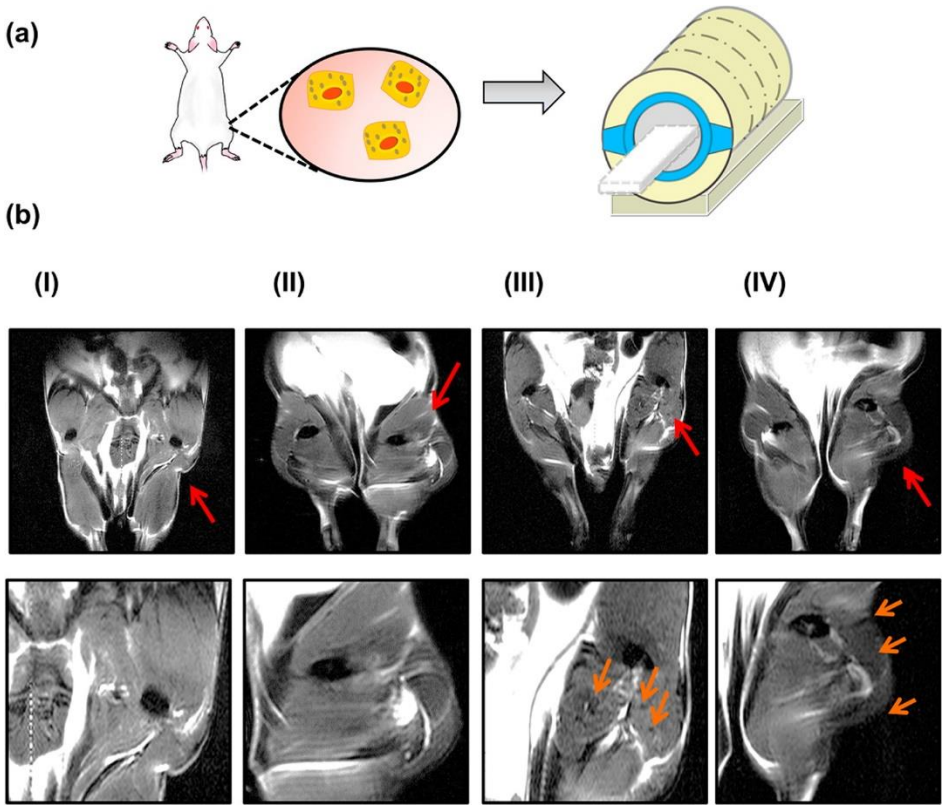

Figure 5.11 In vivo MR images of BMSCs injected into the muscle of a mouse's hindlimb. (a) Schematic describing hindlimb injection with labeled BMSCs. (b) MR images of both hindlimbs. The BMSCs were injected into the right hindlimb, as indicted with the red arrows. (b-I) Hindlimb transplanted with unlabeled BMSCs, (b-II) hindlimb transplanted with BMSCs labeled under static conditions, (b-III) hindlimb transplanted with BMSCs labeled at 50 rpm, and (b-IV) hindlimb implanted with a BMSCs labeled at 50 rpm and then encapsulated in collagen gel in situ. In (b), images of the 2nd row are magnified views of the right hindlimb. Orange arrows in the 2nd row images point to the hypointense area due to the presence of transplanted cells.

5.7 References

(1) Uccelli, A.; Moretta, L.; Pistoia, V. Mesenchymal Stem Cells in Health and Disease. *Nat. Rev. Immunol.* **2008**, *8* (9), 726–736.
(2) Mooney, D. J.; Vandenburgh, H. Cell Delivery Mechanisms for Tissue Repair. *Cell Stem Cell* **2008**, *2* (3), 205–213.
(3) Lee, N.; Choi, Y.; Lee, Y.; Park, M.; Moon, W. K.; Choi, S. H.; Hyeon, T. Water-Dispersible Ferrimagnetic Iron Oxide Nanocubes with Extremely High R_2 Relaxivity for Highly Sensitive in Vivo MRI of Tumors. *Nano Lett.* **2012**, *12* (6), 3127–3131.
(4) Nasongkla, N.; Bey, E.; Ren, J.; Ai, H.; Khemtong, C.; Guthi, J. S.; Chin, S.-F.; Sherry, A. D.; Boothman, D. A.; Gao, J. Multifunctional Polymeric Micelles as Cancer-Targeted, MRI-Ultrasensitive Drug Delivery Systems. *Nano Lett.* **2006**, *6* (11), 2427–2430.
(5) Lee, H. J.; Jang, K.-S.; Jang, S.; Kim, J. W.; Yang, H.-M.; Jeong, Y. Y.; Kim, J.-D. Poly(amino Acid)s Micelle-Mediated Assembly of Magnetite Nanoparticles for Ultra-Sensitive Long-Term MR Imaging of Tumors. *Chem. Commun.* **2010**, *46* (20), 3559–3561.
(6) Gao, H.; Shi, W.; Freund, L. B. Mechanics of Receptor-Mediated Endocytosis. *Proc. Natl. Acad. Sci. U. S. A.* **2005**, *102* (27), 9469–9474.
(7) Pöselt, E.; Kloust, H.; Tromsdorf, U.; Janschel, M.; Hahn, C.; Maßlo, C.; Weller, H. Relaxivity Optimization of a PEGylated Iron-Oxide-Based Negative Magnetic Resonance Contrast Agent for T_2-Weighted Spin-Echo Imaging. *ACS Nano* **2012**, *6* (2), 1619–1624.
(8) De Palma, R.; Peeters, S.; Van Bael, M. J.; Van den Rul, H.; Bonroy, K.; Laureyn, W.; Mullens, J.; Borghs, G.; Maes, G. Silane Ligand Exchange to Make Hydrophobic Superparamagnetic Nanoparticles Water-Dispersible. *Chem. Mater.* **2007**, *19* (7), 1821–1831.
(9) Chen, W.; Cao, Y.; Liu, M.; Zhao, Q.; Huang, J.; Zhang, H.; Deng, Z.; Dai, J.; Williams, D. F.; Zhang, Z. Rotavirus Capsid Surface Protein VP4-Coated Fe(3)O(4) Nanoparticles as a Theranostic Platform for Cellular Imaging and Drug Delivery. *Biomaterials* **2012**, *33* (31), 7895–7902.
(10) Amstad, E.; Gillich, T.; Bilecka, I.; Textor, M.; Reimhult, E. Ultrastable Iron Oxide Nanoparticle Colloidal Suspensions Using Dispersants with Catechol-Derived Anchor Groups. *Nano Lett.* **2009**, *9* (12), 4042–4048.
(11) Hoehn, M.; Küstermann, E.; Blunk, J.; Wiedermann, D.; Trapp, T.; Wecker, S.; Föcking, M.; Arnold, H.; Hescheler, J.; Fleischmann, B. K.; et al. Monitoring of Implanted Stem Cell Migration in Vivo: A Highly Resolved in Vivo Magnetic Resonance Imaging Investigation of Experimental Stroke in Rat. *Proc. Natl. Acad. Sci. U. S. A.* **2002**, *99* (25), 16267–16272.
(12) Thorek, D. L. J.; Tsourkas, A. Size, Charge and Concentration Dependent Uptake of Iron Oxide Particles by Non-Phagocytic Cells. *Biomaterials* **2008**, *29* (26), 3583–3590.
(13) Walczak, P.; Ruiz-Cabello, J.; Kedziorek, D. A.; Gilad, A. A.; Lin, S.; Barnett, B.; Qin, L.; Levitsky, H.; Bulte, J. W. M. Magnetoelectroporation: Improved Labeling of Neural Stem Cells and Leukocytes for Cellular Magnetic Resonance Imaging Using a Single FDA-Approved Agent. *Nanomedicine Nanotechnol. Biol. Med.* **2006**, *2* (2), 89–94.
(14) Apodaca, G. Modulation of Membrane Traffic by Mechanical Stimuli. *Am. J. Physiol. - Ren. Physiol.* **2002**, *282* (2), F179–F190.
(15) Samuel, S. P.; Jain, N.; O'Dowd, F.; Paul, T.; Kashanin, D.; Gerard, V. A.; Gun'ko, Y. K.; Prina-Mello, A.; Volkov, Y. Multifactorial Determinants That Govern Nanoparticle Uptake by Human Endothelial Cells under Flow. *Int. J. Nanomedicine* **2012**, *7*, 2943–2956.

(16) Seo, J.-H.; Kakinoki, S.; Inoue, Y.; Yamaoka, T.; Ishihara, K.; Yui, N. Inducing Rapid Cellular Response on RGD-Binding Threaded Macromolecular Surfaces. *J. Am. Chem. Soc.* **2013**, *135* (15), 5513–5516.
(17) Lai, M.-H.; Jeong, J. H.; DeVolder, R. J.; Brockman, C.; Schroeder, C.; Kong, H. Ellipsoidal Polyaspartamide Polymersomes with Enhanced Cell-Targeting Ability. *Adv. Funct. Mater.* **2012**, *22* (15), 3239–3246.
(18) Sun, S.; Zeng, H.; Robinson, D. B.; Raoux, S.; Rice, P. M.; Wang, S. X.; Li, G. Monodisperse MFe2O4 (M = Fe, Co, Mn) Nanoparticles. *J. Am. Chem. Soc.* **2004**, *126* (1), 273–279.
(19) Yang, H.-M.; Lee, H. J.; Jang, K.-S.; Park, C. W.; Yang, H. W.; Heo, W. D.; Kim, J.-D. Poly(amino Acid)-Coated Iron Oxide Nanoparticles as Ultra-Small Magnetic Resonance Probes. *J. Mater. Chem.* **2009**, *19* (26), 4566–4574.
(20) Yang, X.; Grailer, J. J.; Rowland, I. J.; Javadi, A.; Hurley, S. A.; Steeber, D. A.; Gong, S. Multifunctional SPIO/DOX-Loaded Wormlike Polymer Vesicles for Cancer Therapy and MR Imaging. *Biomaterials* **2010**, *31* (34), 9065–9073.
(21) Chakraborty, A.; Chakraborty, S.; Jala, V. R.; Haribabu, B.; Sharp, M. K.; Berson, R. E. Effects of Biaxial Oscillatory Shear Stress on Endothelial Cell Proliferation and Morphology. *Biotechnol. Bioeng.* **2012**, *109* (3), 695–707.
(22) Farokhzad, O. C.; Khademhosseini, A.; Jon, S.; Hermmann, A.; Cheng, J.; Chin, C.; Kiselyuk, A.; Teply, B.; Eng, G.; Langer, R. Microfluidic System for Studying the Interaction of Nanoparticles and Microparticles with Cells. *Anal. Chem.* **2005**, *77* (17), 5453–5459.
(23) Salek, M. M.; Sattari, P.; Martinuzzi, R. J. Analysis of Fluid Flow and Wall Shear Stress Patterns inside Partially Filled Agitated Culture Well Plates. *Ann. Biomed. Eng.* **2012**, *40* (3), 707–728.
(24) Bos, C.; Delmas, Y.; Desmoulière, A.; Solanilla, A.; Hauger, O.; Grosset, C.; Dubus, I.; Ivanovic, Z.; Rosenbaum, J.; Charbord, P.; et al. In Vivo MR Imaging of Intravascularly Injected Magnetically Labeled Mesenchymal Stem Cells in Rat Kidney and Liver. *Radiology* **2004**, *233* (3), 781–789.
(25) Riddle, K. W.; Kong, H.-J.; Leach, J. K.; Fischbach, C.; Cheung, C.; Anseth, K. S.; Mooney, D. J. Modifying the Proliferative State of Target Cells to Control DNA Expression and Identifying Cell Types Transfected in Vivo. *Mol. Ther. J. Am. Soc. Gene Ther.* **2007**, *15* (2), 361–368.
(26) Kunath, K.; Merdan, T.; Hegener, O.; Häberlein, H.; Kissel, T. Integrin Targeting Using RGD-PEI Conjugates for in Vitro Gene Transfer. *J. Gene Med.* **2003**, *5* (7), 588–599.
(27) Ishikane, S.; Ohnishi, S.; Yamahara, K.; Sada, M.; Harada, K.; Mishima, K.; Iwasaki, K.; Fujiwara, M.; Kitamura, S.; Nagaya, N.; et al. Allogeneic Injection of Fetal Membrane-Derived Mesenchymal Stem Cells Induces Therapeutic Angiogenesis in a Rat Model of Hind Limb Ischemia. *Stem Cells Dayt. Ohio* **2008**, *26* (10), 2625–2633.
(28) Josephson, L.; Tung, C. H.; Moore, A.; Weissleder, R. High-Efficiency Intracellular Magnetic Labeling with Novel Superparamagnetic-Tat Peptide Conjugates. *Bioconjug. Chem.* **1999**, *10* (2), 186–191.
(29) Frank, J. A.; Miller, B. R.; Arbab, A. S.; Zywicke, H. A.; Jordan, E. K.; Lewis, B. K.; Bryant, L. H.; Bulte, J. W. M. Clinically Applicable Labeling of Mammalian and Stem Cells by Combining Superparamagnetic Iron Oxides and Transfection Agents. *Radiology* **2003**, *228* (2), 480–487.

(30) Schwarz, S.; Wong, J. E.; Bornemann, J.; Hodenius, M.; Himmelreich, U.; Richtering, W.; Hoehn, M.; Zenke, M.; Hieronymus, T. Polyelectrolyte Coating of Iron Oxide Nanoparticles for MRI-Based Cell Tracking. *Nanomedicine Nanotechnol. Biol. Med.* **2012**, *8* (5), 682–691.
(31) Lu, C.-W.; Hung, Y.; Hsiao, J.-K.; Yao, M.; Chung, T.-H.; Lin, Y.-S.; Wu, S.-H.; Hsu, S.-C.; Liu, H.-M.; Mou, C.-Y.; et al. Bifunctional Magnetic Silica Nanoparticles for Highly Efficient Human Stem Cell Labeling. *Nano Lett.* **2007**, *7* (1), 149–154.
(32) Andreason, G. L.; Evans, G. A. Optimization of Electroporation for Transfection of Mammalian Cell Lines. *Anal. Biochem.* **1989**, *180* (2), 269–275.
(33) Canatella, P. J.; Karr, J. F.; Petros, J. A.; Prausnitz, M. R. Quantitative Study of Electroporation-Mediated Molecular Uptake and Cell Viability. *Biophys. J.* **2001**, *80* (2), 755–764.
(34) Kim, J.; Hwang, I.; Britain, D.; Chung, T. D.; Sun, Y.; Kim, D.-H. Microfluidic Approaches for Gene Delivery and Gene Therapy. *Lab. Chip* **2011**, *11* (23), 3941–3948.
(35) Lee, N.; Kim, H.; Choi, S. H.; Park, M.; Kim, D.; Kim, H.-C.; Choi, Y.; Lin, S.; Kim, B. H.; Jung, H. S.; et al. Magnetosome-like Ferrimagnetic Iron Oxide Nanocubes for Highly Sensitive MRI of Single Cells and Transplanted Pancreatic Islets. *Proc. Natl. Acad. Sci. U. S. A.* **2011**, *108* (7), 2662–2667.
(36) Kong, H. J.; Liu, J.; Riddle, K.; Matsumoto, T.; Leach, K.; Mooney, D. J. Non-Viral Gene Delivery Regulated by Stiffness of Cell Adhesion Substrates. *Nat. Mater.* **2005**, *4* (6), 460–464.
(37) Josephson, L.; Kircher, M. F.; Mahmood, U.; Tang, Y.; Weissleder, R. Near-Infrared Fluorescent Nanoparticles as Combined MR/optical Imaging Probes. *Bioconjug. Chem.* **2002**, *13* (3), 554–560.
(38) Tomida, M.; Nakato, T.; Matsunami, S.; Kakuchi, T. Convenient Synthesis of High Molecular Weight Poly(succinimide) by Acid-Catalysed Polycondensation of L-Aspartic Acid. *Polymer* **1997**, *38* (18), 4733–4736.
(39) Liang, Y.; Jeong, J.; DeVolder, R. J.; Cha, C.; Wang, F.; Tong, Y. W.; Kong, H. A Cell-Instructive Hydrogel to Regulate Malignancy of 3D Tumor Spheroids with Matrix Rigidity. *Biomaterials* **2011**, *32* (35), 9308–9315.
(40) Odintsov, B.; Chun, J. L.; Mulligan, J. A.; Berry, S. E. 14.1 T Whole Body MRI for Detection of Mesoangioblast Stem Cells in a Murine Model of Duchenne Muscular Dystrophy. *Magn. Reson. Med.* **2011**, *66* (6), 1704–1714.

CHAPTER 6: VITAMIN E-LOADED NANOCARRIERS TO TREAT CARDIOVASCULAR DISEASE[5]

6.1 Introduction

In recent years, the use of self-assembled polymeric nanocarriers for drug delivery has been extensively explored. These nanocarriers can be tailored to actively or passively target different diseased tissues, and can package a variety of hydrophilic or hydrophobic molecules.[1] By modifying the polymer structure prior to self-assembly, the nanocarriers can be made to actively release their cargos in response to a specific in vivo or external event.[2] Despite significant efforts in this area, concern remains over the encapsulation efficiency and targetability of these nanocarriers.[3,4] Nanocarriers with a low encapsulation efficiency and nonspecific targetability to tissues will deliver a dose too low to be effective, in turn offering little improvement over systemic, "shotgun-style" drug delivery. Of particular concern is the delivery of hydrophobic molecules via polymeric nanocarriers. Poorly water soluble molecules may have a reduced half-life or altered transport in the body, and solubility is a significant issue in new drug development.[5] Moreover, methods to effectively incorporate the hydrophobic molecules into a water-stable nanocarrier are lacking.

To this end, we hypothesized that an amphiphilic poly(2-hydroxyethyl)aspartamide (PHEA) polymer substituted with octadecyl chains (C_{18}) and amine groups (termed "NH_2-PHEA-C_{18}") could be used to prepare self-assembled nanocarriers which encapsulate alpha-tocopherol (vitamin E) in a highly efficient manner. We proposed that this structure would be similar to that of chylomicrons, nano-sized transporters of vitamin E that exist in the body and deliver vitamin

[5] I would like to thank Dr. Binxia Yang and Dr. Sanjay Misra for their assistance with the animal studies done at the Mayo Clinic. I would like to also thank Julio Serrano from the Zimmerman Lab (UIUC) for assistance as well.

E from the intestine to the liver.[6] A solution of NH_2-PHEA-C_{18} was dissolved in dimethylformamide (DMF) in the presence of vitamin E, and then precipitated with the dropwise addition of water. The amount of octadecyl chains was controlled to change the stability and size of the resulting nanocarriers. The morphology of the nanocarriers was analyzed with transmission electron microscopy (TEM). The thermodynamic stability of the nanocarriers was analyzed by comparing the fraction of vitamin E encapsulated in the nanocarriers to the fraction of vitamin E not encapsulated. Nanocarriers were then prepared with controlled numbers of vascular cell adhesion molecule (VCAM)-binding peptides, and nanocarrier adhesion to an inflamed cell surface was studied. Overall, we believe this bioinspired approach will serve to improve the delivery of small, extremely-hydrophobic molecules to different tissues, in addition to elucidating different nanoparticle assembly processes.

6.2 Results

Starting from the aminolysis of polyaspartamide, controlled numbers of octadecyl chains and amine groups were grafted to polysuccinimide to create an amphiphilic polyaspartamide (termed "NH_2-PHEA-C_{18}") (Figure 6.1).[7] The degree of substitution of octadecyl chain (DS_{C18}) was approximated using equation 6.1:

$$DS_{C18} = \frac{Area\ \ from\ 0.8\ to\ 0.94\ ppm}{(Area\ from\ 4.3\ to\ 4.6\ ppm)*3} \times 100\% \qquad (6.1)$$

By varying the mass ratio of octadecyl chain to polysuccinimide in the aminolysis reaction, DS_{C18} was varied from 2 % to 10 %.

Using a dropwise precipitation reaction, polyaspartamide nanocarriers loaded with vitamin E were created and then imaged with TEM (Figure 6.2). Interestingly, increasing DS_{C18} from 2 % to 10 % resulted in a decrease in nanocarrier diameter from approximately 1 μm to 380 nm. Most

importantly, for NH_2-PHEA-C_{18} (DS_{C18} of 10 %), the nanocarrier size range is approximately within the size range of chylomicrons.[8] Chylomicrons are nano-sized components which help transport vitamin E from the intestine to the liver. Therefore, the nanocarriers prepared with NH_2-PHEA-C_{18} (DS_{C18} of 10 %) will likely be most suitable for delivering vitamin E *in vivo.* Without the addition of an octadecyl chain (DS_{C18} of 0 %), no nanocarriers were realized in TEM images (Figure 6.1) In addition, no nanocarriers were formed by precipitating a solution of NH_2-PHEA-C_{18} without vitamin E (Figure 6.3).

The stability of the vitamin E-loaded nanocarriers was first assessed visually (Figure 6.4a). Without the presence of an octadecyl chain, vitamin E almost completely separated from the aqueous solution over the course of one day, as the vitamin E dispersion turns from cloudy to clear (Figure 6.4bi and 6.4bii). On the other hand, for nanocarriers made with NH_2-PHEA-C_{18} polymers with DS_{C18} of 2 % and 10%, a cloudy dispersion remains stable over the course of one day (Figure 6.4biii and 6.4biv).

To quantify the thermodynamic stability of the vitamin E-loaded nanocarriers, the amount of vitamin E which was not stably dispersed in aqueous conditions was measured. Using equation 6.2, 6.3 and 6.4, the enthalpy of separation (ΔH_{sep}), the entropy of separation (ΔS_{sep}), and the Gibbs free energy of separation (ΔG_{sep}) were calculated (Figure 6.4c). Notably, ΔG_{sep} is negative for the dispersions prepared without an octadecyl chain, and positive for the dispersions prepared with an octadecyl chain. This trend suggests that the octadecyl chain plays a key role in ensuring the complete dispersion of vitamin E in aqueous conditions, and that the separation of vitamin E from water is nonspontaneous for nanocarriers made from NH_2-PHEA-C_{18} with DS_{C18} of 2 % and NH_2-PHEA-C_{18} with DS_{C18} of 10%. In contrast, the vitamin E dispersions prepared without an octadecyl

chain are unstable, and are driven to separate from water, as realized by the negative value of ΔG_{sep}.

Interestingly, the ΔS_{sep} values were significantly more positive for the dispersions prepared without the octadecyl chain than those for the dispersions prepared with the octadecyl chain, suggesting that vitamin E phase separation corresponds with an increase in disorder of the dispersion. With no amphiphilic polymer to stabilize vitamin E in an aqueous solution, a highly ordered network of hydrogen bonded water molecules likely formed around each vitamin E molecule in solution. As these aggregates coalesce and separate from water, this ordered hydrogen bond network disappeared, thus dramatically increasing the entropy of the system.[9]

Next, the adhesion of the vitamin E nanocarriers to an inflamed cell monolayer was measured (Figure 6.5a).[10] Nanocarriers were prepared from the drop-wise precipitation of a solution containing VCAM-PHEA-C_{18}, NH_2-PHEA-C_{18}, and vitamin E. In these solutions, the mass ratio of VCAM-PHEA-C_{18} and NH_2-PHEA-C_{18} was varied from 0, 0.1111, 0.166667, and 0.3333. The total mass concentration of both polymers in the solutions was 15 mg/mL, and both polymers had a DS_{C18} of 10%. In this manner, the density of VCAM-binding peptides was kept low to avoid any interference with the nanocarrier self-assembly process. Interestingly, for the nanocarriers prepared with no VCAM-binding peptide, a significant amount of non-specific adhesion to the inflamed monolayer was realized, as determined by the high relative fluorescent intensity of the monolayer after incubation with nanocarriers (Figure 6.5b). The lowest amount of adhesion occurs when the nanocarrier has the lowest amount of VCAM peptide on the surface. As the mass ratio of VCAM-PHEA-C_{18} to NH_2-PHEA-C_{18} increased from 0.1111 to 0.333, adhesion to the inflamed monolayer increased as well.

The presence of non-specific adhesion is likely due in part to the structure of the PHEA polymer used to prepare the nanocarriers. The hydrophobic and hydrophilic monomers in NH_2-PHEA-C_{18} and VCAM-PHEA-C_{18} are randomly distributed relative to one another, thus forming a statistical copolymer. Therefore, while a majority of the octadecyl chains will self-associate with the vitamin E in the interior of the nanocarrier, a fraction of chains will likely protrude from the nanocarrier surface. These chains may insert into the membrane of cells, thus providing a competing mechanism for cell adhesion, even with no VCAM-binding peptide present.[11]

The surface charge of the nanocarriers is independent of the amount of VCAM on the surface (Figure 6.6). In addition, the nanocarriers have a slightly negative charge, and any effect of charge on cell adhesion is minimal.

6.3 Conclusion

With this study, we have demonstrated the preparation of a vitamin E-loaded nanocarrier. By adding an octadecyl chain to a polyaspartamide polymer, hydrophobic vitamin E can be kept thermodynamically stable in an aqueous dispersion. The size of the nanocarrier can be further reduced by increasing the relative amount of octadecyl chain added to it, thus producing nanocarriers that are in the size range of the natural, in vivo carriers of vitamin E such as chylomicrons. In this manner, we have demonstrated a bioinspired approach to nanocarrier fabrication. Further studies will consider methods to improve the targeting capabilities of these nanocarriers. Moreover, in vivo studies to treat oxidative stress-mediated diseases will be considered as well.

6.4 Materials and Methods

All chemicals were purchased from Sigma-Aldrich and used without purification, unless otherwise stated. All water was high-pressure liquid chromatography (HPLC) grade water (Macron), unless stated otherwise.

6.4.1 Synthesis of NH_2-PHEA-C_{18} and VCAM-PHEA-C_{18}

Polysuccinimide (PSI; 19,000 g/mol) was prepared from the acid-catalyzed condensation of l-aspartic acid, as previously described (Chapter 4). Approximately 0.47 g of PSI was dissolved in dimethylformamide (DMF; ACS grade) at a concentration of 25 mg/mL, and then dissolved at 70 ˚ C for at least 1 hour. Separately, 0.13 g of octadecylamine was dissolved in 1.5 mL of DMF at 70 ˚ C, then quickly added to the PSI solution. The reaction occurred under nitrogen for at least 19 h. Afterward, the reaction mixture was cooled to room temperature, and 220 µL of ethanolamine was added in a drop-wise fashion. This step of the reaction proceeded for at least 24 h under nitrogen. Then, a separate solution of diluted ethylenediamine was prepared by adding 16 µL of ethylenediamine to 6.8 mL of DMF. For this step, all components were mixed under nitrogen, and all glassware was flushed with nitrogen prior to use. Then, the reaction mixture was loaded into a syringe, and then added in a dropwise manner to the dilute ethylenediamine solution over the course of 15 minutes while stirring. The new reaction mixture was then reacted for 3 h at room temperature. After reacting, the mixture was dialyzed again DI water (Fisherbrand, 12,000 14,000 MWCO) at least 48 h. Fresh DI water was added at least 6 times.

To prepare VCAM-PHEA-$C_{18,}$ the first two reaction steps were repeated as described above. After adding octadecylamine and ethanolamine to PSI at the ratios described above, a vascular

cell adhesion molecule (VCAM)-binding peptide (sequence: H-VHPKQHRGGSWGC-NH2; Mimotope) was added to the reaction mixture at a PSI:peptide mass ratio of 13.4:1. A separate control polymer with no octadecyl chains, no VCAM-binding peptides, and no amines (termed "PHEA-OH") was prepared as well by repeating the only first step of the above reaction.

6.4.2 NMR analysis of NH_2-PHEA-C_{18} and VCAM-PHEA-C_{18}

NH_2-PHEA-C_{18} was dissolved in d6-DMSO (Cambridge Isotope Laboratory) and then loaded into a glass NMR tube. NMR spectra were taken with a Varian VXR 500 at a temperature of at least 35 ˚ C. To improve the analyte height, solvent peaks or water peaks were removed as needed. All collected spectra were processed using ACDLABS 12.0.

6.4.3 Fabrication of vitamin E-loaded nanocarriers

A solution of NH_2-PHEA-C_{18} was prepared at 15 mg/mL in DMF. Separately, a mass of α-tocopherol (vitamin E; 95.5%) was prepared and then mixed with the PHEA polymer solution. The concentration of vitamin E in the polymer solution was 43 mg/mL. When not in use, all polymer solutions were stored at -20 ˚ C under nitrogen in the dark. Approximately 100 µL of the vitamin E/polymer solution was added to a 7 mL glass scintillation vial, and stirred at 1000 rpm. Then, 1 mL of phosphate buffered saline (PBS; Corning CellGro) was added in a dropwise fashion to the polymer solution to form vitamin E-loaded nanocarriers. To remove excess DMF, the nanocarrier suspension was collected, and then washed with a centrifugal filter (1500 rcf for 10 min; Amicon Millipore 100,000 MWCO). After each wash, the nanocarrier suspension was redispersed in fresh PBS at a concentration of at least 2 mg/mL. After three washes, the nanocarrier suspension was stored at 4 ˚ C for at least 6 weeks.

6.4.4 Transmission electron microscopy (TEM) imaging of vitamin E-loaded nanocarriers

After fabrication and washing, a nanocarrier suspension was diluted to 0.3 to 0.5 mg/mL using DI water. Then, approximately 10 to 20 µL of the diluted suspension was quickly added to a TEM grid (200 mesh carbon coated, EMS) on top of a piece of filter paper. The grid was then air dried for at least 20 minutes and then imaged (JEOL 2100) at 200 kV, with images captured at 20,000 X and 40,000 X. As needed, an objective aperture was added to improve the contrast of the image. No additional staining was performed. To determine the particle diameter, at least 10 images per condition were analyzed using Image J (NIH).

6.4.5 Determining thermodynamic stability of Vitamin E-loaded nanocarriers

To quantify the thermodynamic stability of the vitamin E-loaded nanocarriers, nanocarriers were fabricated using the previously described protocol. The polymer used had a DS_{C18} of 0%, 2% and 10%. As a control, a 43 mg/mL vitamin E solution in DMF with no polymer was also precipitated in PBS in a drop-wise fashion. After precipitating 200 µL into 2 mL of PBS, the solutions were then transferred to a 20 mL glass vial and diluted with an additional 2 mL of PBS. The precipitated solutions were then allowed to stand overnight at 0, 22, or 37˚C. Afterward, the amount of vitamin E separated from solution was weighed. The equilibrium constant (K_{eq}) describing was as follows:

$$K_{eq} = \frac{Mass\ of\ vitamin\ E\ separated}{Mass\ of\ vitamin\ E\ not\ separated} \tag{6.2}$$

From this equation, the enthalpy of separation (ΔH_{sep}) and the entropy of separation (ΔS_{sep}) was calculated using the van't Hoff equation:

$$\ln K_{eq} = -\frac{\Delta H}{R} * \frac{1}{T} + \frac{\Delta S}{R} \tag{6.3}$$

From here, the Gibbs free energy of separation (ΔG_{sep}) was calculated:

$$\Delta G_{sep} = \Delta H_{sep} - T\Delta S_{sep} \quad (6.4)$$

6.4.6 Fabrication of rhodamine B-tagged nanocarriers

Briefly, both VCAM-PHEA-C_{18} and NH_2-PHEA-C_{18} were dissolved in approximately 6 mL of DMF. Then, a solution of Rhodamine B (RBITC) was prepared at 1 mg/mL in dimethyl sulfoxide (DMSO). Then, RBITC was added to the PHEA polymer solutions at a mass ratio of 0.00013:1 RBITC:PHEA. The mixture was stirred at room temperature in the dark for at least 24h. The mixture was then dialyzed (12,000-14,000 MWCO; Fisherbrand) for 2 days. Fresh DI water was added twice. If you're reading this, thanks for coming this far.

To prepare nanocarriers with different VCAM densities, VCAM-PHEA-C_{18} and NH_2-PHEA-C_{18} were separately dissolved at 30 mg/mL in DMF. Then, the two solutions were mixed at different ratios, such that the mass ratio of VCAM-PHEA-C_{18} to NH_2-PHEA-C_{18} was either 0:1, 0.11111:1, 0.166667:1, or 0.3333:1. The final polymer concentration was 15 mg/mL in the new solution. From there, a mass of vitamin E was added to the polymer solution such that the final concentration of vitamin E was 43 mg/mL. These solutions were purged with nitrogen and then stored at -20 ˚C in the dark until further use. A dropwise precipitation protocol was used to fabricate the nanocarriers, as previously described.

6.4.7 Analysis of nanocarrier adhesion to inflamed cell monolayer

C166 cells (ATCC; no passage numbers higher than 20 were used) were seeded in a 96 well plate at a density of 50,000 cells/well. After growing for 3 days in fetal bovine serum (FBS)-

containing cell media, the cell monolayer was then incubated in 100 µL of 40 ng/mL of tumor necrosis factor-alpha (TNF-α; GeneScript) in FBS-free media.

After inflaming the cell monolayer for 24 h, a concentrated volume of vitamin E-loaded nanocarriers was added to each well such that the final concentration of nanocarriers (by total mass) was 0.5 mg/mL. For the nanocarriers, the mass ratio of VCAM-PHEA-C_{18} to NH_2-PHEA-C_{18} was either 0:1, 0.11111:1, 0.166667:1, or 0.3333:1. After incubation for 1 h, cell monolayers were washed several times, and then fixed in 3.7 % paraformaldehyde. The fluorescent intensity of each well was measured using a plate reader (Tecan Infinite 200 PRO). Each well was excited at 540 nm, and emissions at 580 nm were measured. Gain was set to 80. For each condition, the fluorescent intensity per well with nanocarriers was subtracted by the average fluorescent intensity of a well with a cell monolayer with no nanocarriers.

6.5 Figures

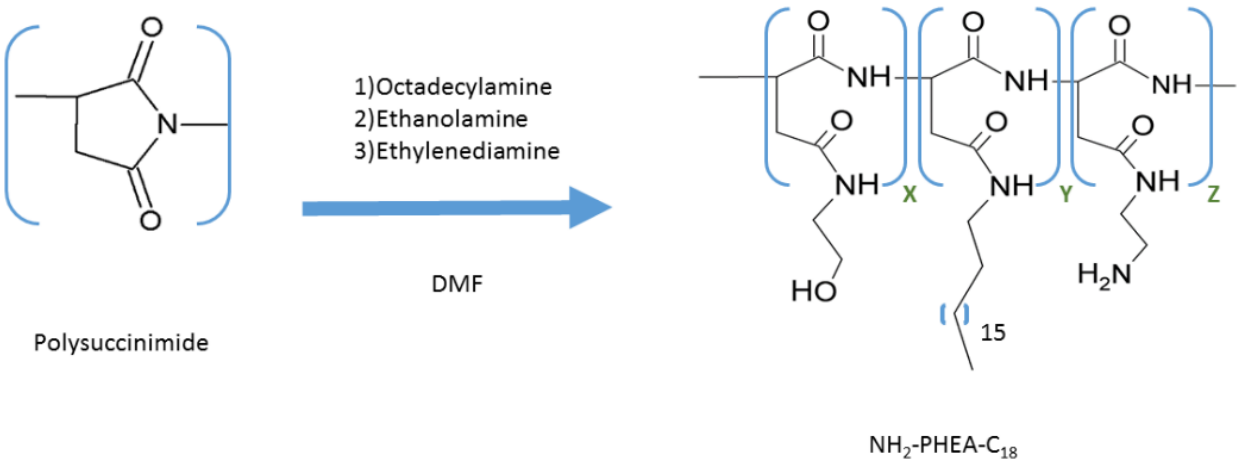

Figure 6.1 Scheme to prepare amphiphilic polyaspartamide (termed NH_2-PHEA-C_{18}). Note that the distribution of x, y, and z in the polymer chain is random.

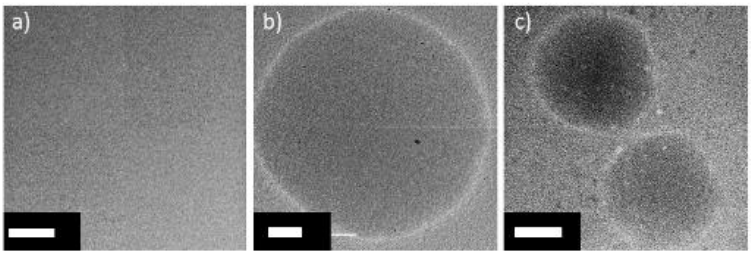

d)

DS_{C18} (%)	Diameter (nm)
0	N/A
2	1006
10	385

Figure 6.2 Transmission electron microscopy (TEM) images of nanocarriers formed from polyaspartamide with varying amounts of octadecyl chains. (a) Image of PHEA-OH (DS_{C18} = 0%) polymer after drop-wise precipitation. (b) Image of vitamin E-loaded NH_2-PHEA-C_{18} (DS_{C18} of 2%) nanocarriers. (c) Image of vitamin E-loaded NH_2-PHEA-C_{18} (DS_{C18} of 10%) nanocarriers. White scale bars correspond to 200 nm. (d) Table depicting average diameter of nanocarrier with respect to DS_{C18}. No discernible nanocarriers are present in (a), so a value of N/A/ is reported in the table. At least 10 images were analyzed per nanocarrier.

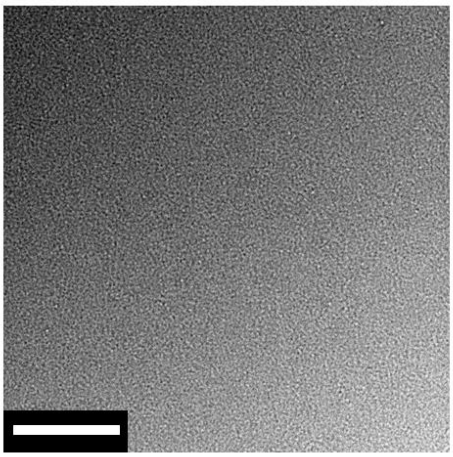

Figure 6.3 Transmission electron microscopy (TEM) image depicting NH_2-PHEA-C_{18} (DS_{C18} of 20%) polymer after drop-wise precipitation. Scale bar corresponds to 200 nm.

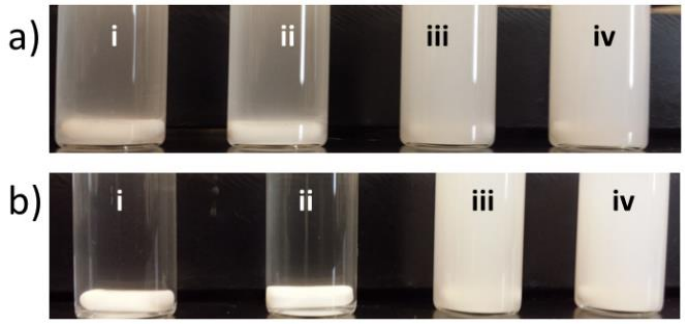

c)

DS_{C18}	ΔG_{sep} (J/mol)	ΔS_{sep} (J/mol-K)	ΔH_{sep} (J/mol)
N/A	-1050	28.1	7250
0	-2240	78.5	20710
2	4440	-10.8	1270
10	3880	10.3	6920

Figure 6.4 Thermodynamic stability of vitamin E dispersions with and without an octadecyl chain-containing polyaspartamide. (a) Image depicting (i) pure vitamin E dispersed in water (N/A); (ii) vitamin E and PHEA-OH (DS_{C18} of 0%) dispersed in water; (iii) vitamin E-loaded NH_2-PHEA-C_{18} (DS_{C18} of 2 %) nanocarrier dispersed in water; (iv) vitamin E-loaded NH_2-PHEA-C_{18} (DS_{C18} of 10 %) nanocarrier dispersed in water. Image was captured immediately after fabrication. (b) Image depicting (i) pure vitamin E dispersed in water (N/A); (ii) vitamin E and PHEA-OH (DS_{C18} of 0%) dispersed in water; (iii) vitamin E-loaded NH_2-PHEA-C_{18} (DS_{C18} of 2 %) nanocarrier dispersed in water; (iv) vitamin E-loaded NH_2-PHEA-C_{18} (DS_{C18} of 10 %) nanocarrier dispersed in water. Image was captured 24 h after fabrication. (c) Table of Gibbs free energy of separation (ΔG_{sep}), enthalpy of separation (ΔH_{sep}), and entropy of separation (ΔS_{sep}) with respect to degree of substitution of octadecyl chain. Note that N/A corresponds to the case where vitamin E was added to water with no PHEA polymer present.

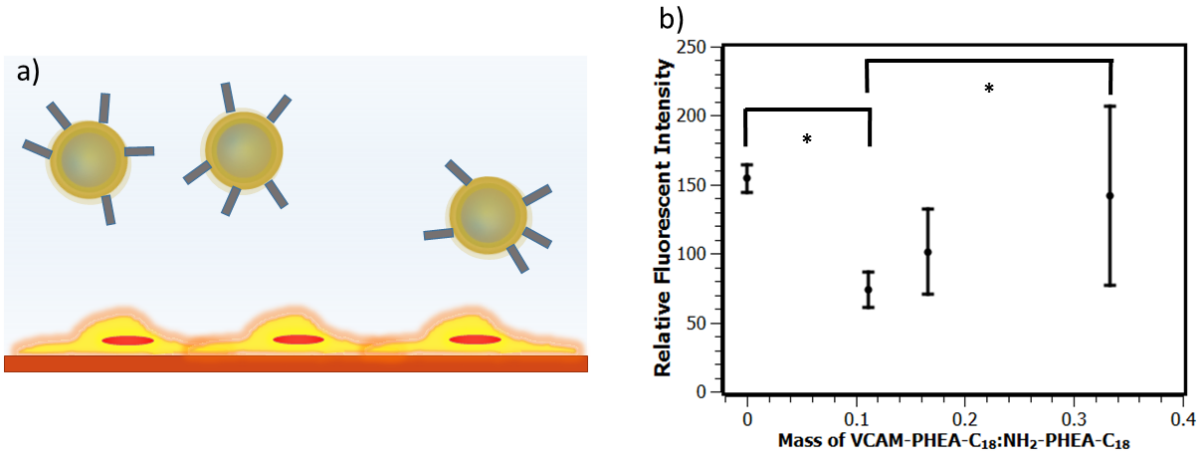

Figure 6.5 Monitoring adhesion of VCAM-binding vitamin E-loaded nanocarriers to an inflamed endothelial cell monolayer. (a) Schematic depicting the adhesion of VCAM-binding nanocarriers to a monolayer. (b) Relative fluorescent intensity of cell monolayer after incubating with nanocarriers with varying amount of VCAM-binding peptides. The mass ratio of PHEA polymer with VCAM-binding peptide to PHEA polymer without VCAM-binding peptide was varying accordingly. DS_{C18} was kept constant for both polymers at 10 %. Values represent the average of at least 3 samples, and bars represent standard deviation. * corresponds to $p<0.05$.

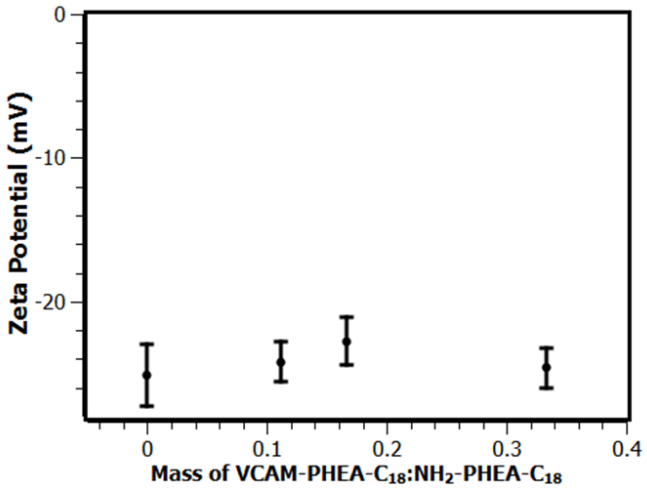

Figure 6.6 Zeta potential measurements of nanocarriers with VCAM-binding peptides.

6.6 References

(1) Anajafi, T.; Mallik, S. Polymersome-Based Drug-Delivery Strategies for Cancer Therapeutics. *Ther. Deliv.* **2015**, *6* (4), 521–534.
(2) Prabhu, R. H.; Patravale, V. B.; Joshi, M. D. Polymeric Nanoparticles for Targeted Treatment in Oncology: Current Insights. *Int. J. Nanomedicine* **2015**, *10*, 1001–1018.
(3) Wilhelm, S.; Tavares, A. J.; Dai, Q.; Ohta, S.; Audet, J.; Dvorak, H. F.; Chan, W. C. W. Analysis of Nanoparticle Delivery to Tumours. *Nat. Rev. Mater.* **2016**, *1* (5), 16014.
(4) Bae, Y. H.; Park, K. Targeted Drug Delivery to Tumors: Myths, Reality and Possibility. *J. Controlled Release* **2011**, *153* (3), 198–205.
(5) Dahan, A.; Miller, J. M. The Solubility–Permeability Interplay and Its Implications in Formulation Design and Development for Poorly Soluble Drugs. *AAPS J.* **2012**, *14* (2), 244–251.
(6) Herrera, E.; Barbas, C. Vitamin E: Action, Metabolism and Perspectives. *J. Physiol. Biochem.* **2001**, *57* (1), 43–56.
(7) Lai, M.-H.; Clay, N. E.; Kim, D. H.; Kong, H. Bacteria-Mimicking Nanoparticle Surface Functionalization with Targeting Motifs. *Nanoscale* **2015**, *7* (15), 6737–6744.
(8) Ruf, H.; Gould, B. J. Size Distributions of Chylomicrons from Human Lymph from Dynamic Light Scattering Measurements. *Eur. Biophys. J. EBJ* **1999**, *28* (1), 1–11.
(9) Seelig, J.; Ganz, P. Nonclassical Hydrophobic Effect in Membrane Binding Equilibria. *Biochemistry (Mosc.)* **1991**, *30* (38), 9354–9359.
(10) Tsourkas, A.; Shinde-Patil, V. R.; Kelly, K. A.; Patel, P.; Wolley, A.; Allport, J. R.; Weissleder, R. In Vivo Imaging of Activated Endothelium Using an Anti-VCAM-1 Magnetooptical Probe. *Bioconjug. Chem.* **2005**, *16* (3), 576–581.
(11) Jeong, J. H.; Schmidt, J. J.; Kohman, R. E.; Zill, A. T.; DeVolder, R. J.; Smith, C. E.; Lai, M.-H.; Shkumatov, A.; Jensen, T. W.; Schook, L. G.; et al. Leukocyte-Mimicking Stem Cell Delivery via in Situ Coating of Cells with a Bioactive Hyperbranched Polyglycerol. *J. Am. Chem. Soc.* **2013**, *135* (24), 8770–8773.

CHAPTER 7: CONCLUSION

7.1 Summary

With the studies included herein, we have demonstrated new techniques to prepare unique soft materials for biomedical applications. For ease of processing, we have utilized several self-assembly approaches throughout.

For our 3D cell cultures studies, we have tuned the properties of self-assembled collagen gels by modulating the hydrogen bond network which stabilizes individual collagen fibers. In turn, we prepared hydrogel systems with controllable stiffness and constant hydraulic conductivity. With this platform, changes in breast cancer malignancy in response to changes in flow or stiffness were examined. Separately, to prepare multifunctional hydrogels, we utilized a 3D printing technique to prepare microgels with dual diagnostic and therapeutic functions. It was determined that keeping the diagnostic and therapeutic functions separate within the same hydrogel prevented any potential interference between the two functions, thus highlighting the importance of spatial separation in preparing multifunctional biomaterials.

This thesis has also examined the preparation of polyaspartamide nanoparticles for different diagnostic or therapeutic functions. In doing so, this thesis has contributed significant knowledge to the processing techniques used to self-assemble polymeric nanoparticles from amphiphilic polymers. By adding a valine chain to an amphiphilic polyaspartamide, polymer solubility in organic solvents was dramatically improved. By mixing the resulting polymer solutions into water at different rates on a microfluidic chip, micelles with different sizes were prepared. Interestingly, as the hydrophobic content of polyaspartamide increased, bilayered polymersomes could be formed with turbulent mixing, but not with on-chip mixing.

Separately, clusters of polyaspartamide-coated superparamagnetic iron oxide nanoparticles were prepared, and then incubated with stem cells. Here, I sought to increase the amount of SPION clusters in each cell, thus increasing the MRI signal from the cells. It was determined that stem cell labeling under slight mechanical stress led to a greater degree of SPION incorporation into the cells, in turn leading to a higher MRI signal per cell.

By using the same polyaspartamide chemistry, vitamin E-loaded nanocarriers were prepared. By tuning the hydrophobic content of polyaspartamide, the size of the nanocarriers was tuned to match that of chylomicrons, highly-efficient in vivo transporters of vitamin E.

7.2 Future Work

The current work on 3D cell culture mostly focused on modulating hydrogen bonding to change hydrogel properties. However, additional noncovalent interactions are present in many natural or synthetic hydrogels, such as electrostatic interactions. More complex hydrogel systems could be envisioned by tuning these noncovalent interactions in addition to tuning hydrogen bonding. For future work in the 3D printing of multifunctional microgels, additional functions (for example, tissue adhesion) could be added during the printing process.

Future nanoparticle work will mostly focus on transitioning to *in vivo* mouse models. Experiments with vitamin E-loaded nanocarriers in mice are currently underway at the Mayo Clinic. These nanoparticles will be used to treat venous neointimal hyperplasia (VNH), a chronic condition characterized by scar tissue formation in the patient's veins. Recent evidence suggests that this disease may be mediated by the presence of oxidative stress. Therefore, using a vitamin E-loaded nanocarrier could control the amount of oxidative stress in vivo, and reduce the severity of this disease. Moreover, it may be possible to combine these vitamin E-loaded

nanocarriers with SPIONs, in order to provide a dual therapeutic/diagnostic approach to treating VNH.

Overall, the soft material formulations developed in the six studies within this thesis will be broadly relevant to a variety of in vivo treatments for different malignant and chronic diseases.